

University of St Andrews



Full metadata for this thesis is available in
St Andrews Research Repository
at:

<http://research-repository.st-andrews.ac.uk/>

This thesis is protected by original copyright

Adsorption and growth of organic molecular films on silicon surfaces

Tomás J. Rada Crespo



Thesis submitted in accordance with the requirements
of the University of St. Andrews for the degree of
Doctor of Philosophy.

Supervised by: **Prof. Neville. V. Richardson.**
School of Chemistry, University of St. Andrews
October 2002



TL E 252 .

Abstract.

The adsorption of organic molecules, including maleic anhydride, perylene, 3,4,9,10- perylene tetracarboxylic dianhydride (PTCDA) and tetracene on silicon surfaces in ultra-high vacuum have been investigated by several surface sensitive techniques such as low energy electron diffraction, high resolution energy electron loss spectroscopy, photoluminescence and scanning tunnelling microscopy.

A preliminary investigation to assess the applicability of photoluminescence studies considered the initial oxidation processes of silicon, through adsorption of molecular oxygen and water to follow the formation of gap states. Exposure of Si(100) to O₂ at room temperature leads to formation of gap states, but the density of these decreases slightly after water exposure. Photoluminescence measurements of adsorption of maleic anhydride on Si(100) result in a gap state density slightly lower than that determined for clean Si(100). The adsorption site for the chemisorption of maleic anhydride on Si(100)-2x1 at room temperature has been identified at low coverage. Maleic anhydride adsorbs almost exclusively on inter-dimer sites in the submonolayer regime. This adsorption site induces a local rearrangement of unsaturated silicon dimers.

Different growth modes have been observed for large organic molecules such as perylene, PTCDA and tetracene. Formation of small clusters has been obtained, through molecular beam deposition, for multilayer of perylene and tetracene on Si(100) and hydrogen terminated Si(111) surfaces. In contrast, PTCDA molecules form an incommensurate crystalline structure on hydrogen passivated Si(111). High resolution images allow the identification of the crystal orientation and the molecular mechanism

for the formation of the dendritic shapes, which are observed. In the submonolayer regime, it has been observed that tetracene molecules adsorb in a flat-lying configuration on Si(100), while perylene adopts an up-right orientation.

Acknowledgements

My greatest debt of gratitude is to my supervisor Prof. Neville V. Richardson for his patience, attitude and for leading me through surface science and beyond. I specially thank Dr. Thomas Bitzer and his wife for their invaluable friendship, support and encouragement as well as Dr. Q. Chen for his permanent support and friendly discussions.

I truly appreciate the camaraderie and incredible environment within our group at St. Andrews, and everybody - Steve, Chris, Alberto, Danny, Sandy, Wendy, Per, Euan, Tim, Emma and Manfred - deserves my sincere acknowledgement.

I also thank anyone in Chemistry and Physics who have contributed in any way to this thesis.

I would like to thank Dr. Thomas Dittrich for his friendship and support.

Many people in St. Andrews, who have made my non-academic life really enjoyable during these three years of my doctorate, deserve my gratitude and to all of them: THANK YOU!

Thank Universidad del Norte and in particular Joachim Hahn, Beatriz de Torres and Agustin Barrios for their support, encouragement and for listening to my “screams”.

I dedicate this thesis to two strong Elviras, my mum and my lovely wife, to my wonderful son, Martin, and in memory of my dad. Mi eterno agradecimiento a mi esposa e hijo por su amor y apoyo, además por que fueron el faro que iluminó mi camino estos tres años y espero que perdonen mi ausencia durante este tiempo. A mi familia en general un agradecimiento inmenso por el apoyo constante y el valor que me brindaron. Mencion especial merecen mis abuelos y hermanos.

TABLE OF CONTENTS

Chapter 1.

Silicon Surfaces

1.1. Introduction	1
1.2. Physics and electronic properties	1
<i>1.2.1. Silicon surfaces</i>	<i>1</i>
<i>1.2.2. Surface states on silicon</i>	<i>3</i>
<i>1.2.3. Silicon (111)</i>	<i>6</i>
<i>1.2.3.1. Silicon(111)-7x7</i>	<i>6</i>
<i>1.2.4. Silicon (100)</i>	<i>7</i>
1.3. The chemistry of Si(100)	11
1.4. Band gap	13
1.5. Photoluminescence of silicon	15
1.6. Silicon devices	20
<i>1.6.1. A historical review</i>	<i>20</i>
<i>1.6.2. The future</i>	<i>22</i>
1.7. Organic semiconductors	23
<i>1.7.1. Historical introduction</i>	<i>23</i>
<i>1.7.2. Maleic anhydride</i>	<i>25</i>
<i>1.7.3. Perylene</i>	<i>25</i>
<i>1.7.4. Perylene -3,4,9,10- Tetra-Carboxylic-DiAnhydride</i>	<i>26</i>
<i>1.7.5. Tetracene</i>	<i>26</i>
References	27

Chapter 2

Experimental Techniques

2.1. Introduction	31
2.2. Scanning tunnelling microscopy	32
2.3. Scattering from surfaces	36
2.4. Low energy electron diffraction	37
2.5. High resolution electron energy loss spectroscopy	40
2.6. Photoluminescence: principle	44
2.7. <i>Ab initio</i> calculation	46
2.8. Cleaning silicon procedure	47
2.9. Hydrogen terminated surfaces	47
2.10 The doser	49
2.11 Experimental details	50
References	51

Chapter 3

Gap State Formation During the Initial Oxidation of Si(100)-2x1 and Si(111)

3.1. Introduction	54
3.2. Review of oxygen on silicon surfaces	56
3.3. Review of water adsorption and oxidation on silicon surface	57
3.4. HREELS study of oxygen adsorption on Si(100)-2x1	59

3.5. HREELS study of water on Si(100)-2x1	62
3.6. Gap state formation during initial oxidation of Si(100)-2x1	64
3.7. Photoluminescence study of water on Si(100)-2x1	67
3.8. Gap state changes on Si(111) surface	72
3.9. Conclusions	74
References	74

Chapter 4

Physical and Chemical Properties of Maleic Anhydride on Si(100)-2x1 Surface

4.1. Introduction	77
4.2. Chemisorption of maleic anhydride on Si(100)-2x1	78
4.3. HREELS study	82
4.3.1. <i>Adsorption of MA on Si(100)</i>	82
4.3.2. <i>Thermal decomposition of maleic anhydride</i>	84
4.4. STM study of maleic anhydride on Si(100)-2x1	85
4.5. Influence of tunnelling conditions on maleic anhydride STM images	90
4.5.1. <i>Constant current.</i>	90
4.5.2. <i>Constant voltage</i>	93
4.6. Simulations of scanning tunnelling images	93
4.7. PL experiments	104
4.7.1. <i>Formation of electronic states in the fundamental gap at MA/Si(100)-2x1</i>	104
4.7.2. <i>Desorption of MA and changes in the electronic state</i>	106

4.8. Conclusions	108
References	108

Chapter 5

Adsorption of Perylene on Silicon Surfaces

5.1. Introduction	111
5.2. Review of previous work on perylene	112
5.2.1. <i>Perylene: half century ago</i>	112
5.2.2. <i>Epitaxial growth</i>	113
5.2.3. <i>Vibrational studies</i>	118
5.3. HREELS results	119
5.3.1. <i>Perylene on clean Si(100)-2x1</i>	119
5.3.2. <i>Perylene on H:Si(111)</i>	120
5.4. STM	124
5.4.1. <i>Clean Si(100)-2x1</i>	124
5.4.2. <i>Hydrogen – terminated Si(111)</i>	127
5.5. Calculations	129
5.6. Discussion	130
5.7. Conclusions	133
References	134

Chapter 6

Diffusion limited growth of PTCDA crystals on H:Si(111) surface

6.1. Introduction	136
--------------------------	------------

6.2. Relevant work on PTCDA: a brief review	139
6.3. Vibrational study	142
6.4. STM study	144
6.5. <i>Ab initio</i> results	155
6.6. Conclusions	157
References	157

Chapter 7

Study of tetracene adsorption on silicon surfaces

7.1. Introduction	161
7.2. Review of benzene on silicon surfaces	163
7.3. Vibrational study of tetracene	166
7.4. Desorption of tetracene from H:Si(111) at room temperature	169
7.5. HREELS study of tetracene adsorption on clean Si(100)-2x1	170
7.6. STM analysis of tetracene on Si(100)-2x1	172
7.6.1. <i>Filled state images</i>	<i>172</i>
7.6.2. <i>Empty state images</i>	<i>174</i>
7.7. <i>Ab initio</i> calculations	177
7.8. Discussion	179
7.9. Conclusions	183
References	184

LIST OF PUBLICATIONS

This thesis is based on the following publications

- T. Rada, Q. Chen, N. V. Richardson, *Scanning tunnelling microscopy of tetracene on Si(100)-2x1*, Phys. Rev. B (submitted).
- Q. Chen, T. Rada, Th. Bitzer, N. V. Richardson, *Diffusion limited growth of PTCDA crystals on H:Si(111) surfaces*, Chem. Mater. (submitted).
- Q. Chen, T. Rada, A. McDowall, N. V. Richardson, *Epitaxial growth of a crystalline organic semiconductor: Perylene/Cu{110}*, Chem. Mater. **14**, 743 (2002).
- W. A. Hofer, A. J. Fisher, Th. Bitzer, T. Rada, N.V. Richardson, *Tuning in on single molecular states: adsorption sites and STM images of maleic anhydride on Si(100)*, Chem. Phys. Lett. **355**, 347 (2002).
- Th. Dittrich, Th. Bitzer, T. Rada, N.V. Richardson, V. Yu. Timoshenko, J. Rappich, F. Koch, *Defect transformation under growth of submonolayer oxides on silicon surfaces at low temperatures*, Microelectron. Eng. **59**, 399 (2001).
- T. Bitzer, T. Rada, N.V. Richardson, *Inhibition of the [2+2] cycloaddition: Maleic anhydride on Si(100)-2x1*, J. Phys. Chem. B **105**, 4535 (2001).

- T. Bitzer, T. Rada, N.V. Richardson, T. Dittrich, F. Koch, *Gap states at the interface of ultra – thin oxide and organic films on Si(100)*, Solid State Phenomena **76-77**, 131 (2001).

- T. Bitzer, T. Rada, N.V. Richardson, T. Dittrich, F. Koch, *Gap state formation during the initial oxidation of Si(100)-2x1*, App. Phys. Lett. **77**, 3779 (2000).

- T. Bitzer, T. Dittrich , T. Rada, N.V. Richardson, *The electronic properties at the Maleic anhydride /Si(100)-2x1 interface*, Chem. Phys. Lett. **331**, 433 (2000).

List of Acronyms and abbreviations

AFM	Atomic Force Microscopy
BZ	Brillouin Zone
D_{it}	Interface states density
DOS	Density of States
E_g	Band gap energy
ETL	Electron transport layer
FET	Field Effect Transistors
HOMO	Highest Occupied Molecular Orbital
HREELS	High Resolution Energy Electron Loss Spectroscopy
HTL	Hole transport layer
IR	Infrared
LEED	Low Energy Electron Diffraction
LUMO	Lowest Unoccupied Molecular Orbital
MA	Maleic anhydride
ML	Monolayer
MO	Molecular orbital
MOS	Metal Oxide Semiconductor
OFET	Organic Field Effect Transistors
OLED	Organic Light Emitting Device
OMBD	Organic Molecular Beam Deposition
OMBE	Organic Molecular Beam Epitaxy
PL	Photoluminescence
PTCDA	3,4,9,10-perylene tetracarboxylic dianhydride
SC	Solar Cells

STM	Scanning Tunnelling Microscopy
STS	Scanning Tunnelling Spectroscopy
UHV	Ultra High Vacuum
UV	Ultra-violet
vdW	Van der Waals

CHAPTER 1

Silicon Surfaces

1.1 Introduction

Silicon is one of the most important and representative semiconductors and it has been studied extensively since the second half of the past century. The understanding and control of silicon surfaces is of great importance in the production of silicon based electronic devices [1]. In addition to the control of the surface chemistry of etching, doping and film deposition, it is important to achieve well defined structures for devices fabricated on silicon single crystal substrates. In this spatial regime, atomic level properties often dictate how this will be done, leading to miniature surface structures with quantum properties dependent on size. As continued reduction in the size of semiconductor devices takes place, surface phenomena will assume an even greater role in achieving this goal [2].

1.2 Physics and electronic properties

1.2.1 Silicon Surfaces

Silicon crystals have the diamond lattice structure, which belong to the tetrahedral phase, i.e. the atoms are sp^3 hybridised and bonded to four nearest neighbours in tetrahedral co-ordination, as it can be seen from its unit cell in Fig. 1.1. The covalent bond length is 2.35\AA with a bond energy of 226 kJ/mol. The unit cell of this structure can be defined by the set

$$R = ma + nb + pc$$

where \mathbf{a} , \mathbf{b} , and \mathbf{c} are three primitive basis vectors, which describe a crystalline solid with two fcc lattices mutually displaced by $(1/4, 1/4, 1/4)$ of a unit cell, and m, n, p are integers.

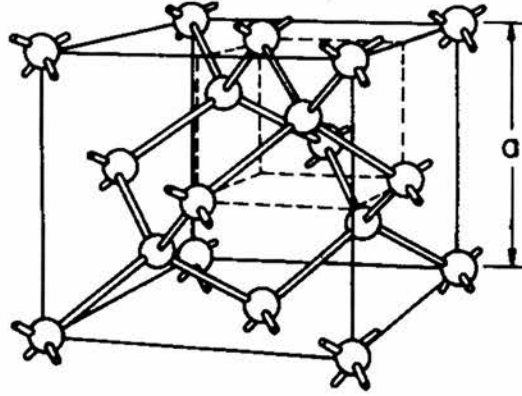


Fig. 1.1 Diamond structure of silicon including its unit cell (direct lattice). The lattice constant is $a=5.43 \text{ \AA}$.

On the other hand, for a given set of the direct basis vectors, a set of reciprocal lattice basis vectors \mathbf{a}^* , \mathbf{b}^* , \mathbf{c}^* , can be defined such that

$$\mathbf{a}^* \equiv 2\pi \frac{\mathbf{b} \times \mathbf{c}}{\mathbf{a} \cdot (\mathbf{b} \times \mathbf{c})}, \quad \mathbf{b}^* \equiv 2\pi \frac{\mathbf{c} \times \mathbf{a}}{\mathbf{a} \cdot (\mathbf{b} \times \mathbf{c})}, \quad \mathbf{c}^* \equiv 2\pi \frac{\mathbf{a} \times \mathbf{b}}{\mathbf{a} \cdot (\mathbf{b} \times \mathbf{c})}$$

so that $\mathbf{a} \cdot \mathbf{a}^* = 2\pi$; $\mathbf{a} \cdot \mathbf{b}^* = 0$, and so on; and the general reciprocal lattice vector is given by

$$\mathbf{G} = h\mathbf{a}^* + k\mathbf{b}^* + l\mathbf{c}^*,$$

where h, k , and l are integers.

The unit cell of a reciprocal lattice can be represented by a Wigner–Seitz cell. Fig. 1.2a shows a typical example for face-centred cubic structure [3]. Fig. 1.2b shows the shape of the constant-energy surface [4], where six ellipsoids along the $\langle 100 \rangle$ axes appear,

with the centers of ellipsoids locate three-fourths of the distance from the Brillouin zone center.

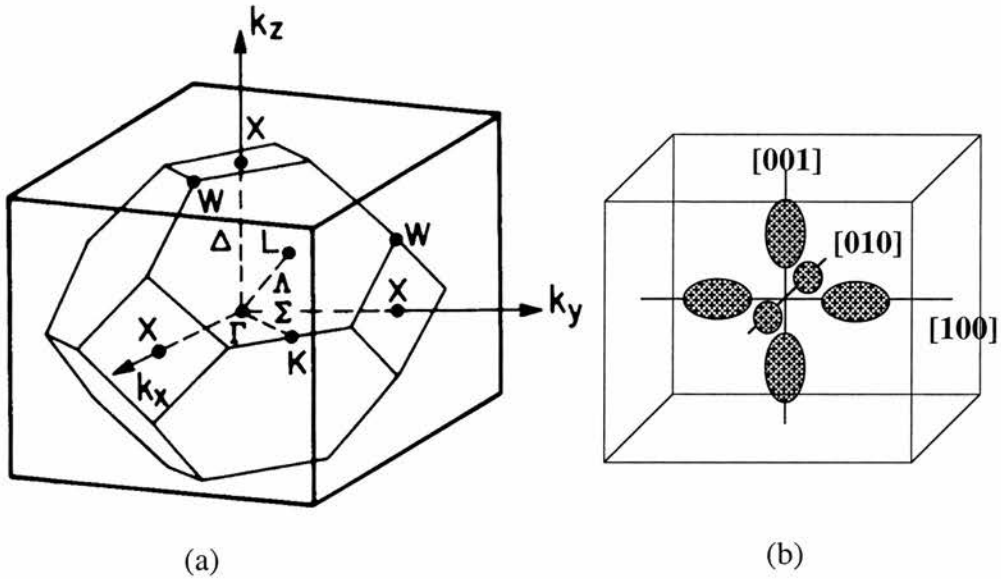


Fig. 1.2 (a) Brillouin zone for the diamond lattice. The most important symmetry points and symmetry lines are also indicated: $\Gamma: 2\pi/a(0,0,0)$, zone centre; $L: 2\pi/a(1/2, 1/2, 1/2)$, zone edge along $\langle 111 \rangle$ axes (Δ); $X: 2\pi/a(0,0,1)$, zone edge along $\langle 100 \rangle$ axes (Δ); $K: 2\pi/a(3/4, 3/4, 3/4)$, zone edge along $\langle 110 \rangle$ axes (Σ) [3].
 (b) Shape of constant energy surface in silicon, including six ellipsoids along $\langle 100 \rangle$ axes [4].

1.2.2 Surface states on silicon

Electronic surface states or interface states were studied at an early stage, due to an important breakthrough on the experimental front in applications of photoconductivity and surface photovoltage spectroscopy [5]. As mentioned above, silicon has a tetrahedral atomic bonding characteristic, which is a decisive factor for the crystal structure. When a

crystal is cut or cleaved, bonds are broken, and dangling bonds are created at the surface. The number and direction of these dangling bonds will depend on the macroscopic direction of the surface normal. See Fig. 1.3

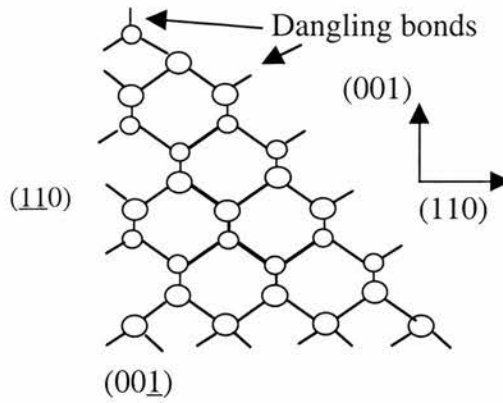


Fig. 1.3 The dangling bond formation on the unreconstructed surfaces of the three low index planes of silicon [6].

Also the sp^3 hybridization leads to the formation of strongly directional bonding lobes which appear as dangling bonds orbitals at the surface. The different dangling bond structures for the three surfaces (assumed to be non-reconstructed, truncated bulk) are shown in Fig. 1.4 a,b. The corresponding 2D Brillouin zones (BZ) of the non-reconstructed surfaces are depicted in Fig. 1.4c. Formation of the “truncated” (111) surface creates one half-filled dangling bond orbital per surface atom perpendicular to the surface. The unreconstructed (100) surface unit cell contains one atom with two broken bonds tilted with respect one another.

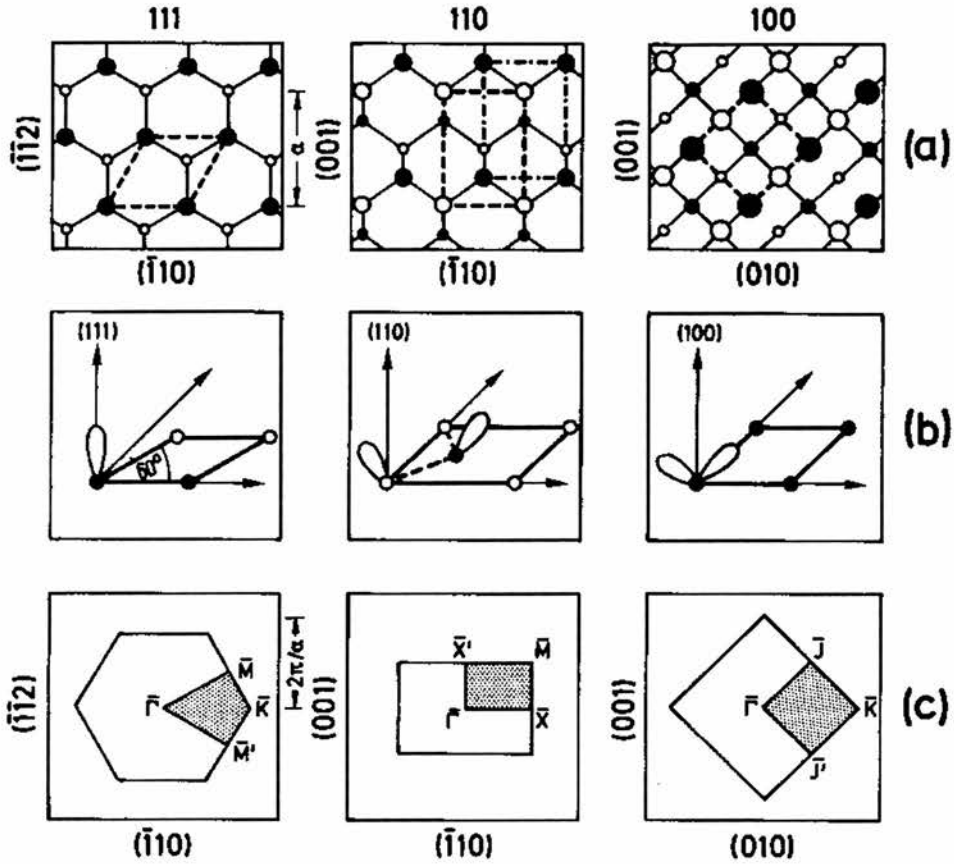


Fig. 1.4 Crystallography of the non-reconstructed three low index surfaces of the zincblende lattice (sp^3 - bonded). The diamond lattice of Si would be obtained if all atoms were the same species. a) Top view and broken lines indicate possible unit meshes. b) Schematic plot of the dangling bond orbitals occurring on the different surfaces. a) Corresponding ideal surface Brillouin zone with conventional labelling [5].

However, the surface energy can be lowered by reducing the number of dangling bonds by rebonding, which leads to a wide variety of surface reconstructions on silicon surfaces. Remaining dangling bonds at the surface are the source of chemical activity of silicon surfaces. The reconstructed cases are discussed in the following section.

1.2.3 Silicon (111)

In the [111] direction, the silicon crystal has a double-layer structure, with each Si atom having three bonds to atoms within the same double layer and one bond to an atom in the adjacent double layer (Fig. 1.3). Si(111) is the natural cleavage surface since only one bond per Si atoms links adjacent double layers to each other.

Corresponding to the one dangling bond (broken sp^3 bond) on the Si(111) surface a single band of surface states within the forbidden gap is expected. This band is split off from the bulk sp^3 states forming the valence and conduction bands. Because of the fewer neighbours at the surface, i.e. reduced orbital overlap the surface states are lowered in energy relative to the bulk valence band states and thus fall into the gap. Due to bond breaking the band is half filled since each side of the broken bond can accept one of the two electrons of the unbroken covalent bond. However, the reality is much more complex because of reconstructions.

1.2.3.1 Silicon(111)-7x7

If the (111) crystal is cleaved at room temperature, a 2x1 reconstruction is found in LEED. If cleaved at very low temperature (~ 20 K) a 1x1 LEED pattern appears. After annealing to temperatures higher than about 400° C a 7x7 structure occurs indicating an extremely long range periodicity. The 7x7 structure is definitely the most stable configuration; the 1x1 and 2x1 structures are frozen-in metastable configurations.

A structure model for Si(111)-7x7 surface has been proposed by Takahashi et al. [7], referred to as the DAS (Dimer- Adatom Stacking-fault) model contains 12 Si adatoms, 6 rest atoms, 9 dimers and one corner hole per surface unit cell. The 2D surface BZ for the 7x7 structure has 1/7 of the 1x1 zone diameter, i.e. because symmetry, the one dangling-

bond band of the 1×1 non-reconstructed surface can be folded back seven times into the 7×7 BZ.

1.2.4 Silicon (100)

The Si(100) is by far the most important surface for semiconductor devices. The $\{100\}$ planes have a square unit cell, and each silicon atom below the surface is bonded to two atoms in the plane below and two atoms in the plane above. The structure of the bulk-terminated surface is shown in Fig. 1.5 a.

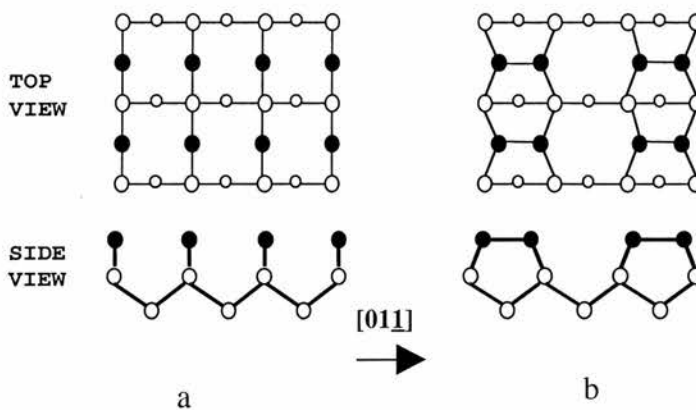


Fig. 1.5 Scheme of the unreconstructed (a) and reconstructed (b) Si(100) surface. Filled circles represent the surface atoms which have two dangling bond each, open circles represent bulk atoms, and size of open circles in the top decrease with the distance from the surface [6].

The commonly accepted model for the reconstructed Si (100) surface is the dimer model. In this model the density of the dangling bonds is decreased by 50% by creation of rows of symmetric dimers, where each surface silicon atom bonds to a neighbouring atom along the $[01\bar{1}]$ direction using one of its dangling bonds, as shown in Fig. 1.5b. In other words, sp^3 like dangling bonds on neighbouring Si surface atoms could dehybridize into

orbitals whose nature is more sp_z , p_x , p_y , and finally form Si dimers at the surface, (Fig. 1.6), which can be asymmetric or symmetric dimers [8].

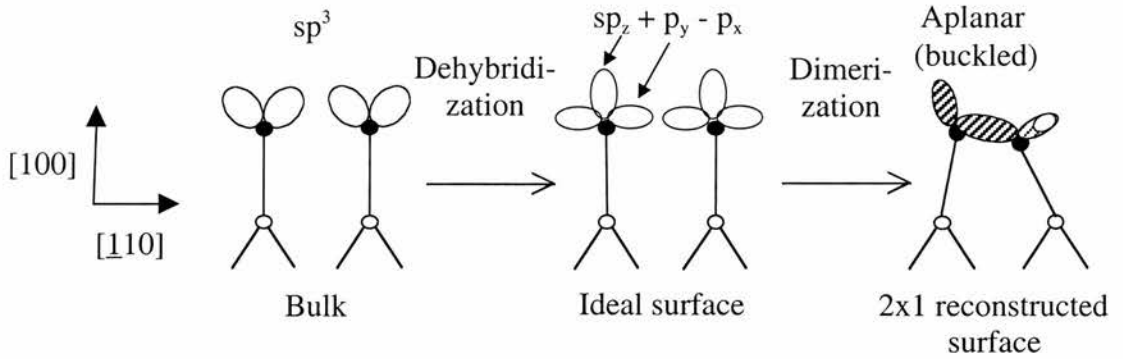


Fig. 1.6 Schematic diagram of the dehybridization and dimerization leading to the non-planar dimer structure [8].

Until now, the question of whether the dimers are symmetric or asymmetric (buckled) on perfect regions, and although final agreement has not been reached yet, the majority of results point toward buckled dimers. (2x1) Structures are expected for symmetric dimers (Fig 5b). However, many reconstruction patterns have been observed, for example $p(2 \times 2)$, $c(4 \times 2)$ [9,10,11], and $c(4 \times 4)$ [12].

Detailed electronic structures and geometries of Si(100) reconstructed surfaces have been investigated [13,14]. Those studies have shown that the asymmetric model gives better agreement between measured and calculated surface state densities. Zhu et al [12], using a self-consistent calculation with a norm-conserving non-local pseudopotential have investigated some reconstructed surfaces. They found that $c(4 \times 2)$ system is the most favourable one at absolute zero temperature; moreover, the $p(2 \times 2)$ system can also be favoured because the total energy difference between $c(4 \times 2)$ and $p(2 \times 2)$ systems is

relatively small. The calculated charge-density for both symmetric and asymmetric dimer (2×1) models are plotted in Fig. 1.7.

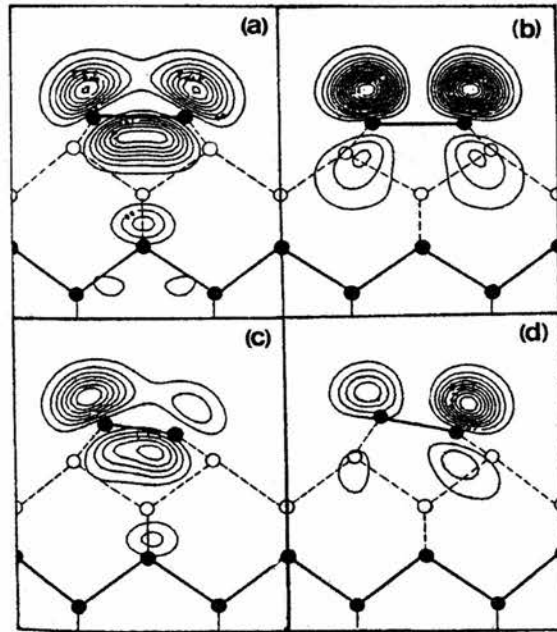


Fig. 1.7 Density of charge for the dimers on $\text{Si}(100)\text{-}2 \times 1$ is presented. (a) Surface bonding and (b) antibonding states for symmetric dimer model. (c) Surface bonding and (d) antibonding states for the asymmetric dimer model. The plots are in the (110) plane cutting the surface at right angle. The solid circles represent the Si atoms lying on the plane, and the solid lines between them represent the hypothetical covalent bonds. Si atoms not on the plane are denoted by open circles [12].

The asymmetric dimer showed qualitatively in Fig. 1.6, which is related with a certain degree of ionicity because of its asymmetry (with the upper silicon atom considered as -ve and the lower as +ve), leads to even lower total energy in the calculation. The dangling-bond band dispersion has been calculated both for symmetric and the asymmetric dimers (Fig. 1.8). For the asymmetric dimer a total gap between the occupied and the

surface state appears, the surface is thus conducting and acting as metallic surface – in contrast to the symmetric dimer surface.

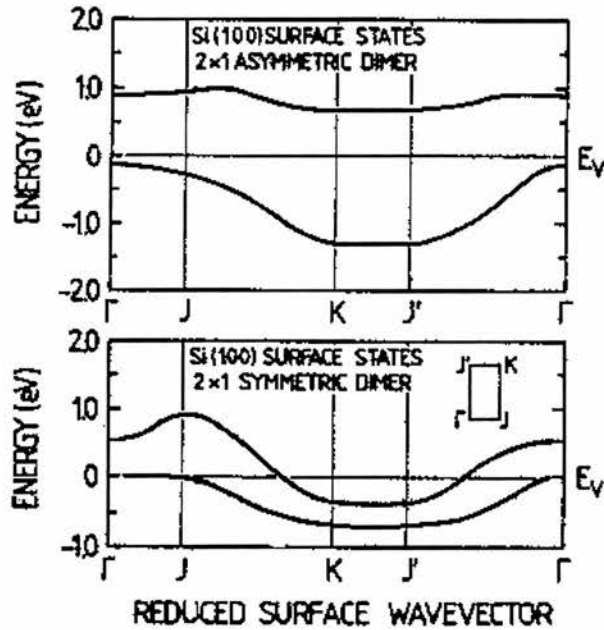


Fig. 1.8 Calculated dispersion curves for the 2×1 asymmetric and the 2×1 symmetric dimer models, respectively [15].

A typical STM image from the Si(100)- 2×1 surface is presented in Fig. 1.9 and the presence of parallel rows of symmetric dimers is observed and defects resulting from missing dimers. Furthermore, buckled dimers (or pinning of asymmetric dimers) are seen as zigzag patterns at surface defects such as step edges. Without pinning, thermal activation leads to virtually symmetric appearance.

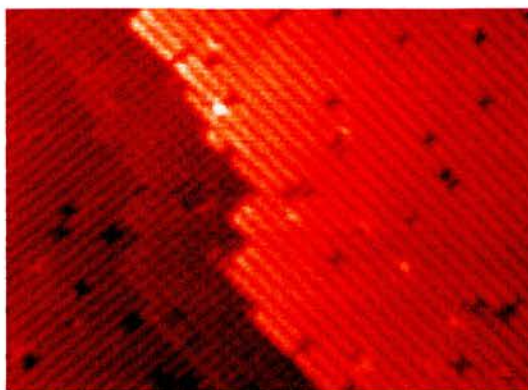


Fig. 1.9 STM images ($310 \text{ \AA} \times 240 \text{ \AA}$) of two filled state layers of Si(100) at sample bias voltage -2.36 V .

Another important feature is the direction of the dangling bonds on the (100) surface which rotate 90° upon crossing a step of single-layer height due to the tetrahedral bonding structure of the silicon lattice. Consequently, the dimer rows on consecutive terraces separated by single-layer height step are perpendicular to each other.

1.3 The chemistry of Si(100)

The chemistry of Si (100) surface is intimately connected with the geometry and electronic structure of the surface atoms. So, for each pair of Si atoms in the top layer, there are a total of four broken bonds. The rehybridization of these orbitals and concurrent motion of the Si atoms towards one another results in a Si dimer in which there is a strong σ bond linking the two atoms and a second weaker π bond [16]. Thus, the silicon surface dimers can be considered to have a double bond. Since STM images the surface electronic (not topographic) structure, it is possible to directly image the spatial distribution of the electronic states, particularly those that lie nearest the Fermi level [17]. The π molecular orbital has its maximum nearest the centre of the Si=Si dimer bond, while the π^* antibonding orbital has a node in the wave function at this location. As a result, unoccupied

down-atom becomes sp^2 -like and has proportionately less local occupied-state density. The degree of π -bonding varies as the dimer fluctuates, being optimal, transiently, when the dimer is symmetric. When the dimer is buckled the dangling bonds are no longer degenerate and π -bonding is further disfavoured. The buckled dimer has associated with it an occupied-unoccupied pair of states. At the surface, these form the valence- and conduction-band edges.

STM studies at room temperature have observed primarily non-tilted dimers, while tilted dimers are typically visible near step edges or defects where the intrinsic symmetry is broken. When tilted dimers are observed, they always alternate from dimer to dimer along a row giving rise to “zigzag” structures in the STM images. The tilting of a dimer has an associated charge transfer, in which electrons are transferred from the down atom to the up atom [15,17].

1.4 Band gap

As is well known, the separation between the energy of the lowest conduction band and that of the highest valence band is called the band gap E_g . This zone, for an intrinsic semiconductor, is a forbidden energy region in which allowed states cannot exist. Also it is the most important parameter in semiconductor physics. In contrast, virtually all commercial semiconductors are extrinsic; that is, the electrical behaviour is determined by impurities, which, when present in even minute concentrations, introduce excess electrons or holes. Thus, an impurity concentration of one atom in 10^{12} is sufficient to render silicon extrinsic at room temperature. In the case of excess electrons, the extra non-bonding electrons are loosely bound to the region around the impurity atoms by a weak electrostatic attraction. The binding energy for an electron is relatively small (on the order of 0.001 eV)

[19]; thus, it is easily removed from the impurity atom, in which case it becomes a free or conducting electron.

The energy state of such an electron may be viewed from the perspective of the electron band model scheme. For each of the loosely bound electrons, there exists a single energy level, or energy state, which is located within the forbidden band gap just below the conduction band, see Fig. 1.11a. The electron binding energy corresponds to the energy required to excite the electron from one of these impurity states to a state within conduction band. Each excitation event (Fig. 1.11b) donates a single electron to the conduction band; an impurity of this type is termed a donor.

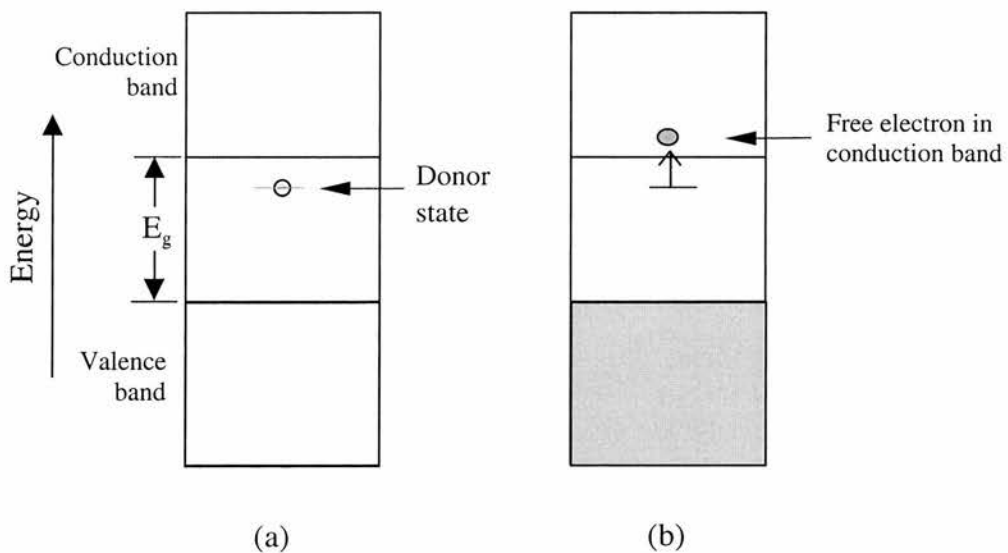


Fig. 1.11 (a) Electron energy band scheme for a donor impurity level located within the band gap. (b) Excitation from a donor state in which a free electron is generated in the conduction band.

Non-local pseudopotential calculations have been used, by Chelikowsky et al [20], to study theoretically the energy bands of some semiconductors, including silicon. The

energy band structure, that is, the energy-momentum (E - k) relationship, of crystalline silicon is shown in Fig 1.12. Also is shown the optical transition between the lowest conduction band and the highest valence band, which corresponds to an indirect transition. The band gap, E_g , for silicon at 300 K is 1.12 eV.

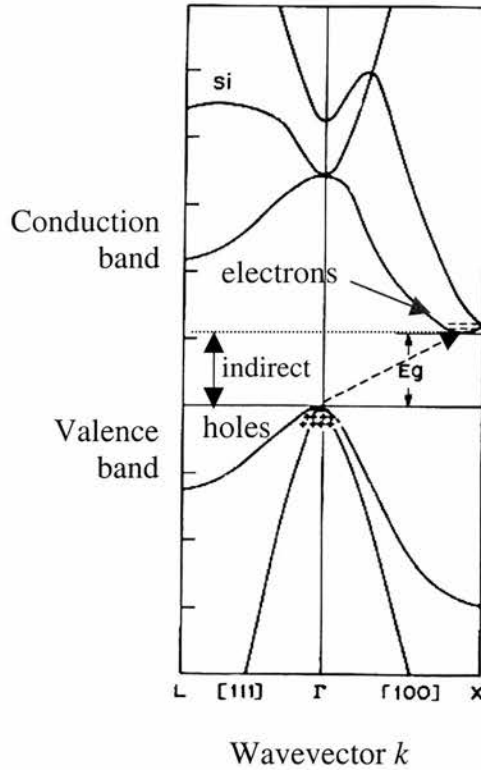


Fig. 1.12 The energy-band structure for silicon, where E_g is the bandgap energy. There are also represented the holes (+) in the valence band and electrons (-) in the conduction band [20].

1.5 Photoluminescence of Silicon.

Crystalline silicon (c-Si) is an indirect semiconductor and the efficiency of the interband luminescence is usually low a room temperature due to high efficiency of non-radiative recombination process [21]. However, photoluminescence (PL) of c-Si at room

temperature can be used as a powerful tool for investigation of non-radiative surface and bulk defects, which is also important for the fast control of the quality of both bulk and surface of c-Si [22]. The principle of PL is given below, in section 2.6. Here, PL is focused on the direct relevance to silicon surfaces. In this way, the efficiency of radiative interband recombination in c-Si is proportional to the product of electron and hole concentrations. Therefore, the PL of c-Si is non-linearly related to the optical excitation and a strong increase of the PL intensity can be reached under an appropriate high optical excitation. Also it was found that the efficient PL of c-Si at room temperature can be excited by sub-nanosecond pulses of a nitrogen laser [23]. Short pulses ($\delta_i < 10$ ns range) of ultraviolet light, which is strongly adsorbed in silicon (adsorption length $\lambda < 20$ nm), are used to generate excess electrons and holes ($\delta_n = \delta_p$) [24]. Dittrich et al. [25] found that the total yield of PL is very sensitive to the surface treatment of the c-Si wafer.

The excess carrier concentrations decrease due to non-radiative bulk and surface recombination, besides ambipolar diffusion and Auger recombination. The excess carrier recombination is mainly non-radiative processes and therefore the radiative band-band recombination is very small due to the indirect band gap in crystalline silicon. However, changes of the non-radiative surface recombination can be investigated by monitoring the radiative band-band recombination, i.e. the PL.

Timoshenko et al. [22] calculated the PL response of c-Si excited by intensive and short laser pulses, which are absorbed within a very thin surface layer. All processes as carrier diffusion and Auger recombinations, non-radiative Shockley–Read recombination, and bimolecular radiative recombination were taken into account. It was shown that PL quantum efficiency can reach some percent of c-Si with very low concentrations of bulk and surface defects. The one-dimensional model proposed considers the evolution of the

non-equilibrium carrier density n excited by a laser pulse in the silicon wafer with thickness d . Therefore the kinetic equation for n can be written in the form [26]

$$\frac{\partial n}{\partial t} = D \frac{\partial^2 n}{\partial x^2} + G(x,t) - \frac{n}{\tau_0} - \beta n^2 - \gamma n^3, \quad \text{Eq. (1)}$$

where D is the ambipolar diffusion coefficient, $G(x,t)$ is generation rate of non-equilibrium carriers, τ_0 is the carrier lifetime in the bulk, β is the coefficient of interband radiative recombination, and γ is the Auger recombination coefficient.

The boundary conditions are [26]

$$\begin{aligned} \left. \frac{\partial n}{\partial x} \right|_{x=0} &= \frac{S_f}{D} [n(0,t) - n_0]; \\ \left. \frac{\partial n}{\partial x} \right|_{x=d} &= \frac{S_b}{D} [n(d,t) - n_0], \end{aligned} \quad \text{Eq. (2)}$$

where n_0 is the equilibrium carrier concentration (about 10^{14} cm^{-3}), S_f and S_b are *surface non-radiative recombination velocities* on the irradiated (front) and back sides, respectively. S_f and S_b depend on the densities of non-radiative defects on the front and back sides. The same surface defect density N_s on the both sides is assumed and the following simple reaction can be written [21,27]

$$S_f = S_b = \sigma v N_s, \quad \text{Eq. (3)}$$

where σ and v are the recombination cross section and the thermal velocity of carrier respectively.

The transient of the PL intensity $I_{PL}(t)$ is given by

$$I_{PL}(t) = \beta \int_0^d n^2(x,t) dx. \quad \text{Eq. (4)}$$

Equation (1) can be solved numerically by applying Eqs. (2) and (3). The following values of constant were used: $D = 15 \text{ cm}^2/\text{s}$ [21, 23], $\beta = 3 \times 10^{-15} \text{ cm}^3/\text{s}$ [28], and $\gamma = 2 \times 10^{-30} \text{ cm}^6/\text{s}$ [27,28]. For Eqs. (3) a constant room temperature ($v = 10^7 \text{ cm/s}$) and the existence of

only surface dangling bonds ($\sigma = 10^{-15} \text{ cm}^2$) [23] are assumed. The main part of the calculations for c-Si is performed for the experimentally important case of excitation with a nitrogen laser ($\tau_p = 0.5 \text{ ns}$, $h\nu_p = 3.7 \text{ eV}$).

Dittrich et al. [24] stated that in order to describe correctly the time dependent distribution of the excess carrier distribution ($\delta_n(x,t)$) and PL intensity, the surface recombination velocity (S_o , named S_b in Eq. (3)) has to be known. Their calculated PL transients were obtained by optimizing so, see Fig. 1.13.

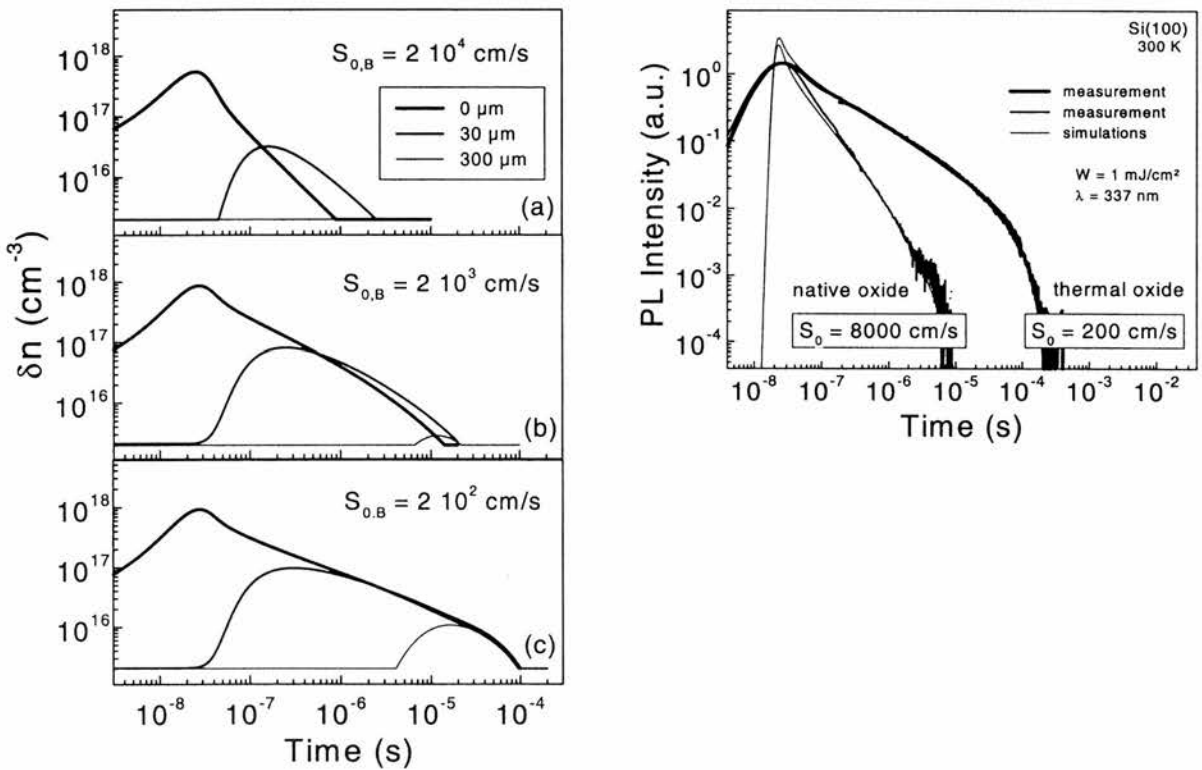


Fig. 1.13 Simulated time dependent excess carrier concentration at the Si surface for different surface recombination velocities is presented (left). Measured (thick lines) and simulated (thin lines) PL transients (right), where the best fits were obtained for $S_o=8000 \text{ cm/s}$ (native oxide) and $S_o=200 \text{ cm/s}$ (thermal oxide) [24].

Fig. 1.14a shows PL transients of different samples, which have different values of, interface state density (D_{it}) [22]. The values of the PL lifetime (τ_{PL}) for the samples with the D_{it} from 10^{11} to 10^{12} $\text{eV}^{-1}\text{cm}^{-2}$ range between 18 and 5 μs . These lifetimes will be in agreement with the values of τ_{PL} evaluated from the simulated transients if supposing $N_s \approx \Delta E \cdot D_{it}$, where $\Delta E \approx 1$ eV is a specific energy interval of the location of the surface states (nearly the forbidden band gap of c-Si). The lifetime of the exponential decay of PL decreases strongly with increasing D_{it} . The measured integrated PL intensity is presented as a function of D_{it} , Fig. 1.14b [22]. The total yield of PL is proportional to $(D_{it})^{-1}$ in the range of two orders of magnitude. This curve can be used as calibration curve for determination of D_{it} of unknown samples [22]. Therefore, it verifies the assumption of the simple relation between the N_s and D_{it} [22]. It should be noted that the measurement of the time integrated PL signal only provides information regarding the relative change of the gap state density, D_{it} .

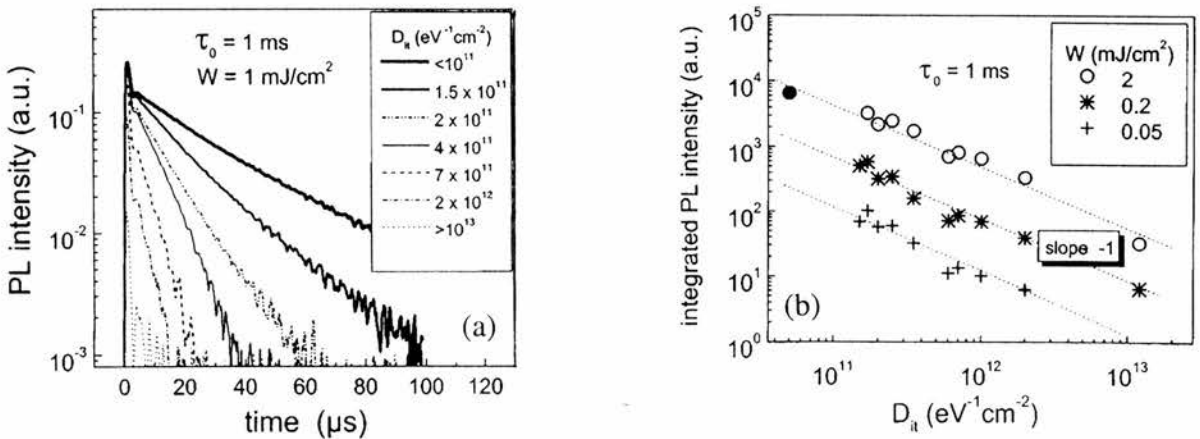


Fig. 1.14. (a) Measured PL transients of c-Si wafers ($\tau_0 = 1$ ms) with different D_{it} (from 10^{11} to 10^{13} cm^{-2}) under nitrogen laser excitation with $W = 1$ mJ/cm^2 . (b) Integrated PL intensity of the measured PL transients as a function of D_{it} [22].

1.6 Silicon devices:

1.6.1 A historical review

Since the invention of the bipolar transistor in 1947, the semiconductor device field has grown rapidly. The unique electrical properties of semiconductors permit their use in devices (diodes and transistors are two simple examples) to perform specific electronic function. Vast numbers of extremely small circuits, each consisting of numerous electronic devices, may be incorporate onto a small silicon “chip”. The invention of semiconductor devices, which has given rise to miniaturized circuitry, is responsible for the advent, worth and extremely rapid growth of a host of a new industries at the end of the last century. The semiconductor industry has been so successful in providing continued system performance improvement year after year that the Semiconductor Industry Association (SIA) has been publishing roadmaps for semiconductor technology since 1992 [29].

The simplest electronic devices may be the diode or rectifier that allows the current to flow in one direction only. That is a p - n junction semiconductor constructed from a single piece of semiconductor which is doped so as to be n -type on one side and p -type on the other, see Fig. 1.15.

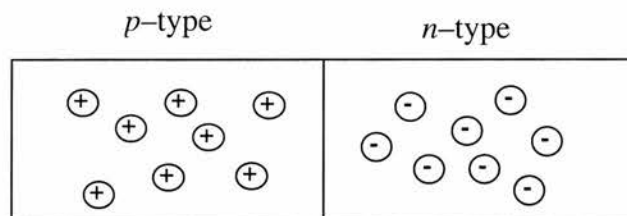


Fig. 1.15 p - n rectifying junction with representations of electrons and holes.

Transistors, which are extremely important semiconducting devices in microelectronic circuitry nowadays, are capable of two primary types of function. First, they can amplify an electrical signal and second, they serve as switching devices in computers for the processing and storage of information [19]. Richman [30], describes a simple phenomenon, commonly referred to as the surface field effect, relate to transistors as follow: “if a highly conductive electrode is brought in very close proximity to the surface of a highly doped semiconductor substrate, a voltage applied to the electrode with the respect to the substrate can have a pronounced effect on the electronic properties of the semiconductor surface. In particular, if *n*-type silicon is used as the substrate material, the application of a large positive voltage to the conducting electrode will attract an increased concentration of negative mobile charges (electrons) to the silicon surface and the surface become accumulated. On the other hand, if a negative voltage is applied to the electrode, the electrons will be repelled from the silicon surface, and the region near the surface become totally depleted of mobile charge, although non-mobile positive charges will remain there in the form of ionized donor-type impurities. If the magnitude of the applied negative voltage is increased, mobile positive charges (holes) will be attracted to the surface, forming a conductive layer in which the holes will be majority carriers. In this case, the silicon surface is said to be inverted”. This is the underlying principle behind the operation of metal–oxide–semiconductor (MOS) field effect transistors (FETs) and other related insulated–gate electronic devices.

The operation of a MOSFET, as shown in Fig. 1.16, is based on the fact that the conductivity of the channel is varied by the presence of an electric field imposed on the gate. So, a positive field on the gate will drive charge carriers (in this case holes) out of the channel, thereby reducing the electrical conductivity. Thus, a small alteration in the field at

the gate will produce a relatively large variation in current between the source and the drain.

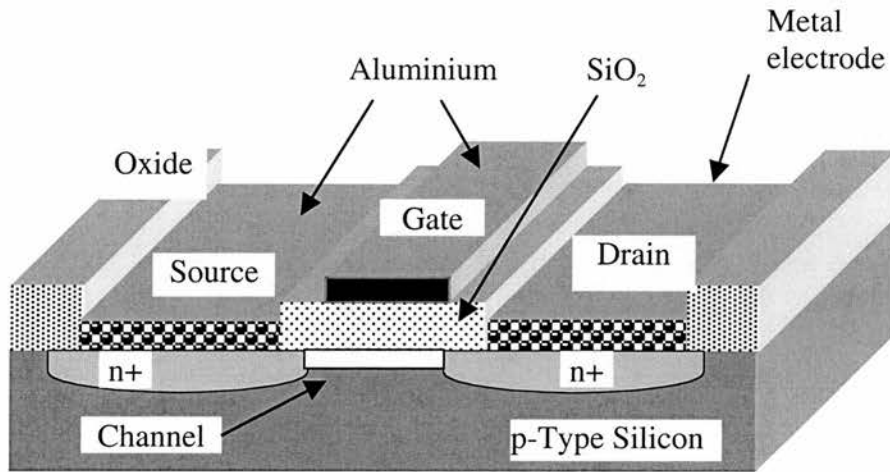


Fig. 1.16 Schematic diagram of a MOSFET.

1.6.2 The future

The phenomenal progress signified by Moore's law, stated as the doubling of transistor performance and quadrupling of the number of devices on a chip every three years, has been achieved through scaling of the MOSFET from larger physical dimensions to smaller physical dimensions, thereby gaining speed and density. But, shrinking the conventional MOSFET beyond the 50-nm-technology node requires innovations to circumvent barriers to the fundamental physics that constrains the conventional MOSFET [31]. The limits most often cited [32] are 1) quantum-mechanical tunnelling of carriers through the thin gate oxide; 2) quantum-mechanical tunnelling of carriers from source to drain, and from drain to the body of the MOSFET; 3) control of the density and location of dopant atoms in the MOSFET channel and source/drain region to provide a high on-off current ratio; and 4) the finite subthreshold slope. Knowing those limits, the device

performance may be improved by 1) inducing a large charge density for a given gate voltage drive; 2) enhancing the carrier transport by improving the mobility, saturation velocity, or ballistic transport; 3) ensuring device scalability to achieve a shorter channel length; 4) reducing parasitic capacitances and parasitic resistances. These options generally fall into two categories; new materials and new devices structures. Therefore, areas of device physics and materials science must be better understood in order to advance in technology.

1.7 Organic semiconductors

1.7.1 Historical introduction.

Organic semiconductors have been studied since the late 1940s [33]. Insulating organic materials are widely used in the electronic industry, mainly for microlithography and encapsulation. Several attempts to use organic semiconductors as the active component in electronic and electro-optical devices have been reported in the past. Earlier works were mainly concerned with the photovoltaic effect, with a view to realizing cheap organic solar cells [34]. Because their high optical absorption in the visible range, organic dyes such as merocyanines [35] and phthalocyanines [36] were the most studied compounds. Organic photovoltaic cells have also been fabricated with the conjugated polymers polyacetylene, poly(N-vinyl carbazole) and various derivatives of polythiophene. Interest in these polymers arose from the discovery of some intriguing properties, the most spectacular being the increase of their electrical conductivity by several orders of magnitude upon doping with an electron donor or acceptor [37]. However, until recently they had failed to have a significant practical impact in optoelectronic applications, despite the fact that a very large number of experimental and theoretical studies have been published [38].

The initial demonstration of organic electroluminescent diodes [39, 40] and organic thin-film transistors (OTFTS) [41,42,43] based on either small organic molecules [39,42] or conjugated polymers [40,41,43], and the impressive improvements in performance, and efficiency of organic devices during the last decade [44,45,46] attracted the interest of industry and opened the way to practical applications for organic semiconductors.

Non-traditional materials such as conjugated organic molecules, short-chain oligomers, longer-chain polymers, and organic-inorganic composites are being developed that emit light, conduct current, and act as semiconductors [47]. The ability of these materials to transport charge (holes and electrons) due to the π -orbital overlap of neighbouring molecules provides their semiconducting and conducting properties. The self-assembling or ordering of these organic and hybrid materials enhances this π -orbital overlap and is key to improvements in carrier mobility. The recombination of the charge carriers under an applied field can lead to the formation of an exciton that decays radiatively to produce light emission.

Recently, there has been much interest in the electronic and optoelectronic properties of polyaromatic hydrocarbons, such as tetracene, pentacene and perylene, because their potential use as organic laser, OLEDs, and OFETs [48,49,50]. Research efforts on semiconducting conjugated organic thiophene oligomers [51, 52], and pentacene molecule [48,53] have led to improvements in the mobility of these materials by five order of magnitude over the past 15 years. Also the study of the growth and optoelectronic characteristics of planar stacking molecules such as polycyclic aromatic compounds based on perylene. In particular, a molecular system based on perylene -3,4,9,10 perylene tetracarboxylic dianhydride (PTCDA)- has been world widely studied focusing on the

fundamental interactions on a variety of substrates to better understand the factors that may affect molecular ordering [54,55,56].

Therefore, in the present work a detailed study of some organic semiconductor molecules, including maleic anhydride, perylene, 3,4,9,10 perylene tetracarboxylic dianhydride and tetracene, is presented. Brief descriptions of those molecules considered in the present study are given next.

1.7.2 Maleic Anhydride

Maleic anhydride ($C_2H_2-C_2O_3$) is a 5-membered planar heterocyclic species with a C=C double bond as shown in the Fig. 17.

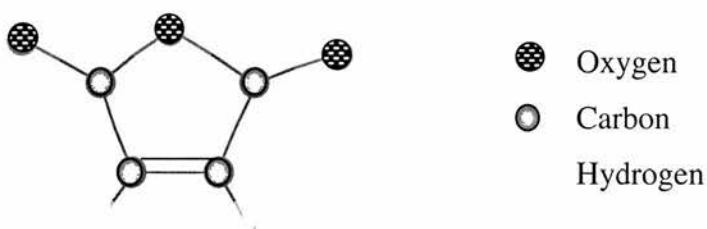


Fig. 1.17 Schematic model of maleic anhydride.

1.7.3. Perylene

Perylene, $C_{20}H_{12}$, crystallizes in the monoclinic system with four molecules in the unit cell. The molecule is of D_{2h} symmetry and one of the simplest examples of a type of polynuclear aromatic hydrocarbon, which contains formally single bonds in this case linking two naphthalene units. The Van Der Waals dimensions are $8.71 \text{ \AA} \times 11.25 \text{ \AA}$.

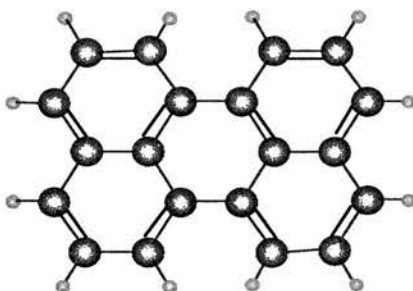


Fig. 1.18 Schematic model of perylene

1.7.4 Perylene –3,4,9,10-Tetra-Carboxylic-Dianhydride

PTCDA is a planar, organic, perylene-based molecule that form Van der Waals' bonded molecular crystals. PTCDA films can be grown in vacuum with a high degree of orientation to the substrate in spite of a very large lattice mismatch [57,58] Fig. 19 shows the schematic of the PTCDA molecule. The Van Der Waals size is: 8.64 Å x 13.86 Å.

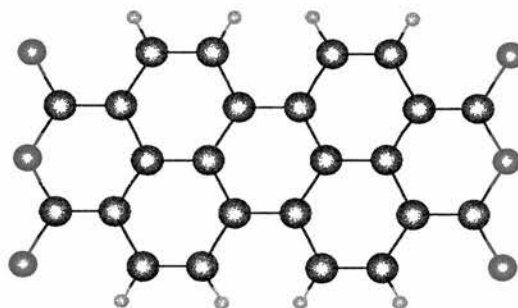


Fig. 1.19 Schematic model of PTCDA.

1.7.5 Tetracene

The tetracene molecule $C_{18}H_{12}$ is a planar molecule where four aromatic rings form a linear array, see Fig. 1.20. This molecule consists of strongly bonded aromatic molecules arranged on a crystal lattice with weak Van Der Waals intermolecular bonds. Also,

tetracene molecule has the 2-fold symmetry, D_{2h} . The molecular lattice is suggested to be easily polarizable, so it has been suggested for polyacenes [59]. The Van Der Waals' size of the molecule is $13.63 \text{ \AA} \times 6.99 \text{ \AA}$.

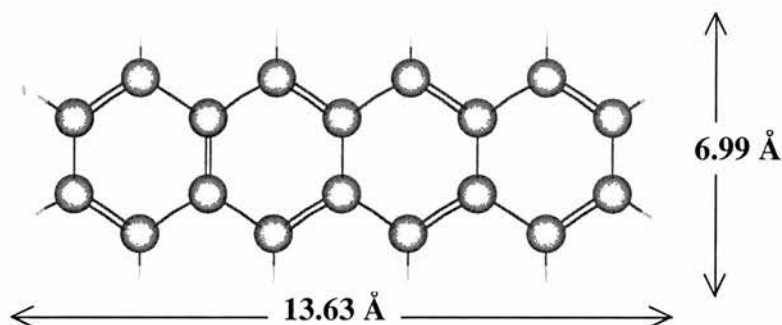


Fig. 1.20 Schematic model of tetracene with the Van Der Waals dimensions.

References

- 1 R. A. Wolkow, *Annu. Rev. Phys. Chem.* **50**, 413 (1999).
- 2 J. Yates, H. Neegaard. *Chem. Rev.* **95**, 1589 (1995).
- 3 L. Brillouin, *Wave Propagation in Periodic Structure*, 2nd ed., Dover, New York, 1963.
- 4 J. M. Ziman, *Electrons and Phonons*, Clarendon, Oxford, 1960.
- 5 H. Luth, *Appl.Phys.* **8**, 1 (1975).
- 6 D. Haneman, *Rep. Prog. Phys.* **50**, 1045 (1987).
- 7 . K. Takayangi, Y. Tanishiro, M. Takahashi. S. Takahashi, *Surf. Sci.* **164**, 367 (1985).
- 8 H. Luth, *Surface and Interfaces of Solids*, Spring-Verlag (Berlin Heidelberg New York) 1993.
- 9 M. J. Cardillo G. E. Becker, *Phys. Rev. B* **21**, 1497 (1980)
- 10 J. Ihm, D. H. Lee, J. D. Joannopoulos, J. J. Xiong, *Phys. Rev. Lett.* **51**, 1872 (1983).
- 11 M. Aona, Y. Hou, C. Oshima, Y. Ishizawa, *Phys. Rev. Lett.* **49**, 567 (1982).
- 12 H. Wang, R. Lin, X. Wang. *Phys. Rev. B* **36**, 7712 (1987).

-
- 13 Z. Zhu, N. Shima, M. Tsukada, Phys. Rev. B **40**, 11868 (1989).
- 14 M. Nishida, Phys. Rev. B **58**, 7103 (1998)
- 15 D. J. Chadi, Phys. Rev. Lett. **43**, 43 (1979).
- 16 R. J. Hamers, Y. Wang. Chem. Rev. **96**, 1261. (1996).
- 17 R. J. Hamers, R. M. Tromp, J. E. Demuth. Surf. Sci. **181**, 246. (1987).
- 18 R. A. Wolkow, Phys. Rev. Lett. **68**, 2636 (1992).
- 19 W. D. Callister, Jr. Materials Science and Engineering, Ch. 19. John Wiley & Sons, Inc. USA (1997).
- 20 J. R. Chelikowsky, M.L. Cohen, Phys. Rev. B **16**, 556 (1976).
- 21 L. C. Kimerling, K. D. Kolenbrander, J. Michel, J. Palm, in Solid State Physics. Advances in Research and Applications, edited by H. Ehrenreich and F. Spaepen (Academic, New York, 1997), Vol 50, p.333.
- 22 V. Y Timoshenko, A. B. Petrenko, M. N. Stolyarov, Th. Dittrich, W, Fussel, J. Rapich, J. Appl. Phys. **85**, 4171 (1999).
- 23 V. Y Timoshenko, J. Rapich, Th. Dittrich, Jpn. J. Appl. Phys., Part 2 **36**, L58 (1997).
- 24 Th. Dittrich, T. Bitzer, T. Rada, V. Yu. Timoshenko, J. Rappich, submitted to Solid State Electron. 2002
- 25 Th. Dittrich, V. Y Timoshenko, J. Rapich, Appl. Phys. Lett. **70**, 2705 (1997).
- 26 M I Galant H. M. van Driel, Phys. Rev. B **26**, 2133 (1982).
- 27 E. Yablonovich, D. L. Alara, C. C. Chang, T. Gmitter T. B. Bright, Phys. Rev. Lett. **57**, 249 (1986).
- 28 V. Grivickas J. Linnros, Thin Solid Films **255**, 70 (1995).
- 29 H. S. P. Wong, *Progress in Digital Integrated Electronics*, IEDM Tech. Digest, pp. 11–13 (1975).

-
- 30 P. Richman, *MOS Field-Effect Transistors and Integrated Circuits*, John Wiley & Sons New York, pp. 1-3 (1973).
- 31 H. S. P. Wong, *IBM J. R&D.* **45**, 133 (2002).
- 32 P. Packan, *Science* **285**, 2079 (1999); B. Hoeneisen, C. A. Mead, *Solid State Electron.* **15**, 819 (1972); J. Meindl, *Proc. IEEE* **83**, 619 (1995); D. Frank, R. Dennard, E. Nowak, P. Solomon, Y. Taur, H. S. Wong, *Proc. IEEE* **89**, 259 (2001); R. W. Keyes, *Proc. IEEE* **89**, 227 (2001).
- 33 M. Pope, C. E. Swenberg, *Electronic Processes in Organic Crystals and Polymers*, 2nd ed. Oxford University Press, Oxford 1999, pp.337-340.
- 34 See for instance, A. L. Fahrenbruch, R. H. Bube, *Fundamentals of Solar Cells: Photovoltaic solar energy conversion*, Academic Press, NY (1983).
- 35 F. Wurthner, R. Wortmann, R. Matschiner, K. Lukaszuk, K. Meerhulz, Y. DeNardin, R. Bittner, C. Brauchle, *R. Sens. Angew. Chem. Int. Edit.* **36**, 2765 (1997).
- 36 *Phthalocyanines: Properties and Applications*, C. C. Leznoff, A. B. P. Lever, Eds., VCH Publishers, New York (1989).
- 37 G Horowitz, *Adv. Mater.* **6/7**, 287 (1990).
- 38 C. D. Dimitrikopoulos, P. R. L. Malenfant, *Adv. Mater.* **14**, 99 (2002).
- 39 C. W. Tang, S. A. van Slyke, *Appl. Phys. Lett.* **51**, 913 (1987).
- 40 J. H. Burroughes, D. D. Bradley, A. R. Brown, R. N. Mark, K. Mackay, R. H. Friend, P. L. Burn, A. B. Holmes, *Nature* **347**, 539 (1990).
- 41 F. Ebisawa, T. Kurokawa, S. Nara, *J. Appl. Phys.* **54**, 3255 (1983).
- 42 K. Kudo, M. Yaashima, T. Moriizumi, *Jpn. J. Appl. Phys.* **23**, 130 (1984).
- 43 A. Tsumura, H. Koezuja, T. Ando, *Appl. Phys. Lett.* **49**, 1210 (1986)

-
- 44 C. D. Dimitrikopoulos, B. K. Furman, T. Graham, S. Hedge, S. Purushothaman, *Synth. Met.* **92**, 47 (1998).
- 45 R. H. Friend, J. H. Burroughes, T. Shimoda, *Phys. World* **12**, 35 (1999).
- 46 S. Forrest, *MRS Bull.* February, 108 (2001).
- 47 J. M. Shaw, P. F. Seidler, *IBM J. R&D.* **45**, 3 (2001).
- 48 J. H. Schon, Ch. Kloc, A. Dodabalapur, B. Batlogg, *Science* **289**, 599 (2000).
- 49 B. Crone, A. Dodabalapur, Y. Y. Lin, R. W. Filas, Z. Bao, A. LaDuca, R. Sarpeshkar, H. E. Katz, W. Li, *Nature* **403**, 521 (2000).
- 50 J. H. Schon, S. Berg, Ch. Kloc, B. Batlogg, *Science* **287**, 1022 (2000).
- 51 G. Horowitz, D. Fichou, X. Peng, Z. Xu, F. Garnier, *Solid State Commun.* **72**, 381 (1989).
- 52 F. Garnier, R. Hajlaoui, A. Yasser, P. Srivatava, *Science* **265**, 1684 (1994).
- 53 C. D. Dimitrikopoulos, S. Purushothaman, J. Kymissis, A. Calleggeri, J. M. Shaw, *Science* **283**, 822 (1999).
- 54 C. Ludwig, B. Gompf, J. Petersen, R. Strohmaier, W. Eisenmenger, *Z. Phys.* **B93**, 365 (1994).
- 55 Y. Hirose, S. R. Forrest, A. Kahn, *Phys. Rev. B* **52**, 14040 (1995).
- 56 F. S. Tautz, S. Sloboshanin, V. Shklover, R. Scholz, M. Sokoloswki, J. A. Schaefer, E. Umbach, *Appl. Surf. Sci.* **166**, 363 (2000); M. Tengelin–Nilsson, L. Ilver, J. Kanski, *Surf. Sci.* **464**, 265 (2000).
- 57 M. Mobus, M. Schreck, N. Karl. *Thin Solid Films* **175**, 89.(1989)
- 58 M. Mobus, N. Karl, T. Kobayashi. *J. Cryst. Growth.* **116**, 495.(1992).
- 59 W. Warta, N. Karl, *Phys. Rev. A* **36**, 163 (1985).

CHAPTER 2.

Experimental Techniques

2.1 Introduction

The development of surface science is intimately related, from an experimental point of view, to the ultrahigh vacuum (UHV) techniques. The preparation of well-defined surfaces with negligible contamination requires ambient pressures lower than 10^{-10} Torr ($= 10^{-10}$ mbar). Typical modern UHV instruments were used in the development of the present work, see Fig. 2.1.

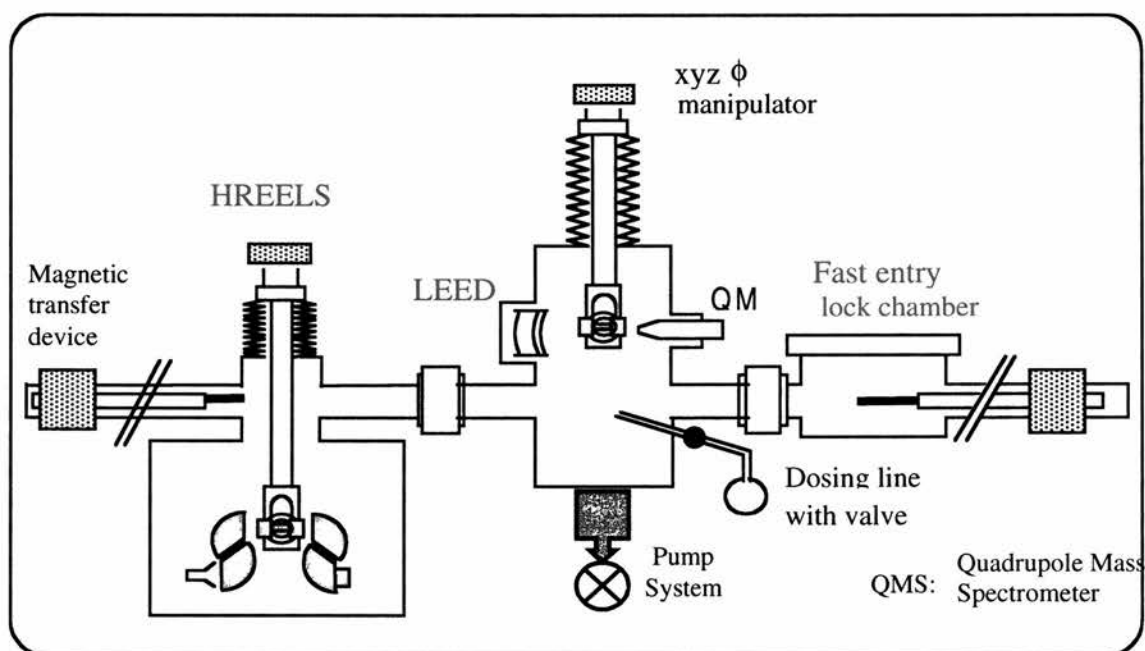


Fig. 2.1 Schematic diagram of the UHV system used to carry out some of the experiments involved in the present work.

The first system consists of two-stage of stainless-steel vessels, the preparation and analysis chambers equipped with low electron energy diffraction (LEED), high

resolution electron energy loss spectroscopy (HREELS), quadrupole mass spectrometer (QMS) and dosing facilities. The second UHV system consists of three interlinked chambers equipped with LEED, vt-STM, reflectance absorption infrared spectroscopy and dosing facilities.

2.2 Scanning tunnelling microscopy

A scanning tunnelling microscopy is essentially an arrangement to bring a sharpened tip, usually tungsten or platinum-iridium alloy, to within $5 - 10 \text{ \AA}$ of the surface under investigation [1]. At such distances, the wavefunctions of the tip and surface overlap, allowing a tunnelling current to flow between them when a bias is introduced. By controlling the small bias, typically a few volts for semiconductors, the direction of this tunnelling current can be chosen. A positive (negative) bias applied to the sample allows charge to flow from (to) occupied (empty) states on the tip to (from) empty (filled) states on the sample. The tip is mounted on a piezoelectric scanner that allows it to be translated in three orthogonal directions, see Fig. 2.2.

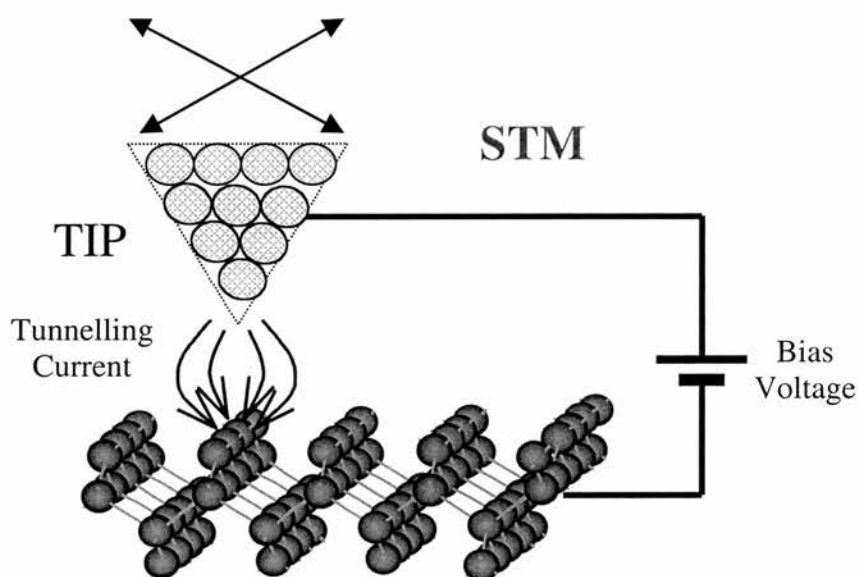


Fig. 2.2 Schematic representations of STM.

The spectroscopy capability of STM, combined with its high spatial resolution, is perhaps the most important feature of STM and has been applied widely, particularly for investigation of semiconductor surfaces [2,3,4]. In principle, STM has to be considered primarily as a spectroscopic method due to its inherent bias-dependence. Besides this, in the tunnelling current, there exists a distance-dependence (apparent barrier height). The expression for this current, in the one-dimensional formalism, is:

$$I \propto U_T \exp(-A\phi^{1/2}s) \quad \text{Eq. (1) [5]}$$

where I is the current, U_T is the voltage, A is a constant, ϕ the work function, and s the distance between tip and sample. The value of A is typically such that the current changes by an order of magnitude for a 5 Å change in the distance.

It is widely observed that at high bias, and particularly for semiconductor samples, the bias-dependence of the tunnelling current generally does not exhibit an Ohmic behaviour, i.e. constant current STM images can depend critically on the applied bias [6].

At fixed bias, the experiment has two forms. Firstly, in the constant current mode, a feedback circuit changes the height of the tip in order to keep the current constant. Secondly, in the constant height mode, the tip is scanned at constant height above the surface while the current variations are recorded. Fig. 2.3 shows the modes of operation of a scanning tunnelling microscope.

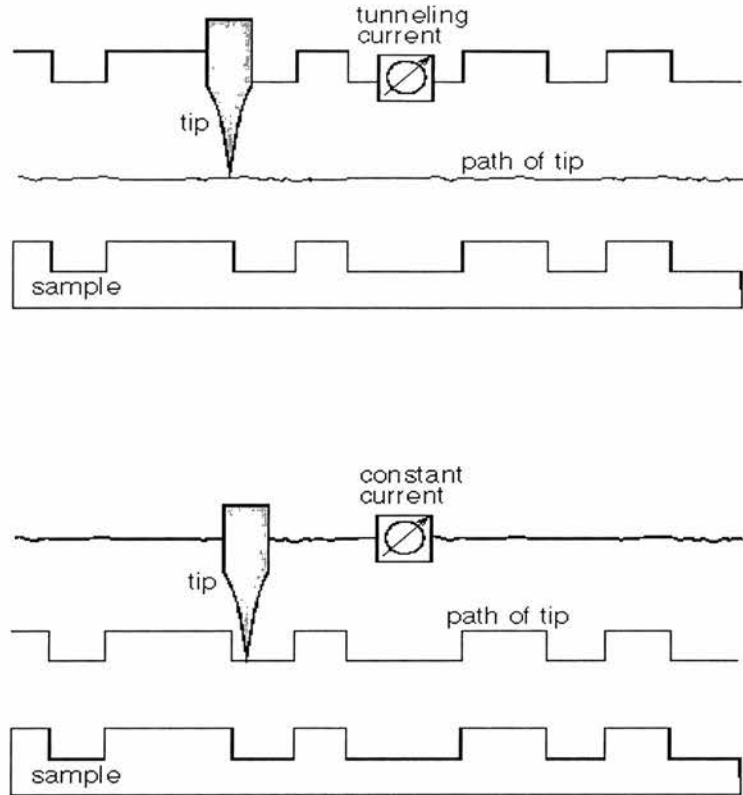


Fig. 2.3 Modes of operation of STM. Above is presented the constant height mode, while the constant current mode appears below [7]

With scanning tunnelling spectroscopy, STS, the bias dependence of the tunnelling current is studied in detail at fixed tip position in order to obtain information regarding the local electronic structure. There, a high frequency sinusoidal modulation voltage is superimposed on the constant d.c. bias voltage applied between tip and sample [8]. The modulation frequency is chosen higher than the cut-off frequency of the feedback loop, which keeps the average tunnelling current constant. By recording the tunnelling current modulation, which is in phase with the applied bias voltage modulation, by means of a lock-in amplifier, a spatially resolved spectroscopic signal dI/dU can be obtained simultaneously with the constant current image [9]

$$\frac{dI}{dU}(U) \propto en_t(0)n_s(eU)T(eU, eU) + \int_0^{eU} n_t(\pm eU \pm \varepsilon)n_s(\varepsilon) \bullet \frac{dT(\varepsilon, eU)}{dU} d\varepsilon \quad \text{Eq. (2)[10]}$$

where n represents the density of states, ε is the energy, and T is the transmission coefficient. Subscripts t and s represent tip and sample respectively.

At a fixed location, the increase of the transmission coefficient with applied bias voltage is smooth and monotonic. For that reason, features in dI/dU curve can usually be attributed to structures in the state density via the first term in Eq. (2). However, interpretation of the spectroscopy data dI/dU as a function of position (x,y) is more complicated.

In the low-bias limit, where the tunnel junction exhibits an Ohmic behaviour, Eq. (2) can be simplified to

$$dI/dU = I/U$$

therefore, for a constant tunnelling current I , the quantity dI/dU increases steadily like I/U as U approaches zero. This I/U background, on which the desired electronic structure information is superimposed, makes it difficult to observe structure in the dI/dU data at low bias voltages, thereby preventing investigation of the electronic structure near the Fermi level. However, breaking the feedback circuit for a certain time interval at selected surface locations by means of a sample-and-hold amplifier while local $I-U$ characteristics are recorded can eliminate the divergence [11]. Therefore, band-gap states in semiconductors, for instance, can be probed without difficulties. The first derivative dI/dU can be obtained from the measured $I-U$ curves by numerical differentiation. The dependence of the measured spectroscopic data on the value of the *tunnelling conductance* I/U can be compensated by normalising the *differential conductance* dI/dU to the total conductance I/U . Then, the normalised quantity

$(dI/dU)/(I/U) = (d \ln I)/(d \ln U)$ reflects the electronic density of states DOS reasonably well [12]. However, the close resemblance of the $(d \ln I / d \ln U) - U$ curve to the electronic DOS is generally limited to the position of peaks while peak intensities can differ significantly.

The chemical information that has been sought in STS as in other techniques has not been compositional in nature but electronic, i.e. in terms of local densities of state and such surface feature as dangling bonds. Finally, information on the DOS is not only of fundamental importance but is needed for an accurate interpretation of the constant current topographies and may be used to study electronic effects upon metal atom adsorption [13].

Riviere [14] mentioned that “under certain conditions of applied voltage, surface reactivity, surface reconstruction, etc., the STM image will be a complex convolution of electronic and topographical features, and in some cases there will therefore almost certainly not be one-to-one correspondence between the image and topography”.

2.3 Scattering from surfaces.

The scattering process at a surface, in general, is a central topic in among the various interaction of a solid. Like in bulk solid-state physics, elastic scattering can tell us something about symmetry and the geometry arrangement of atoms near the surface, whereas inelastic scattering process, where energy quanta are transferred to or from topmost atomic layers of a solid, yield information about possible excitations of the surface or interface, both electronic and vibronic ones. In principle, all kinds of particles, x-rays, electrons, atoms, molecules, ions, neutrons, etc. can be used as probes. The only prerequisite in surface and interface science is the required surface sensitivity.

The geometry and possible excitations of about 10^{15} surface atoms per cm^2 must be studied against the background of about 10^{23} atoms present in a bulk volume of one cm^3 . In surface and interface physics the appropriate geometry for a scattering experiment is thus the reflection geometry. Furthermore, only particles that do not penetrate too deeply into the solid can be used. Atoms and molecules with low energy interact only with the outermost atoms of a solid, and low-energy electrons generally penetrate only a few angstroms into the material. Some electron scattering processes are described in more detail in the next sections.

2.4 Low energy electron diffraction

As an electron beam of energy around 150 eV has a wavelength of 1 Å, it is suitable for electron diffraction (Bragg diffraction) experiments on crystal surfaces [15]. This energy is roughly at the minimum in the universal pathlength curve, giving these electrons optimum surface sensitivity. The elastic backscattering of low energy electrons incident normally on a crystal surface forms the basis of the technique of Low Energy Electron Diffraction (LEED). LEED is a complementary technique capable of providing structural information at surface level. This technique readily gives information about the symmetry of the surface atomic arrangement, in cases where a surface has some long range order. In that case, we would know the size and the shape of the repeat unit on the surface (the surface unit cell).

A typical arrangement used in a LEED experiment is shown in Fig. 2.4. An electron beam of monochromatic but variable energy is produced by an electron gun, and is directed towards the sample. The electrons are then backscattered from the sample surface onto a system of hemispherical grids surrounding the electron gun.

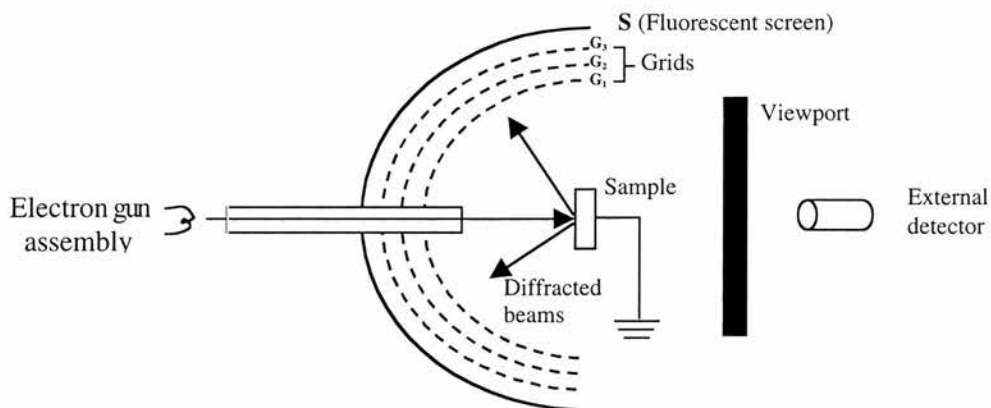


Fig. 2.4 Schematic arrangement used in LEED.

The backscattered electrons are of the two types; elastically scattered electrons forming a set of diffracted beams which create the LEED pattern, and inelastically scattered electrons, which may make up 99% of the total flux, but which are not required. After reaching the first grid, G_1 , which is earthed, the elastically scattered electrons are accelerated towards the fluorescent screen, S, which carries a high positive potential (of the order of 5 keV). This provides the electrons in the diffracted beams with enough energy to excite the fluorescence in the screen, so that a pattern of bright LEED spots is seen. Fig. 2.5 shows a reconstructed Si(111)- 7×7 LEED pattern after flashing until 1200 K. On the other hand, the inelastically electrons are scattered through wide angles and produce a relatively homogeneous background illumination of the screen, which is suppressed by giving the middle grid a somewhat negative bias and thus prevented from reaching the screen.

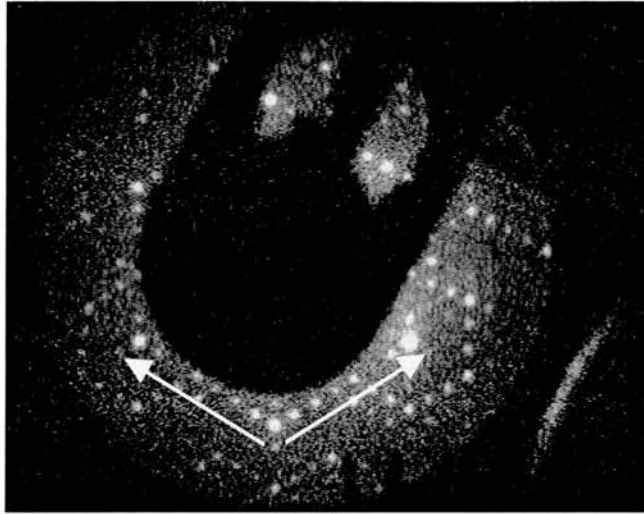


Fig. 2.5 LEED pattern of Si(111)-7x7. The arrows are aligned parallel to 7 spots in the reconstructed surface. The brighter spots are the principal diffraction spots.

The LEED pattern is a reflection of reciprocal space (a brief description of the reciprocal vectors is given in section 1.2.1). This means that the distance between adjacent points in the LEED pattern is inversely to the distance between points in the corresponding direction of the real surface unit mesh (the direct lattice). It is based on the Bragg reflection when the path length of two parallel rays (beam) reflected from adjacent planes (or atoms) is a multiple of the de Broglie wavelength ($\lambda = 2\pi / k$). This is so if $n\lambda = a \sin\theta \rightarrow \sin\theta = n\lambda/a$

where n is an integer, a is the distance between adjacent positions (planes or atoms) and θ is the reflection angle of the beam.

Additional information, such as location of the atoms within the unit mesh, may be obtained from analysis of both of the spot positions and their intensity profiles. However, the simple production of LEED pattern, without an analysis of the intensities of the individual spots, is by the far the most widespread use of a LEED. In many cases,

LEED is routinely used to check the cleanliness and order of surface being prepared for other experiments. Because of the sensitivity of LEED to surface contamination and surface roughness, in some cases, the appearance of a LEED pattern with bright, sharp spots is widely regarded as evidence of a completely clean and ordered surface [16].

2.5 High resolution electron energy loss spectroscopy

A molecule in the gas phase has $3N$ degrees of freedom of motion associated with it, i.e. vibrational $3N-6$ ($3N-5$), translational 3 and rotational $3(2)$, where N is the number of atoms of the molecule and the parenthesis refer to linear molecule. When that molecule meets a surface with which it interacts chemically so that adsorption occurs, there is then no possibility of translational or rotational degrees of freedom and all that remains are the vibrational degrees of freedom, either similar to, or modified from, the original molecular vibrations together with new vibrations related to frustrated translations and rotations. Vibrational modes are of low energy, generally less than 0.5 eV. If now an electron of low primary energy, typically 2-8 eV, approaches the surface with the attached molecule, it can interact with the vibrations of the molecule when it arrives within a certain distance of the surface, and be reflected (scattered) elastic or inelastically from the surface, see Fig. 2.6.

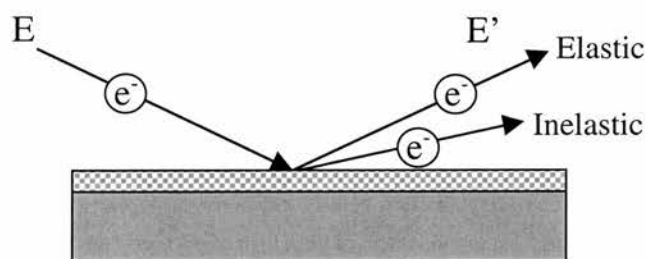


Fig. 2.6 Schematic diagram of the elastic and inelastic scattering processes of a low energy electron on a surface covered with a molecular thin film.

In the inelastic scattering processes the electron has lost a discrete amount of the energy corresponding to one or more of the characteristic vibrational frequencies. Analysis of the energy distribution of the scattered electron thus provides values of the characteristic frequencies and hence information about the way the molecule is attached to the surface.

High resolution electron energy loss spectroscopy (HREELS) measures the discrete energy losses due to the excitation of various vibrational modes of molecules adsorbed on surfaces. Since each of these modes has an associated characteristic energy, typically 5-500 meV, and with widths ~ 1 meV, it follows both that the primary exciting electron energy must be low and that the energy width must be reduced to as near the inherent vibrational modes width as possible. HREELS is therefore used to identify adsorbed species and to get information about adsorption sites and bonding geometry [17].

A tungsten filament operated at a typical temperature of 2200K emits electrons with a thermal spread of about 0.5 eV. But in practice, the electrons pass from such a filament through the same type of energy selector as is used to analyse electron energies, the selector in this case acting as an electron monochromator. See Fig 2.7.

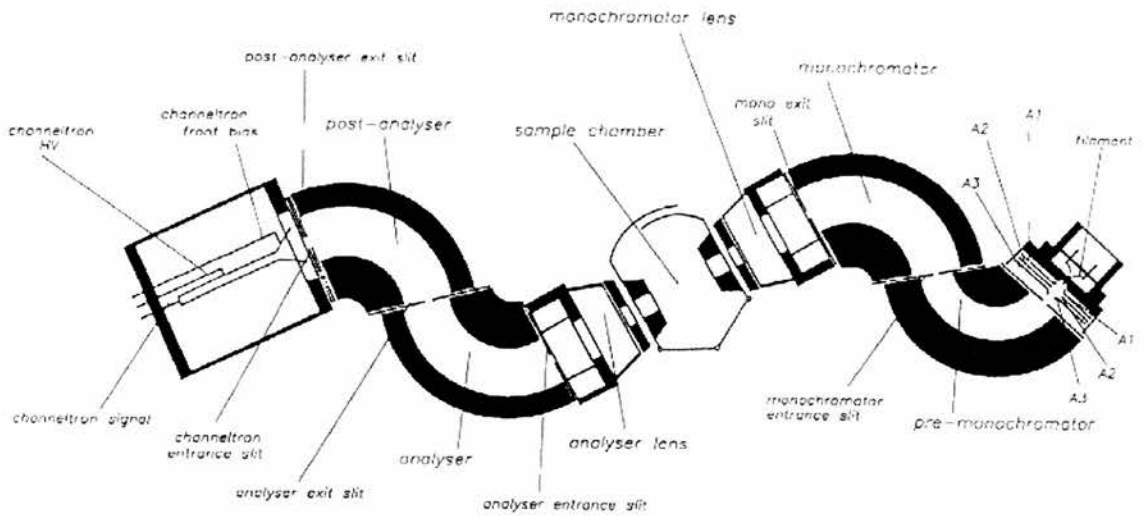


Fig. 2.7 Illustration of the VSW HIB 1000 double pass spectrometer, referred as *Ibach spectrometer*.

The HREELS system has typical performance parameters of primary energy variable from 2 to rarely higher than 8.0 eV, sample current about 2×10^{-10} A, and energy resolution at full-width-half-maximum, FWHM, in the elastically reflected peak of about 2-3 meV.

There are two basic mechanisms by which an electron can be scattered inelastically. Within a certain distance to the surface, it can interact with the dipole field associated with a particular surface vibration, e.g. either the vibrations of surface atoms of the substrate itself, or one or other of the characteristic vibrations of an adsorbed molecule. Alternatively the electron can be scattered inelastically from an atomic core at the surface, again either of a substrate or an adsorbate atom. The former is called *dipole scattering* and the latter *impact scattering*.

Most HREELS observations have been concerned with the first mechanism, that of dipole scattering. The reason for this are concerned with the dipole selection rules. The scattering process is regarded as taking place by either of two paths: an elastic Bragg reflection followed by interaction with the vibrating dipoles through the long-range Coulombic field, or vice versa. Since in conducting materials an electric field is generated normal to the surface when an electron is specularly reflected only those vibrations that can induce a dipole momentum change normal to the surface are excited: “normal dipole selection rule”. The consequence is that the current of inelastically dipole scattered electrons is peaked very close to the specular direction.

Alternatively, this can be described in terms of molecular properties rather than field of the electron, Fig. 2.8. Any dipole at surface induces an image dipole within the surface; if the dipole orientation is normal to the surface the field is enhanced by the image dipole, if the orientation is parallel to the surface the dipole field is cancelled by the image dipole. Thus, an orientation quasi-selection rule exists which strongly favours normally oriented dipoles [15].

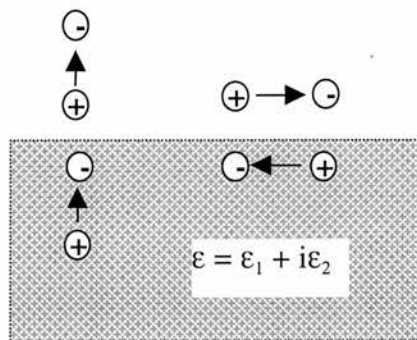


Fig. 2.8 Schematic illustration of the operation of the normal dipole selection rule in HREELS. Image dipoles within the surface either enhance (for normal orientation on the left) or negate (for parallel orientation on the right) the effect

of dipoles in the vacuum above the surface. There is therefore a selection rule that favours normally oriented dipoles [15].

2.6 Photoluminescence: Principle

Photoluminescence (PL) under pulsed excitation was proposed as a direct method of the characterisation of semiconductor surfaces [18]. The absorption of a photon by an atom or molecule can only occur if the photon energy is exactly equal to the difference between two existing energy levels of the system concerned. As a result of the absorption of the photon, the system is raised from the lower level (energy E_1) to the higher level (energy E_2). Thus for absorption to occur:

$$h\nu = E_2 - E_1$$

The vibrational and rotational motions of a molecule are quantized i.e., vibrational or rotational energy can be taken up or lost only in discrete quantum units. Thus the total energy of a particular state of a molecule may be represented as the sum of electronic excitation energy, E_e , the vibrational energy, E_v , and the rotational energy, E_r . So, the overall change of energy on absorption of a quantum of light may be represented as:

$$h\nu = \Delta E_e + \Delta E_v + \Delta E_r$$

The energy of an electronically excited state may be lost in a variety of ways. A radiative decay process is one in which a molecule discards its excitation energy as photon. A more common fate is a non-radiative decay, in which the excess energy is transferred into the vibration, rotation and translation of the surrounding molecules and eventually contributes to the heat bath. In the case of a radiative decay process, we will have luminescence, that is the emission of radiation (ultraviolet, visible, or infrared) as a

result of electronic excitation of a material, excluding any radiation that is purely the result of the temperature of the material (incandescence). The study of most kinds of luminescence can provide some information about the chemical composition of the emitting system and the process that takes place after the absorption of the excitation energy [19]. PL is one of the most informative because it allows greater degree of experimental control over the excitation process. By choice of the wavelength of the exciting light, the energy can be directed to specific components of the system so that the ensuing processes are simpler than if the energy is fed to the system as a whole.

The ultraviolet and visible regions of the spectrum are the most important for photochemistry. Absorption in those regions causes the excitation of the outermost electrons of the molecule, i.e., those responsible for chemical binding, and hence it may lead to chemical change. The same wavelength regions are of interest in the study of photoluminescence because this also requires prior excitation of one of the outermost electrons.

Figure 2.9 schematically shows the basic transitions in a semiconductor [20]. These transitions may be classified as follows. The first classification is the interband transition: (i) intrinsic emission corresponding very closely in energy to the bandgap, where phonons and excitons may be involved, and (ii) higher energy emission involving energetic or hot carriers. The second classification is the transition involving impurities or physical defects; (a) conduction band to acceptor, (b) donor to valence band, (c) donor to acceptor (pair emission), and (d) deep levels or recombination through electron-hole capture. The third classification is the intraband transition involving hot carriers, sometimes called deceleration emission [21].

Not all emission can occur in the same material or under the same conditions, and not all transitions are radiative. An efficient luminescent material is one in which radiative transitions predominate over non-radiative ones (such as Auger non-radiative recombination) [22]. Recombination of electron hole pairs at surface is caused by the presence of electronic states in the forbidden gap, which can act as traps or as recombination active centres.

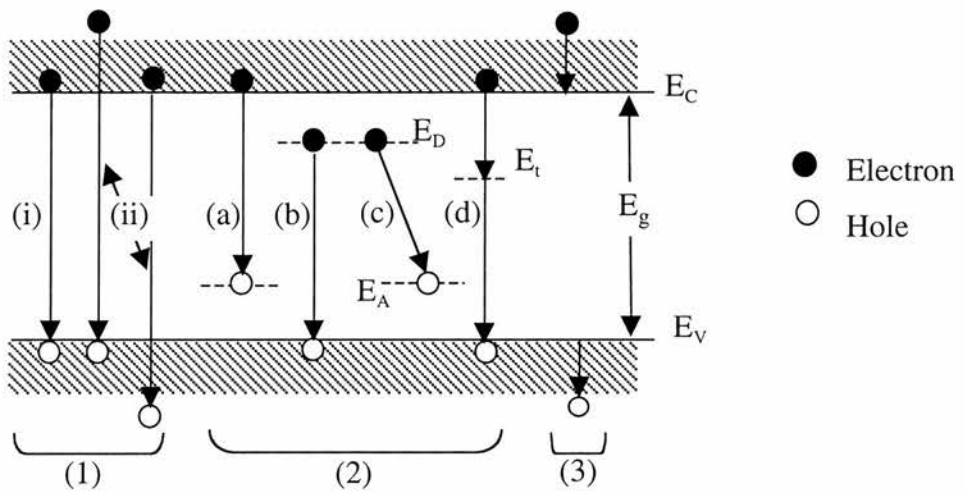


Fig. 2.9 Basic electronic transitions in a semiconductor [20].

2.7 *Ab initio* calculations

Ab initio calculations have become another important tool in research in the field of surface science. The discipline of computational *ab initio* quantum chemistry and physics is aimed at determining the electronic energies and wave functions of atoms, molecules, solids and all other chemical species, through an attempt to solve the electronic Schrödinger equation for the $E_k(\mathbf{R})$ energy surface and wave function $\psi_k(r, \mathbf{R})$ on a grid of values of the fixed nuclear positions [23].

In addition to the experiments in the present work, a series of *ab initio* calculations have been carried out using Gaussian 98 [24] and GAMESS [25]. Vibrational frequencies, molecular orbitals, orbital symmetries and energy have been calculated after a full optimization, including the use of the advanced hybrid density functional theory (DFT) [26] with the non-local Becke's three parameter function [27] to describe the exchange and correlation energy. For the last case, the three hybrid functional uses the LYP correlation functional and therefore referred as B3LYP.

2.8 Cleaning silicon procedure.

Silicon substrates were cleaned with trichlorethylene, acetone and ethanol, in an ultrasonic bath for 10 min, each time, as the first step. The samples are kept in ethanol solution before mounting in the sample holder. Inside the UHV conditions, silicon is prepared by a standard procedure [28], which consists of both sample and sample holder are typically degassed for several hours at temperatures below the SiO sublimation temperature (about 850 K), followed by thermal induced desorption of the native oxide layer at (1100 – 1200 K) by direct heating of the sample. The Si(100) sample conditions is monitored by LEED until a bright 2x1 pattern on a dark background is observed. In the HREEL spectra loss features were absent.

2.9 Hydrogen terminated surfaces

Just as hydrogen plays a prominent role in the chemistry of carbon in the entire field of organic chemistry, where H-C bonds predominate, the Si-H bond is equally important in the chemistry of silicon. Formation of the Si-H bond on the surface of a

silicon crystal provides a high degree of passivation of the surface chemistry of the silicon as a result of reaction with the dangling bond. In the processing of silicon surfaces, the role of the formation and destruction of the surface Si-H bond is often dominant in controlling the processes desired.

The standard method for hydrogenation of silicon surfaces involves etching in HF solutions [29], HF acid etching is a key step in producing silicon surfaces, which are almost contamination-free and chemically stable for subsequent processing in the semiconductor industry [30]. The structure of the H-terminated surface also plays a role in the initial stages of gate oxide formation and may affect the resulting Si/SiO₂ interfacial properties. Also, aqueous HF solutions (HF in H₂O of various concentrations) induce microscopic roughness on both Si (100) as well as Si (111). So varying the pH of the HF solutions drastically alters the microscopic roughness and the nature of the associated H termination of the surface. In particular, basic solutions produce ideally terminated Si (111) surfaces that are microscopically smooth [31]. In addition small triangular domains can be seen in STM images, Fig. 2.10.

A recipe for the procedure of etching is given below according to C Stuhlmann [32].

- Sample was cleaned with trichlorethylene, acetone and ethanol, afterwards intensively rinsed with purified (deionized) water at 18MΩ.
- Pre-etching of the oxidised sample in H₂O₂ : H₂O : HCl 1:1:4 for 5 min at 80°C.
- Sample was wet in buffered HF (pH 5) for 5 min at room temperature.
- Intensive water rinses.
- Oxidise the sample in H₂O₂ : H₂O : HCl 4:1:1 for 10 min at 80°C.
- Intensive water rinses.

- Oxide removal and terminated the surface with H (silicon monohydrides) by etching in concentrate NH_4F (pH 7.8) for 6.5 min at room temperature.
- Finally, intensive water rinses.

To reduce the risk of a contamination especially by hydrocarbons the sample was kept within the solution all times. Inside the UHV system, the sample is gently heated at 150°C for a smooth terminated surface.

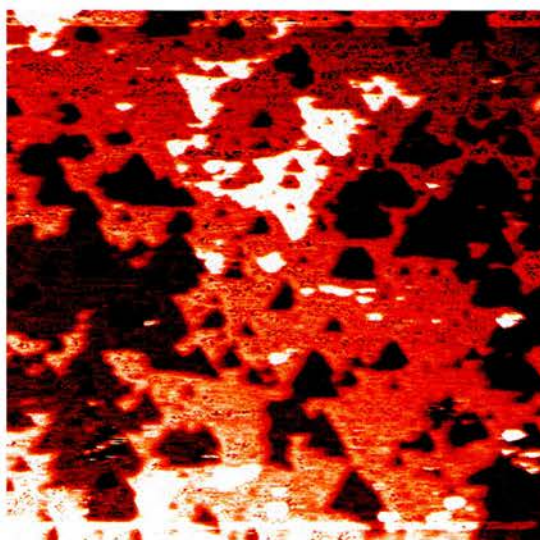


Fig. 2.10 STM image of the Si(111) surface passivated with hydrogen through wet etching.

2.10 The doser

In the present work, the doser used, for studying organic molecules, consists of a quartz tube, 7 cm length and 0.5 cm diameter, with a heating wire and a thermocouple sensor in contact directly with the chemicals (see Fig. 2.11).

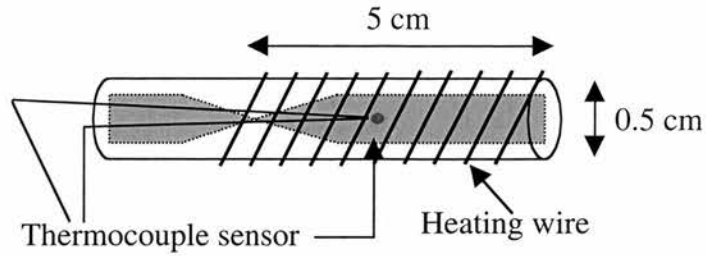


Fig. 2.11 Scheme of the doser, including the thermocouple sensor and heating wire.

2.11 Experimental details

The experiments were carried out in two UHV systems. The first system involved vibrational studies, through HREELS technique, and photoluminescence analysis. Here, it was used an analysis chamber (base pressure $<10^{-10}$ mbar) fitted with HREEL spectrometer and a preparation chamber (base pressure $<3 \times 10^{-10}$ mbar), with dosing facilities, in which the PL measurements were performed. The HREEL spectra were mainly taken at room temperature with a primary electron energy of 8 eV in specular scattering geometry ($\Theta_i = \Theta_s = 45^\circ$).

The second system consisted of topographic studies in an UHV system (base pressure $<10^{-10}$ mbar) equipped with STM (Omicron), LEED and reflectance absorption infrared spectroscopy (Nicolet). Tungsten tips were used which were prepared by an electrochemical etching technique. Mass spectroscopy confirmed the absence of significant contaminants during the dosing at room temperature.

Silicon samples were cut from single side polished wafers (P-doped, 8 12 Ωcm) and mounted on a sample carrier with Ta clips. For temperature calibration, a thermocouple was attached to the front side of the sample with ceramic glue after

completion of the PL and HREELS experiments. In the PL measurements, which were carried out at room temperature, the sample was illuminated by the monochromated pulsed light of by a N₂ laser (3.7 eV, $\Delta t = 4$ ns, $W = 2$ mJ cm⁻²) at an incidence angle of 30° to the surface plane. The luminescence was collimated by a quartz lens positioned 5 cm perpendicular from the sample inside UHV. A charge accumulating InGaAs diode was used to measure the time integrated PL signal (total yield) and a silicon avalanche photodiode was employed to record the PL transients. PL experiments in chapter 3 and 4 were carried out in close collaboration with Dr. Thomas Dittrich from Physics Dept. of Technische Universität München.

Conditions about chemicals used during the experiments are detailed as follow. Prior to dosing, maleic anhydride (Aldrich, 99%) was purified by repeated sublimation and pumping cycles. Larger molecules such as perylene, tetracene and PTCDA were deposited from a doser, described in the previous section. These chemicals were degassed for at least 12 hours at minimum temperature of 343 K (and over in the case of PTCDA).

References

- 1 G. Binnig, H. Rohrer. *Helv. Phys. Acta.* **55**, 726. (1982).
- 2 R. Hammers, *J. Ann. Rev. Phys. Chem.* **40**, 531 (1989a).
- 3 R. M. Tromp, *J. Phys.: Condens. Matter* **1**, 10211 (1989).
- 4 R. M Feenstra, *Scanning Tunnelling Microscopy and Related Methods*, NATO ASI Series E: Appl. Sci. Vol 184, p. 211 (1990).
- 5 G. Binnig, H. Rohrer, *Surf. Sci.* **126**, 236 (1983).
- 6 N. D Lang, *Phys. Rev. Lett.* **58**. 45 (1987a).

-
- 7 www.tmmicro.com/spmguide/1-1-0-.htm
 - 8 R. Wiesendanger, *Scanning Probe Microscopy and Spectroscopy*. (Cambridge U. Press,1994).
 - 9 G. Binnig, N.Garcia, H. Rohrer, Phys. Rev.B **32**. 1336 (1985a,b).
 - 10 R. J. Hamers, Ann. Rev. Phys. Chem.40, 531 (1989).
 - 11 R. M. Feenstra, W. A. Thompson, A. P.Fein, Phys. Rev. Lett. **56**, 608 (1986).
 - 12 R. M. Feenstra, J. M. Stroscio, A. P Fein, Surf. Sci. **181**. 295 (1987a).
 - 13 H. Neddermeyer, S. Tosch, Ultramicroscopy **25**, 135 (1988).
 - 14 J. C. Riviere, *Surface Analytical Techniques* (Oxford Science Public. 1990).
 - 15 H. Luth, *Surfaces and Interfaces of Solids*. Springer–Verlag, Heidelberg 1993.
 - 16 J. Vickerman. *Surface Analysis*. Ed John Wiley, 1997.
 - 17 H. Ibach, D. L. Mills, *Electron Energy Loss Spectroscopy and Surface Vibrations* (Academic, New York 1982).
 - 18 V.Y.Timoshenko, J. Rappich, Th. Dittrich, Appl.Surf.Sci. **123/124**, 111 (1998).
 - 19 C. A. Parker, *Photoluminescence of Solutions*, Elsevier, Amsterdam (1968).
 - 20 H.F. Ivey, IEEE J. Quantum Electron.,QE-2, 713, (1966)
 - 21 S. M. Sze, *Physics of Semiconductor Devices*, 2nd Edition, John Wiley & Sons, New York (1981).
 - 22 A.A. Bergh and P.J. Dean, *Light-emitting diodes*, Clarendon, Oxford (1976).
 - 23 J. Simons, J. Phys. Chem. **95**, 1017 (1991).
 - 24 Gaussian 98, Revision A.7, M. J. Frisch, G. W. Trucks, H. B. Schlegel, G. E. Scuseria, M. A. Robb, J. R. Cheeseman, V. G. Zakrzewski, J. A. Montgomery, Jr., R. E. Stratmann, J. C. Burant, S. Dapprich, J. M. Millam, A. D. Daniels, K. N. Kudin, M. C. Strain, O. Farkas, J. Tomasi, V. Barone, M. Cossi, R. Cammi, B. Mennucci, C. Pomelli,

C. Adamo, S. Clifford, J. Ochterski, G. A. Petersson, P. Y. Ayala, Q. Cui, K. Morokuma, D. K. Malick, A. D. Rabuck, K. Raghavachari, J. B. Foresman, J. Cioslowski, J. V. Ortiz, A. G. Baboul, B. B. Stefanov, G. Liu, A. Liashenko, P. Piskorz, I. Komaromi, R. Gomperts, R. L. Martin, D. J. Fox, T. Keith, M. A. Al-Laham, C. Y. Peng, A. Nanayakkara, C. Gonzalez, M. Challacombe, P. M. W. Gill, B. Johnson, W. Chen, M. W. Wong, J. L. Andres, C. Gonzalez, M. Head-Gordon, E. S. Replogle, and J. A. Pople, Gaussian, Inc., Pittsburgh PA, 1998.

25 Gamess Version, 25 Mar 2000 From Iowa State, M.W.Schmidt, K. K. Baldrige, J. A. Boatz, S. T. Elbert, M. S. Gordon, J. H. Jensen, S.Koseki, N.Matsunaga, K. A. Nguyen, S. J. Su, T. L. Windus, Together With M.Dupuis, J.A.Montgomery, J. Comput. Chem. **14**, 1347-1363 (1993).

26 F. Jensen, *Introduction to Computational Chemistry*, John Wiley & Sons, Chichester (1999).

27 A. D. Becke, Phys. Rev. A **38**, 3098 (1988).

28 T. Bitzer, T. Alkunshile, N.V. Richardson. Surf. Sci. **368**, 202 (1996).

29 Chabal, Y. J. Physica B. **170**, 447 (1991).

30 Grundner, M. and H. Jacob, Appl. Phys. A **39**,73 (1986).

31 G.S. Higashi, Y. J. Chabal, G.W. Trucks, and K. Raghavachari. Appl. Phys. Lett. **56**(7), 656. (1990).

32 C. Stuhlmann, Thesis, Jülich (Germany)

CHAPTER 3

Gap State Formation During the Initial Oxidation of Si(100)-2x1 and Si(111)

3.1 Introduction

The interaction of oxygen with silicon surfaces has been studied in great detail [1-6]. Oxidised silicon surfaces can be produced by wet oxidation in a chemical etching environment, or by exposure of the clean silicon surface, held at elevated temperature, to oxygen or water under vacuum. Silicon oxide films produced by chemical etching are widely used to protect silicon surfaces from contamination while they are handled in the atmosphere. Later, the oxide film can easily be removed by annealing at high temperature 1175 K. Furthermore, SiO₂ films are important as insulator films and as protective coatings against etching in electronic device technology.

Interaction of clean silicon surfaces with oxygen gas can lead to production either of a silicon oxide film on the surface (passive oxidation) or to etching of the surface (active oxidation) in which silicon atoms are removed, depending on the surface temperature and oxygen pressure. The general trend is that active oxidation dominates at high temperatures, while passive oxidation dominates at high oxygen pressures [7].

Silicon is an indirect band gap semiconductor but non-radiative recombination at surfaces plays an important role in many devices such as MOSFETs or solar cells (SC) [8]. The relevant concentrations of electronically active surface defects range between 10¹⁰ and 10¹² cm⁻², which is similar to the concentration of free carriers in a MOS channel. In comparison with the number of chemical bonds at the silicon surface, which

is about $5 \times 10^{14} \text{ cm}^{-2}$, the concentration of electronically active surface defects is rather small.

Recombination of electron holes pair at surfaces is caused by the presence of electronic surface states in the forbidden band gap, which can act as traps or as recombination active centres. Surface states at reconstructed Si surface have been investigated with scanning tunneling spectroscopy (STS)[9,10], photovoltage spectroscopy (SPS) [11] and scanning tunneling photovoltage [12,13]. STS studies have shown that surface states, which are related to dangling bonds, vanish after saturating the dangling bonds at the reconstructed Si surface with hydrogen atoms [10]. Chemisorbed molecules, e.g. oxygen [13], also introduce surface states. However, it is still unknown, whether surface states are recombination active or not.

Several angle resolved photoemission studies on Si(100)- 2×1 have pointed to the presence of a surface state close to the Fermi level, which has been associated with domains of asymmetric dimers arranged into $c(4 \times 2)$ or $p(2 \times 2)$ periodicity [14,15]. At room temperature, localized domains of ordered asymmetric dimers on clean Si(100)- 2×1 are frequently found around point defects in scanning tunneling microscopy [16], see Fig. 1.10.

Photoluminescence has been used to follow the gap state formation during initial oxidation of silicon surfaces exposed to oxygen in vacuum. In order to monitor the oxidation process, molecular oxygen and water adsorption followed by heating have been considered. Before presenting the results, previous studies of O-Si interactions are reviewed followed by vibrational studies using EELS. Later, I present information on the formation and changes in the gap states. Finally, relevant results concerning the gap state on Si(111) surface will be presented.

3.2 Review of oxygen on silicon surfaces

As mentioned above, the initial oxidation of silicon surfaces and the structure and composition of SiO_2 in the proximity of the crystalline silicon have been studied widely [1-6]. However, little is known about the origin of gap states at the Si/SiO_2 interface. Avouris and Lyo [17], from STM studies, concluded that the initial adsorption occurred predominantly at defect sites. From calculations, O_2 is predicted to adsorb dissociatively [18,19]. Many other kinds of surface analyses have been used to study oxygen adsorption kinetics onto silicon surface [20-25].

Watanabe et al [26], in their SREM studies, followed the kinetics of initial layer-by-layer oxidation of the $\text{Si}(100)\text{-}2\times 1$ surface. They depicted this process with increasing oxidation as shown in Fig. 3.1. After cleaning the surface, Fig. 3.1a, oxidation of the dangling bonds and the first subsurface layer is obtained (Fig. 3.1b). Further oxidation leads to oxidation of the second and third subsurface layers, Figs. 3.1c, d.

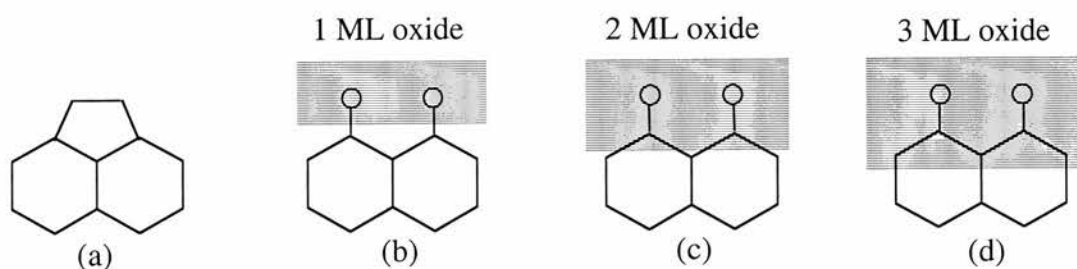


Fig. 3.1 Depiction of $\text{Si}(100)$ surfaces before and after oxidation. (a) Initial clean $\text{Si}(100)$ surface. (b) After 3 min of oxidation at room temperature. (c) After 17 min of oxidation at $635\text{ }^\circ\text{C}$ following 15 min of oxidation at room temperature and (d) a further 65 min of oxidation at $700\text{ }^\circ\text{C}$. The shadow areas represent the subsurface layers involve in the oxidation process.

SREM images were recorded at each oxidation step after oxygen evacuation, and the periodic reversal of SREM contrast observed implies layer-by-layer oxidation of the Si(100)-2x1 surface. In particular, for first and second layer oxidation, it has been found that oxygen chemisorbs onto the uppermost layer situated in the top and bridge sites (see Fig. 3.2), cases 1 and 2 respectively.

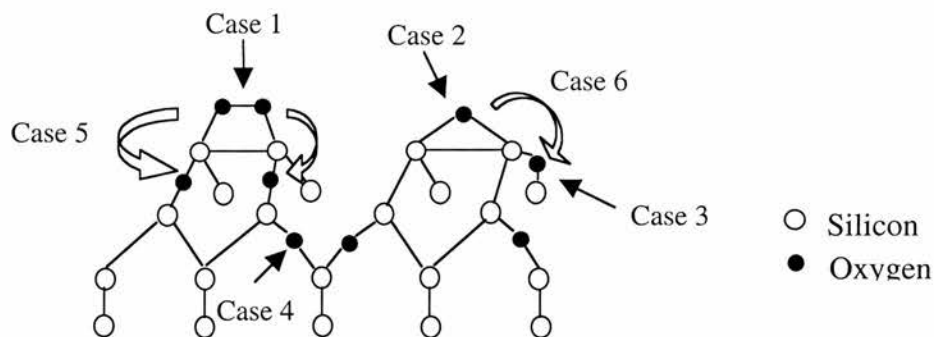


Fig. 3.2 Schematic illustration of the initial oxidation and oxygen sites in the different subsurface layers.

Case 3 shows oxygen atom insertion into the first subsurface. Note that after oxidation at room temperature for 3 min, oxygen atom insertion into the back bond, as well as oxygen adsorption onto the uppermost layer (Fig. 3.1b), occur even at low temperatures. Case 4, oxygen atom insertion into the second subsurface, requires a much higher temperature. Finally, cases 5 and 6 show oxygen atom migration from the uppermost layer to the back bond.

3.3 Review of water adsorption and oxidation on silicon surface

The main focus in this stage is to review the thermal evolution of water-exposed Si(100) studies, as well as part of the wider oxidation process. The H₂O:Si(100) system

has received considerable attention [7, 27, 28], and some of these studies have focused on the nature of the adsorption. Now, it is clearly established to be predominantly dissociative, forming Si-H and Si-OH [26].

Studies by Weldon et al [1] are related to direct observation of the vibrations of all species relevant to this system, including SiO, SiH, and SiOH. They showed that the homogeneous H₂O-exposed surface (comprising one H and one OH per dimer, see Fig. 3.3a) evolves into a mixed phase consisting of oxygen free, and singly, and doubly oxidized dimer units. They also identified two distinct intermediate Si-O species at 675 K that demonstrate that oxidation starts with the insertion of an oxygen into the surface dimer bond, as show in Fig. 3.3b, which facilitates subsequent incorporation of oxygen into the silicon backbonds. The important results are summarized in table 3.1, showing both calculated and experimental frequencies [1].

TABLE 3.1. A summary of theoretical and experimental frequencies (cm^{-1}) of the structures shown in Fig. 3.2 Taken from Weldon et al [1].

Mode	Structure	Theory [29]	Experiment
ν_a (Si-O)	HSi-O-SiH	993	993
ν''_a (Si-O)	HSi-O-Si(O)H	1013	1013
ν'_a (Si-O)	HSi-O-Si(O)H	1046	1042
ν_s (Si-H)	HSi-SiOH	2084	2084
ν_a (Si-H)	HSi-SiH	2091	2090
ν_s (Si-H)	HSi-SiH	2098	2099
ν_a (OSi-H)	HSi-O-SiH	2110	2109
ν_s (OSi-H)	HSi-O-SiH	2113	2117
ν (OSi-H)	HSi-O-Si(O)H	2110	2109
ν (O ₂ Si-H)	HSi-O-Si(O)H	2158	2165

These observations at low temperature (~ 300 K) are consistent with the known initial surface structure [28,30,31] with H and OH passivating the dangling bonds of the same dimer, HSi-SiOH, Fig. 3.3a. However, substantial changes occur in the 575 to 675 K temperature range. After the 675 K anneal partial information about the surface composition can be deduced from the frequencies and polarizations of the SiH stretching modes. This provides evidence for the segregation of oxygen-free dimers and the presence of a O_x Si-H mode which signal insertion of oxygen into the Si backbonds.

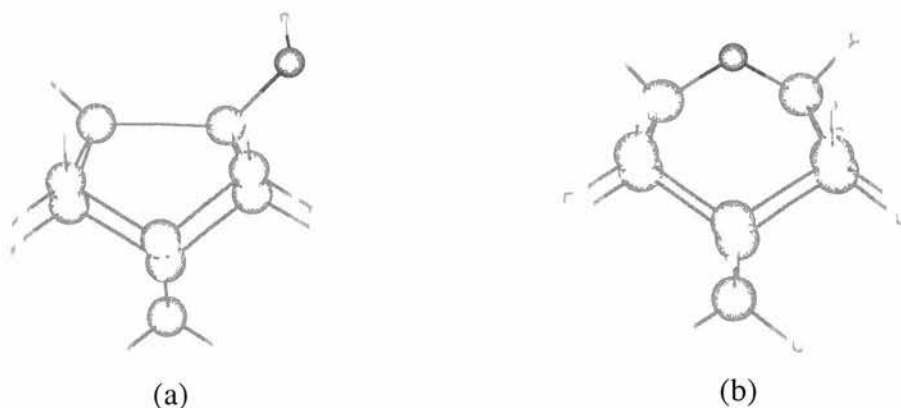


Fig. 3.3 Structure of the dissociative process of water adsorption on silicon surface. (a) Passivation of the silicon dimer through Si-H and Si-OH bonds. (b) Insertion of oxygen into the surface dimer after heating the sample at 675 K. Smallest circles represent hydrogen atoms, the medium size are oxygen and the biggest ones are silicon.

3.4 HREELS study of oxygen adsorption on Si(100)-2x1

The HREELS spectra of Si(100)-2x1 (Fig. 3.4) were obtained after an O_2 dosage of 3.5 L, 20 L, and 1.4 kL: they display the characteristic behaviour of a dry oxide film.

Details of those spectra are as follows. Firstly in Fig. 3.4(a), after an oxygen dosage of 3.5 L, a shoulder at 490 cm^{-1} and two distinctive peaks at 695 and 990 cm^{-1} are present in the vibrational data which can be rather straightforwardly assigned to the Si–O deformation, symmetric, and asymmetric in-plane stretching vibrations, labelled as $\nu_s(\text{Si-O-Si})$ and $\nu_a(\text{Si-O-Si})$, respectively [32]. By comparison with an early HREELS study, as calibrated by J. A. Schaefer et al. [32] on the basis of the peak positions and frequency shift of this feature compared to the quantitative XPS measurements, for room temperature adsorption, it is estimated the oxide coverage near 0.4 monolayer (ML). At 20 L oxygen exposure, Fig. 3.4b, the symmetric and asymmetric Si-O peaks remain distinct although a slight shift towards higher frequencies occurs with increase in oxygen coverage.

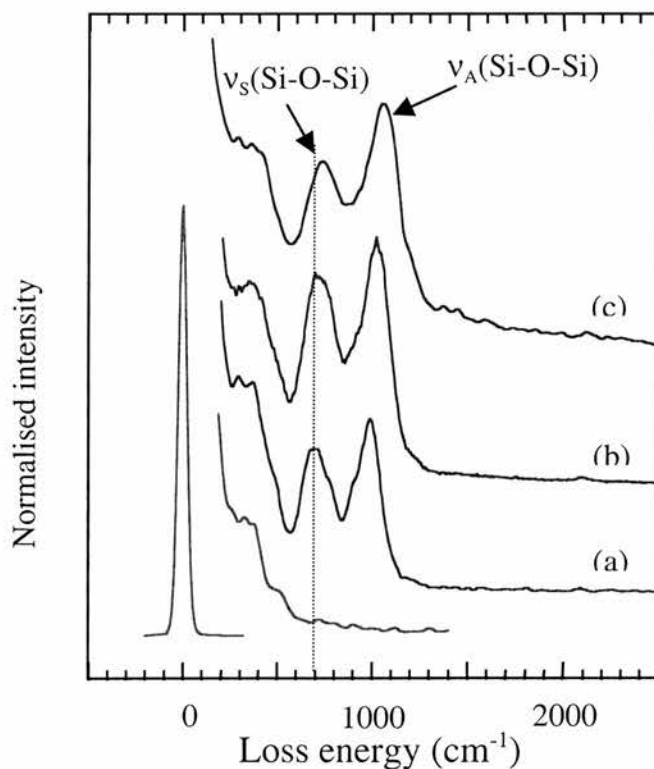


Fig. 3.4 Vibrational spectra of Si(100) after oxygen dosage of (a) 3.5 L, (b) 20 L, and (c) 1.4 kL. The last corresponds to 0.6 monolayer coverage or higher. A

frequency shift is noticeable in the symmetric and asymmetric Si-O-Si stretching modes.

A major shift towards higher frequencies takes place at 1.4 kL oxygen exposure (Fig. 3.4c). There, the most intense peak can be observed at 1050 cm^{-1} , which is indicative of an oxide coverage above 0.6 ML. Higher oxides are ruled out since they possess distinct SiO bands around 1100 cm^{-1} [32]. The observation of a submonolayer oxide coverage, even at relatively high O_2 exposure, is consistent with the layer-by-layer oxidation of Si(100)-2x1 suggested by Watanabe et al. [26]. Thus, molecular O_2 chemisorbs dissociatively on Si(100)-2x1 by the formation of epoxide structures, Fig 3.5. Following prolonged exposure of Si(100)-2x1 to O_2 at room temperature, oxygen was found to be incorporated only into the first silicon layer, i.e., into the Si-Si bonds of dimer complexes.

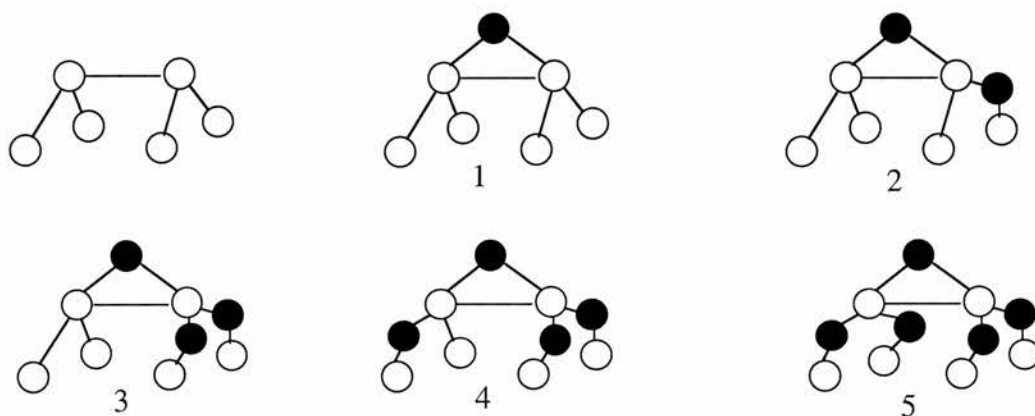


Fig. 3.5 Epoxides on Si(100)-2x1. Filled circles represent oxygen atoms and Silicon atoms are empty circles. Dimer structure with 1, 3 and 5 oxygen atoms are thermodynamically favoured [2].

3.5 HREELS study of water on Si(100)-2x1

A study of water adsorption on Si(100)-2x1, starting with 0.5 L H₂O on a previously oxide free Si(100)-2x1 surface, is shown in Fig. 3.6. The clean surface was achieved after oxide removal by heating the sample to 1175 K. It is important to point out the formation of Si-H and Si-OH species in agreement to the dissociative behaviour of water molecule on Si(100), as described above and shown in Fig. 3.3a, with corresponding vibrational peaks at 810 cm⁻¹ for stretching Si-OH and both 635 and 2020 cm⁻¹ for Si-H bending and stretching modes, respectively.

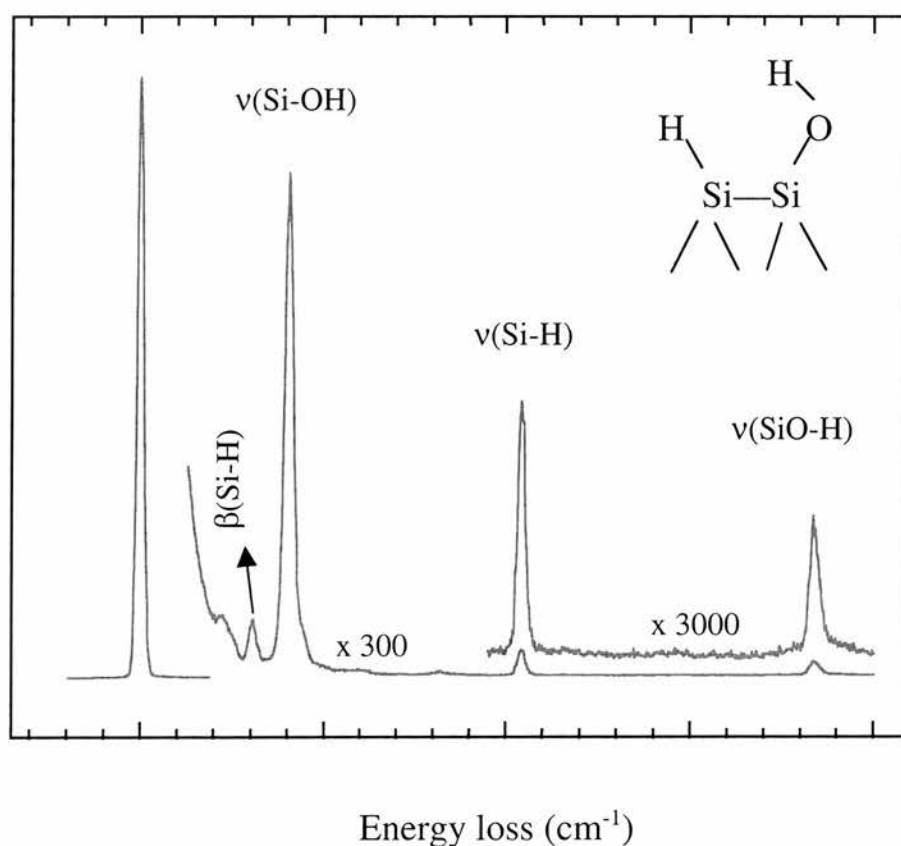


Fig. 3.6 Vibrational spectrum of 0.5 L water adsorption on Si(100).

Figure 3.7 shows the HREEL spectra of (a) the surface heated at 805 K after 0.5 L water dosing, involving desorption of H and formation of epoxides, and (b)

subsequent water adsorption. In the dehydrogenated oxide film spectrum (Fig. 3.7a), 0.25 ML thick before post-treatment with water, Si–O vibrational modes are present at 350, 460, and 1045 cm^{-1} [22]. The assignment of the mode at 665 cm^{-1} to the Si–H bending mode of an oxidized Si dimer atom is supported by the observation of the $(\text{O})_3\text{Si-H}$ stretch at 2285 cm^{-1} , which indicates an incomplete dehydrogenation of the oxide structures.

The modes at 810, 2085, and 3665 cm^{-1} in the HREEL spectrum of the H_2O exposed surface at room temperature (Fig. 3.7b), which can be assigned to $\nu(\text{Si-OH})$, $\nu(\text{Si-H})$, and $\nu(\text{SiO-H})$ respectively, are the same as for chemisorption of H_2O on an oxide-free Si(100)- 2×1 surface. In addition, the 1045 cm^{-1} peak, which correspond to Si-O-Si vibration mode, is a feature of back bond oxygen or second oxygen subsurface described as cases 5 and 6 in Fig. 3.2. This peak is the main difference between spectrum showed in Fig. 3.6 and the curve in Fig. 3.7b, as result of annealing at high temperature (around 1100 K).

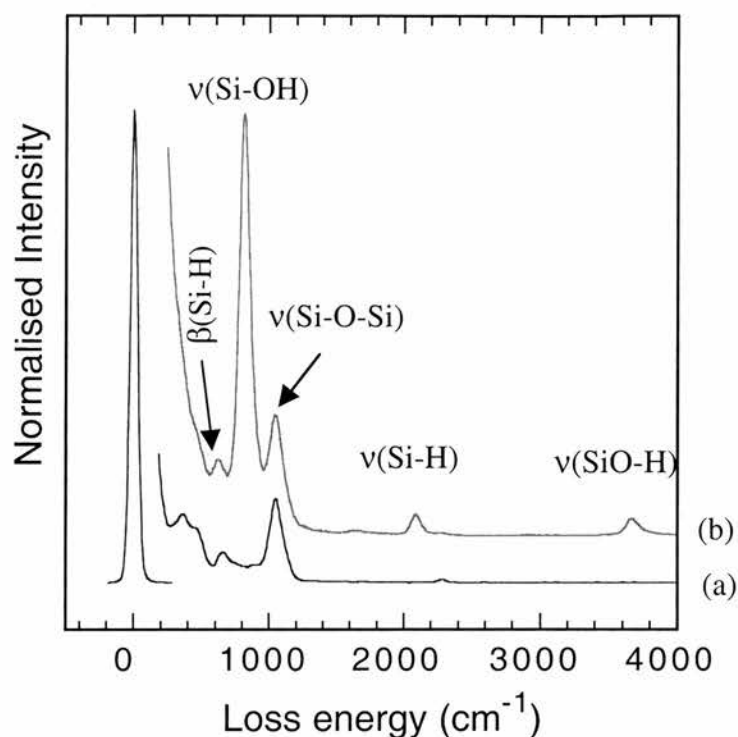


Fig. 3.7 HREEL spectra of (a) dehydrogenated oxide film before post-treatment with H₂O, and (b) after water adsorption treatment.

Those bonds, related with water and oxygen adsorption have a strong influence in the density of states on the surface and details of this will be presented in the next sections.

3.6 Gap state formation during initial oxidation of Si(100)-2x1

PL experiments were carried out at University of St. Andrews in collaboration with Dr. Thomas Dittrich from Technische Universität München. The results obtained from these studies are presented in this chapter and in chapter 4.

Although the adsorption of some organic molecules on silicon surfaces have been studied in great detail, as mentioned in section 3.1, little is known about the

electronic properties at the organic film/semiconductor interface. In particular, electronic states in the fundamental gap are of major importance if a current is to be passed across the organic film/semiconductor interface. Recently, it has been shown that the measurement of the photoluminescence (PL) induced by the pulsed light of a nitrogen laser can be used to determine quantitatively the density of gap states at silicon surfaces [33]. A detailed description of these measurements is given in section 1.5. Therefore, excitation of the sample with light makes the PL technique particularly favourable for the study of the gap state density of organic film/semiconductor interfaces under ultra high vacuum (UHV) conditions.

Figure 3.8 shows the density of gap states D_{it} for sequential exposures of Si(100)-2x1 to O_2 at room temperature. Note that for the estimation of D_{it} , a constant recombination cross section was assumed, according to Eq.(4) written in section 1.5. For the clean Si(100)-2x1 surface we estimate D_{it} to be $1 \times 10^{12} \text{ eV}^{-1} \text{ cm}^{-2}$, depicted as empty circle. As can be seen in Fig. 3.8, the initial dosage of 0.002 L of molecular oxygen ($1 \text{ L} = 10^{-6} \text{ Torr s}$) already induces an increase of D_{it} by 15%, i.e., gap states are formed in the earliest stages of silicon oxidation [34]. The last part in this sequence, corresponding to triangles, represents the exposure of the Si(100)-2x1 to 1.8 kL O_2 , where D_{it} increases to $2.7 \times 10^{12} \text{ eV}^{-1} \text{ cm}^{-2}$. The surface recombination velocity, S_o , increases systematically with increasing the dosage of O_2 , from $1.0 \times 10^4 \text{ cm/s}$ until $2.7 \times 10^4 \text{ cm/s}$ (Eq. 4 in section 1.5) [35].

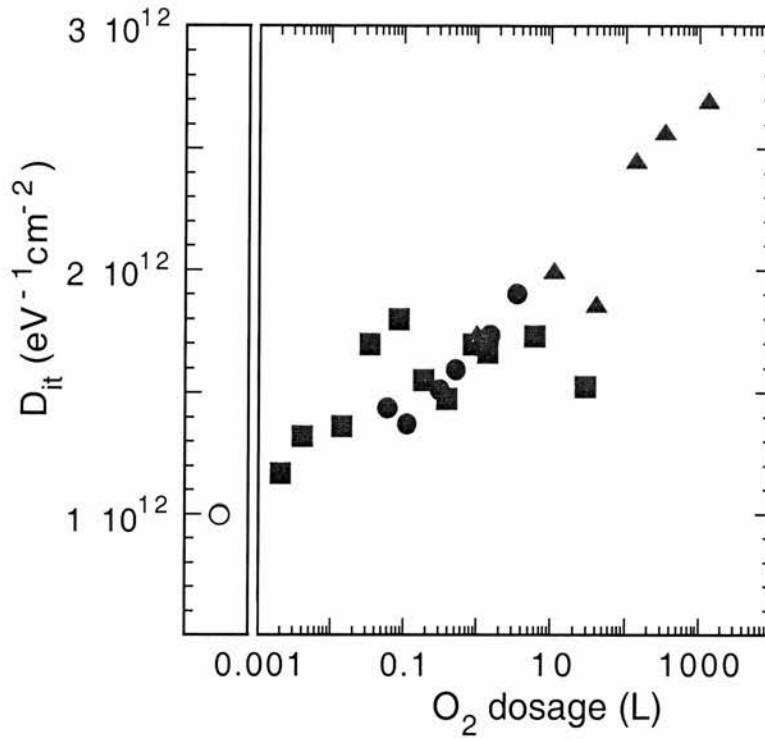


Fig. 3.8 A steady increment in the density of the gap states D_{it} during sequential exposures of Si(100)-2x1 to oxygen. Filled circles, squares, and triangles indicate three independent series of sequential oxygen exposures respectively. The empty circle indicates the gap state density of a clean Si(100)-2x1 surface.

As mentioned before, from angle resolved photoemission studies in section 3.1, here the residual gap state density of clean Si(100)-2x1 are related to a surface state of localized ordered asymmetric dimers structures, which are pinned by point defects. However, contributions from contaminants cannot be ruled out.

Recently, extended Hückel-type, non-orthogonal, tight-binding calculations by Nishida indicated the presence of gap states at an ultrathin oxide layer in which oxygen

is adsorbed in a top-bridge site on Si(100)-2x1 [36]. Although experimental confirmation for this site occupancy has not yet been obtained, we tentatively relate the observed gap state formation at low oxygen exposure to top-bridge bonded oxygen as proposed by Nishida.

3.7 Photoluminescence study of water on Si(100)-2x1

In order to verify the assignment of gap states to top-bridge bonded oxygen, we formed an ultrathin oxide film by heating saturated H₂O/Si(100)-2x1 to 805 K for 1 min. The chemisorption of H₂O on clean Si(100)-2x1 (empty circle in Fig. 3.9) leads to a slight decrease of the gap state density (filled circle in Fig. 3.8). However, after heating to a temperature of 805 K, D_{it} has risen to $2.0 \times 10^{12} \text{ eV}^{-1} \text{ cm}^{-2}$ (filled square). Subsequent prolonged exposures to H₂O at room temperature reduce the gap state density at the surface, as can be seen by filled squares in Fig. 3.8. Note that a dosage of 0.1 L H₂O already results in a significant drop of D_{it} . [34]. The surface recombination velocity, S_0 , remains (almost) constant after dosing of 0.5 (or more) L H₂O, but increased by more than 2 times after heating to 805 K. An increase of S_0 by such a great amount can be explained only by the generation of non-radiative surface defects [35].

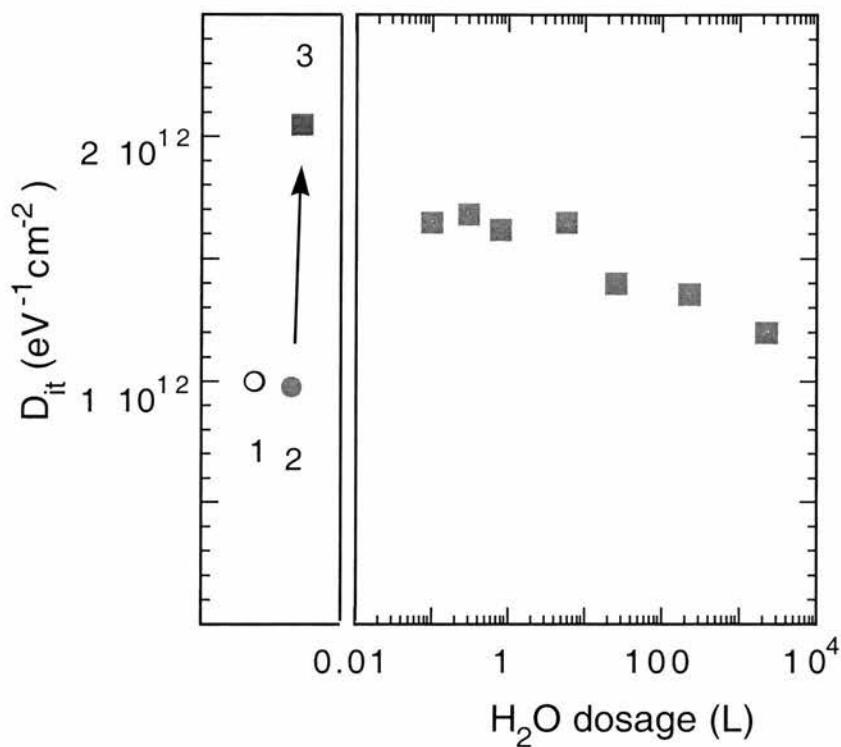


Fig. 3.9 Density of gap states during water adsorption. In the left, empty circle corresponds to clean Si(100)-2x1. Filled circle corresponds to chemisorption of H_2O and the filled square is the D_{it} after heating the sample at 850 K. In the right, the effect of a prolonged exposure of H_2O at room temperature are shown.

The HREELS data show that we have to consider three chemisorption sites for H_2O , which are oxide-free Si dimers (Fig. 3.6), partially dehydrogenated dimer structures with oxygen incorporated (Fig. 3.7b), and completely dehydrogenated oxidized silicon structures (Fig. 3.7a). As discussed above, H_2O chemisorbs on Si(100)-2x1, but the saturation of Si(100)-2x1 with Si-H and Si-OH groups does not create gap states at the silicon surface Fig. 3.9). Second, an adsorption of H_2O on partially

dehydrogenated structures would require the insertion of the hydrogen atom or the OH group into Si–O–Si linkages and Si–Si bonds, respectively, due to the absence of a pair of dangling Si bonds. Such an insertion is not observed even after extended H₂O exposures [2]. It should be also noted that hydrogenated oxide structures are not expected to contribute to the observed gap state density [36].

Finally, we consider the adsorption of H₂O on completely dehydrogenated oxidized silicon structures. In the case of top-bridge bonded oxygen on Si(100)-2x1, the chemisorption of H₂O would involve a structural rearrangement of the topmost oxygen atom. Such a rearrangement leads to a silicon cluster, in which electronic states in the fundamental gap are expected to be absent [36]. In this light, the observed reduction of D_{it} can be related to the H₂O induced formation of Si–O–Si surface species with Si–H and Si–OH groups attached, See Fig. 3.10. Consequently, a complete quenching of gap states would require a prolonged exposure to H₂O, which is indeed observed [Fig. 3.9].

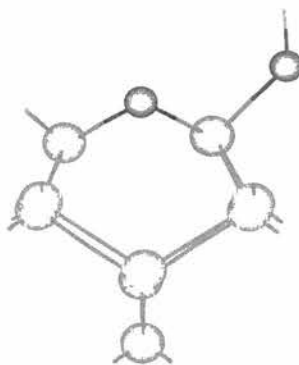


Fig. 3.10. A model of Si–O–Si surface species with H and OH groups attached.

Thicker SiO₂ films can be grown by repeated exposure of Si(100)-2x1 to 1 L H₂O at room temperature and heating to 805 K, as represented in Fig. 3.10. After a total dosage of 9 L H₂O, the characteristic vibrational modes of a dehydrogenated oxide film are observed at 465, 810, and 1175 cm⁻¹ in the HREEL spectrum (Fig. 3.10). From a comparison of the HREEL spectrum with the results of Schaefer and Göpel [32], it estimates the thickness of the oxide film to be above 1.5 ML. Interestingly, the post-treatment of the dehydrogenated oxide film with H₂O leaves the HREEL spectrum virtually unchanged.

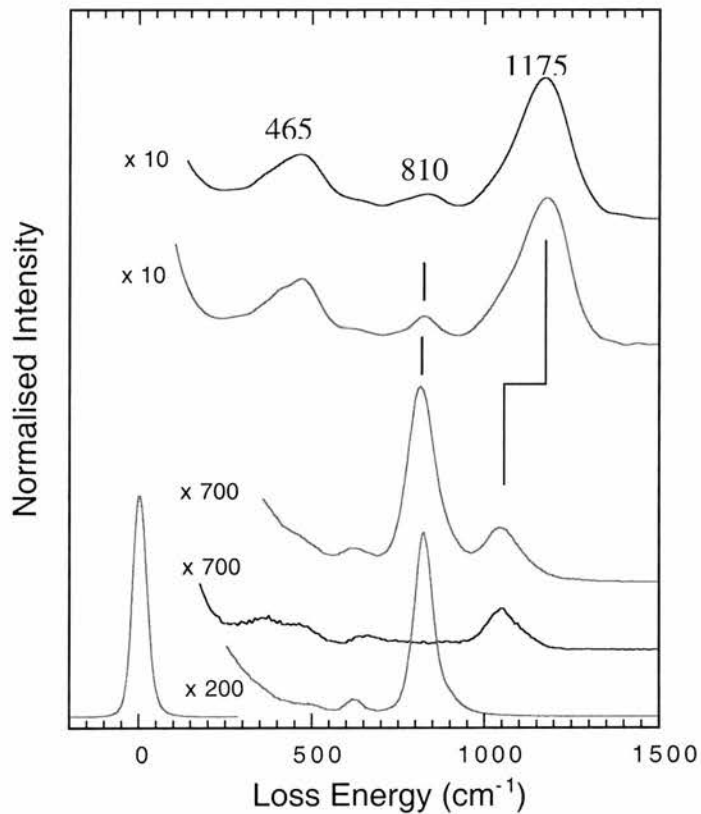


Fig. 3.11 This spectra show the sequence of several cycles of 1 L water dosing and heating at 805 K .The three lower HREEL spectra present the cycle of thick oxide films on S(100)-2x1 (lowest) achieved by repeated water exposures and heating at 805 K for 1 min (second from the bottom). The two upper spectra were taken after 9L H₂O and heated to 805 K (the topmost spectrum).

As observed above, the thermally induced dehydrogenation of oxidized Si(100) results in a formation of gap states, which can be significantly quenched by a post-exposure of the silicon substrate to H₂O (Fig. 3.11). This diagram shows the density of gap states of Si(100)-2x1 during the repeated exposure from 1L to 9L H₂O at room temperature (filled circles) and after heating to 805 K for 60 s (filled squares). The PL measurements show also that, after the initial oxidation, D_{it} falls steadily with the growing total H₂O exposure even below the value of the clean Si(100)-2x1 surface. It is tentatively assigned the improvement of D_{it} to the completion of the first SiO₂ monolayer on Si(100)-2x1, which prevents the presence of top-bridge, bonded oxygen, as deduced through the vibrational spectra in Fig. 3.10. Note that at larger oxide film thickness, the thermally induced dehydrogenations of the oxide film and post-exposure to H₂O, respectively, induce only a relatively small change of D_{it} .

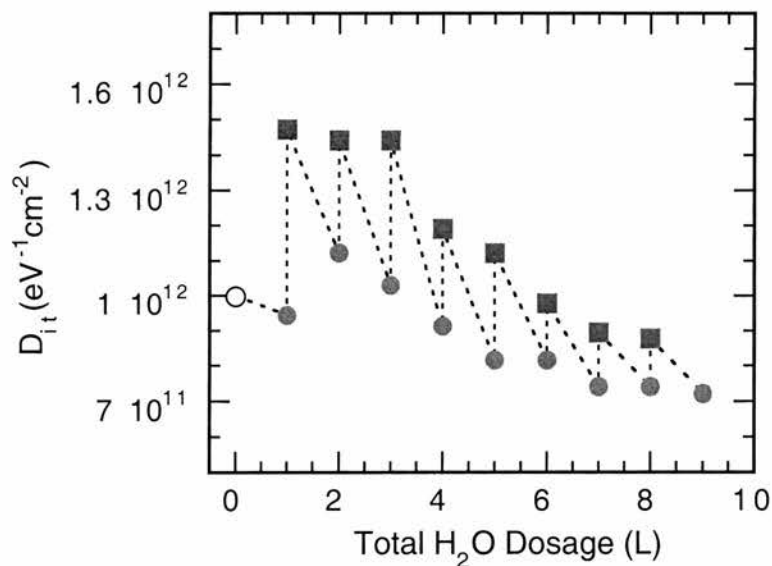


Fig. 3.12 Development of the gap state density during the cyclic wet oxidation of Si(100). After heating the silicon crystal to 805 K, D_{it} increases significantly

due to almost complete dehydrogenation of this surface. Further exposure with H₂O reduces the gap state density. Filled circles represent D_{it} after water exposure and filled squares represent D_{it} after heating.

3.8 Gap state changes on Si(111) surface.

Here, the changes observed on Si(111) surface at three different stages are presented. Firstly, a hydrogen-terminated Si(111)-1x1 surface was prepared through etching procedure (see details in section 2.9). The HREEL spectra in Fig. 3.13a shows the distinctive peaks for this passivated surface, where the vibrational stretching mode Si-H at 2060 cm⁻¹ [37] and the bending mode Si-H at 640 cm⁻¹ are presented. The quality of this surface was verified by LEED, as can be seen in Fig. 3.14a. Photoluminescence measurements at this stage showed the gap state density to be 7x10¹⁰ eV⁻¹ cm⁻².

After heating the sample at 825 K, the spectrum (Fig. 3.13b) shows that the H-Si distinctive peaks have almost disappeared, indicative of hydrogen desorption and a clean Si(111) surface, although still with a 1x1 reconstruction, as shown in Fig. 3.14 (b) by the LEED pattern recorded at 65 eV. The gap state density obtained was 5x10¹² eV⁻¹ cm⁻², which shows a sharp increase due to increment in the surface recombination velocity to 5x10⁴ cm/s [35].

Heating the clean Si(111) surface at 1175 K lead to a 7x7 reconstruction surface as shown in Fig. 3.14c, from the LEED pattern obtained. The featureless HREEL spectrum reflects the properties of this surface. It is important to notice the slight change in D_{it}, being 8x10¹² eV⁻¹ cm⁻², caused by the reduction in the dangling bond as part of the reconstruction and the fact that the adatoms of the clean surface have a high

density of states near the Fermi energy [38]. Again, an increment in S_0 (8×10^4 cm/s) is obtained after forming the Si(111)-7x7 reconstructed surface [35]. This gives an indication that dangling bonds at the Si(111)-1x1 and Si(111)-7x7 surfaces are not recombination active or much less so than dangling bonds at the Si/SiO₂ interface.

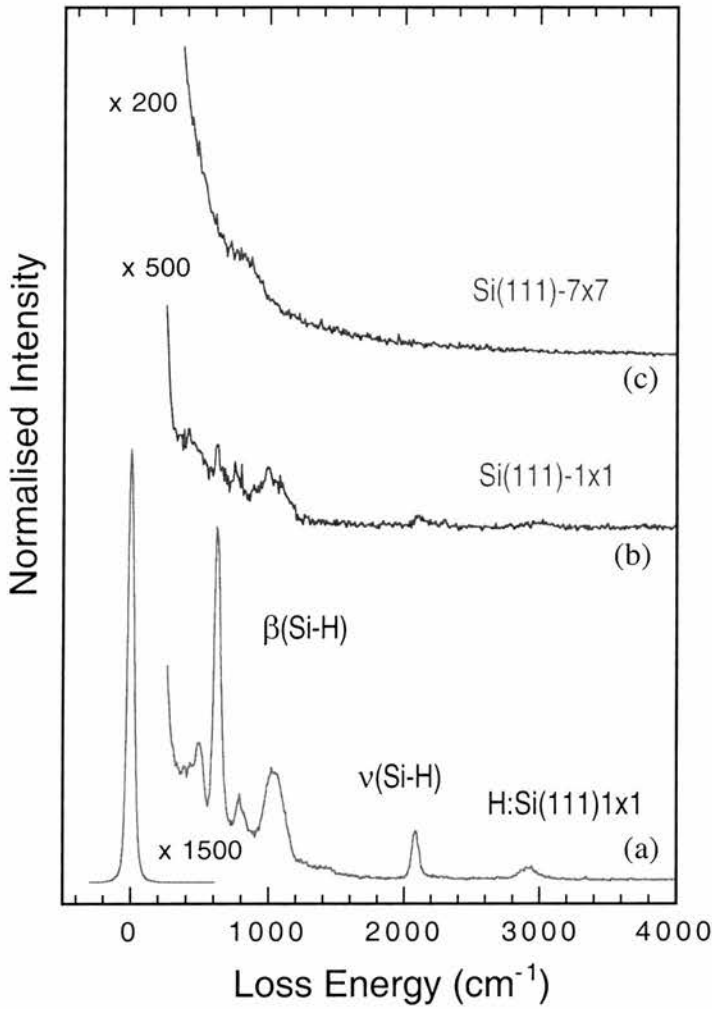


Fig. 3.13 The corresponding HREELS spectrum of (a) hydrogen terminated-Si(111)-1x1. Heating the silicon crystal to 550° C and to 900° C leads first to desorption of the hydrogen and then to the 7x7 silicon surface, spectrum (b) and (c) respectively.

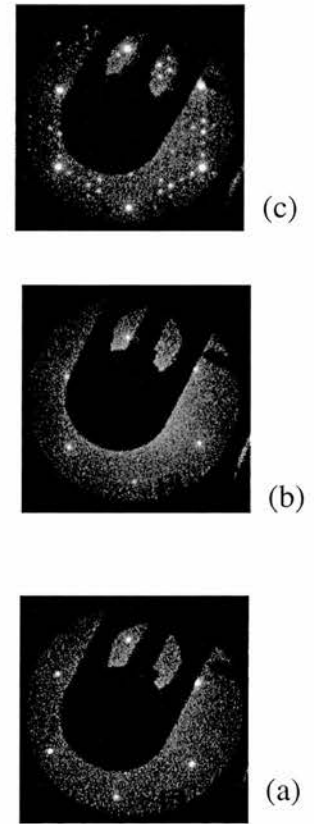


Fig. 3.14 Corresponding LEED pattern for each vibrational spectrum.

3.9 Conclusions

In conclusion, the study provides strong evidence for the formation of gap states during the initial oxidation of Si(100)-2x1 even at exposures of 0.002 L of molecular oxygen. An increase of D_{it} is also observed following the thermally induced dehydrogenation of ultrathin oxide films. Although it is not clear if top-bridge bonded oxygen induces the formation of gap states, the findings stress the importance of post-treatments of thermally formed ultrathin oxide films in order to improve the electronic quality of the Si/SiO₂ interface. Dissociative process of water during adsorption on Si(100)-2x1 was confirmed, including the formation of Si–H and Si–OH species. The density of the gap states is reduced after water adsorption, but a slight increase of D_{it} is observed after annealing the sample at 805 K.

Dehydrogenated Si(111)-1x1 and 7x7 reconstruction surfaces lead to increase in the gap state density and therefore the dangling bonds at these surfaces are not recombination active.

References

1. M. K. Weldon, B. B. Stefanov, K. Raghavachari, Y. J. Chabal, Phys. Rev. Lett. **79**, 2851 (1997).
2. M. K. Weldon, K. T. Queeney, Y. J. Chabal, B. B. Stefanov, K. Raghavachari, J. Vac. Sci. Technol. B **17**, 1795 (1999).
3. B. B. Stefanov, A. B. Gurevich, M. K. Weldon, K. Raghavachari, Y. J. Chabal, Phys. Rev. Lett. **81**, 3908 (1998).

-
4. H.W. Yeom, H. Hamamatsu, T.Ohta, R.I.G. Uhrberg, Phys. Rev. B **59**, 10413 (1999).
 5. P. Avouris, D. Cahill, Ultramicroscopy **42**, 838 (1992)
 6. D. G. Cahill, P. Avouris, Appl. Phys. Lett. **60**, 326 (1992).
 7. H. N. Waltenberg, J.T. Yates, Jr., Chem. Rev. **95**,1589 (1995).
 - 8 S. M. Zse. Semiconductor Devices, Physics and Technology. John Wiley & Son (New York, Chichester, Brisbane, Toronto, Singapore) 1985.
 - 9 P. Avouris, R. Wolkov. Phys. Rev. B **39**, 5091 (1989).
 - 10 J. J. Boland. Phys. Rev B **44**, 1383 (1991).
 - 11 J. Clabes, M. Hensler. Phys. Rev. B **21**, 625 (1980).
 - 12 D. G. Cahill, R. J. Hamers. Phys. Rev. B **44**, 1387 (1991).
 - 13 M. McEllistrem, G. Haase, D. Chen, R. J. Hamers. Phys. Rev. Lett. **70**, 2471 (1993).
 - 14 L. S. O. Johansson, R. I. G. Uhrberg, P. Martensson, and G. V. Hansson, Phys. Rev. B **42**, 1305 (1990).
 - 15 P. Martensson, A. Cricenti, G. V. Hansson, Phys. Rev. B **33**, 8855 (1986).
 - 16 R. M. Tromp, R. J. Hamers, J. E. Demuth, Phys. Rev. Lett. **55**, 1303 (1985).
 - 17 P. Avouris, I-W. Lyo. Appl. Surf. Sci. **60/61**, 426 (1992).
 - 18 X. M. Zheng, P. V. Smith. Surf. Sci. **232**, 6 (1990).
 - 19 Y. Miyamoto, A. Oshiyama. Phys. Rev. B **41**, 12680 (1990).
 - 20 T. Engel, Surf. Sci. Rep. **18**, 91 (1993), and references therein.
 21. M. Tabe, T. T. Chiang, I. Lindau, W. E. Spicer, Phys.Rev. B **34**, 2706 (1986).
 22. F. Lutz, J. L. Bischoff, L. Kubler, D. Bolmont, Phys.Rev. B **40**, 10 356 (1989).
 23. Y. Enta, Y. Takegawa, M. Suemitsu, N. Miyamoto. Appl. Surf. Sci. **100/101**, 449 (1996).

-
24. T. Miyake, S. Soeki, H. Kato, T. Nakamura, A. Namiki, H. Kamba, and T. Suzuki, *Phys. Rev. B* **42**, 11801 (1990).
25. A. A. Shklyaev, T. Suzuki, *Surf. Sci.* **351**, 64 (1996).
- 26 H. Watanabe, K. Kato, T. Uda, K. Fujita, M. Ichikawa, T. Kawamura, K. Terakura, *Phys. Rev. Lett.* **80**, 345 (1998).
- 27 P. A. Thiel, T.E. Madey, *Surf. Sci. Rep.* **7**, 211 (1987).
- 28 L. M. Struck et al., *Surf. Sci.* **380**, 444 (1997).
- 29 B. B. Stefanov, K. Raghavachari. *Surf. Sci.* **389**, 1159 (1997).
- 30 Y.J. Chabal. *Phys. Rev. B* **29**, 3677 (1984).
- 31 K. Raghavachari, Y. J. Chabal, L. M. Struck. *Chem. Phys. Lett.* **52**, 230 (1996).
- 32 J. A. Schaefer, W. Göpel, *Surf. Sci.* **155**, 535 (1985).
- 33 V. Y. Timoshenko, A. B. Petrenko, M. N. Stolyarov, T. Dittrich, W. Fuessel, J. Rappich, *J. Appl. Phys.* **85**, 4171 (1999).
- 34 T. Bitzer, T. Rada, N.V. Richardson, T. Dittrich, F. Koch. *Appl. Phys. Lett.* **77**, 3779 (2000).
- 35 Th. Dittrich, T. Bitzer, T. Rada, V. Y. Timoshenko, J. Rappich. Submitted *Solid-State Electronics*.
- 36 M. Nishida, *Phys. Rev. B* **60**, 8902 (1999).
- 37 G. S. Higashi, Y. J. Chabal, G. Trucks, K. Raghavachari. *Appl. Phys. Lett.* **56**, 656 (1989).
- 38 R.J. Hamers, Y. Wang. *Chem. Rev.* **96**, 1261(1996).

CHAPTER 4

Physical and Chemical Properties of Maleic Anhydride on Si(100)-2x1 Surface

4.1 Introduction

One of the most active fields in organic chemistry today is the search for suitable compounds to control electronic properties on the level of single molecules. To this end, a number of pathways seem possible, from utilizing organic molecules sandwiched between metallic leads, to electrochemical devices, or silicon/organic hybrids [1,2,3]. While transport and electronic properties of single molecules are analyzed extensively in order to determine the most suitable candidate molecules [1], their connection to metallic or semiconductor surfaces is frequently not well understood. On Si(100) surfaces molecular adsorption has been studied for quite some time [3]

Unsaturated molecules, such as ethylene, butene, and cyclohexene have been shown by STM to adsorb via characteristic [2+2] cycloaddition reaction, in which C=C double bond adds to a Si-Si dimer [4-11], also referred to as di- σ interaction. In the process, the carbon bond undergoes a change from sp^2 to sp^3 . The silicon surface can also be functionalized by adsorption of cyclic organic compounds [6,12]. This method is based on the fact that the dimers (formally two silicon atoms sharing a σ and a π bond), which comprise the clean Si(100)-2x1 surface can interact with double bonds in unsaturated organic molecules, thus, attaching the molecule to the surface through the formation of two new σ Si-C bonds. Because the interacting bonds are both strongly oriented, the interaction of the Si=Si dimers with the unsaturated C=C bonds effectively makes the surface Si=Si dimers act as a template for extending orientational order into the organic film [6].

In the present chapter, as continuation of previous work on maleic anhydride/Si(100) interface, a combined geometric, topographic and electronic study of maleic anhydride (MA) on Si(100)-2x1 is used to identify the chemical interaction, and in particular the adsorption sites, between this unsaturated molecule and silicon, and the electronic properties at the interface. The first part is concerned with the chemisorption of MA on Si through vibrational and topographic studies and some discussions with previous studies [4-10]. The STM images clearly demonstrate the bonding sites at the initial stage and also changes on the appearance of the molecules induced by changes in the tunnelling conditions. In the second part, complementary information about preferred sites of adsorption at different coverage, through first principles simulations, are presented. Finally, formation of electronic states in the fundamental gap is studied. Photoluminescence (PL) technique was used to follow the changes in the electronic properties at the interface.

4.2 Chemisorption of Maleic anhydride on Si(100)-2x1.

Maleic anhydride ($C_2H_2 - C_2O_3$) is a 5- membered heterocyclic species with a C=C double bond as shown in the Fig. 4.1. Previous studies of maleic anhydride on Si(100)-2x1 were carried out and a brief description of them is given below.



Fig. 4.1 Structural formula for maleic anhydride molecule on the left. Also, a ball-and-stick model on the right.

By comparison with the behavior of other unsaturated molecules on Si(100)-2x1, e.g. cyclopentene [6,7], it was anticipated that the maleic anhydride molecules would adsorb on the top of the silicon dimer in a di- σ fashion [13]. In particular, it was expected

an ethylene-like adsorption behavior, therefore it is important to mention that ethylene was the first organic molecular adsorbed on Si(100) for which a structure was determined [14], and so this adsorption structure is mimicked by many other alkenes. This di- σ bond is also present in the case of acetylene adsorption on Si(100)-2x1, see Figs. 4.2a, b [11]. In addition, two configurations with four Si-C bonds, where a single C-C bond remains, were considered in the same study and referred to as tetra- σ bond, Figs. 4.2c, d.

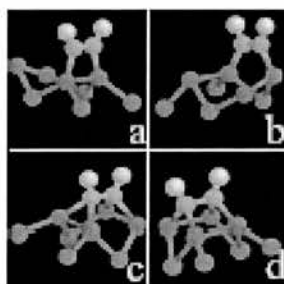


Fig. 4.2 Adsorption sites of acetylene C_2H_2 on Si(100)-2x1: (a) parallel and above a single dimer, (b) perpendicular to dimer rows, bonded off-centre at the end of adjacent dimers, (c) perpendicular to dimer row with four Si-C bonds, (d) parallel to dimer row with four Si-C bonds.

Adsorption of MA on Si(100) has been previously studied through a combined near edge X-ray absorption fine structure (NEXAFS) and high resolution electron energy loss spectroscopy (HREELS) [15]. It was reported that at low coverage the adsorption occurs mainly through cycloaddition of the C=C bond to the dangling bonds of Si-Si dimers (Fig. 4.3).



Fig. 4.3 Model of expected maleic anhydride adsorption on Si(100)-2x1. A [2+2] cycloaddition is formed through C=C and Si=Si dimer.

In general, those reports have shown that, at low dosages, molecules adsorb through a rehybridization of the carbon atoms in the olefin bond from sp^2 to sp^3 [15], although, the vibrational study also indicated that at higher coverage, the majority of maleic anhydride molecules are attached to the silicon dimers through a single Si-C bond via C-H bond cleavage. The observed rehybridization at low coverage points to reactions I or II (Scheme 1), in which maleic anhydride adsorbs above a silicon dimer through a direct [2+2] cycloaddition or in an inter-row adsorption site between adjacent dimers in a [1+2+1] addition, respectively. At higher dosages, an additional reaction path arises, in which the unsaturated molecule bonds to one side of the silicon dimer with the olefin bond preserved and formation of an Si-H bond (reaction III), which has been attributed to the presence of surface defects [15]. As it is noticeable, there is a coverage dependence of adsorption sites for MA on clean Si(100)-2x1.

It is important to mention that the cycloaddition reactions are subject to the Woodward-Hoffman selection rules, which are based on analysis of frontier orbital theory about the symmetries of the HOMO and LUMO of the reactants as they come together to form the reaction product. In this case, the frontier π orbitals must overlap “in phase” for the reaction to be symmetry allowed. Because of the particular properties of the π orbitals, involving organic compounds, in the [2+2] reaction, [2+2] cycloadditions are

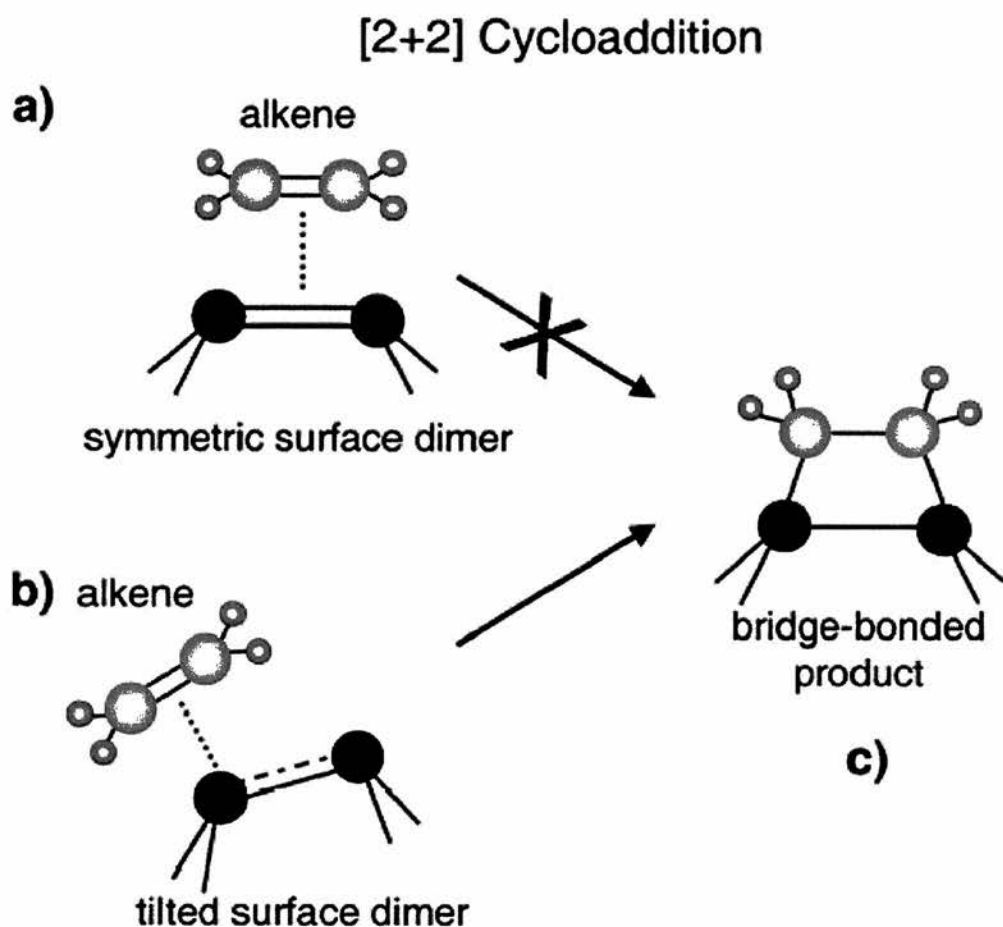


Fig. 4.4 A [2+2] reaction at the silicon surface occurs between an alkene molecule and the silicon dimer. The product is bridge-bonded across the dimer. Figure taken from S. Bent [16].

4.3 HREELS study

4.3.1 Adsorption of MA on Si(100)

High resolution electron energy spectroscopy technique provides chemical information about bonding between maleic anhydride and the substrate. Thus, spectrum (a) in Fig. 4.5 shows the HREEL spectra of Si(100)-2x1 exposed to 3 L maleic anhydride at room temperature. In the HREEL spectrum (a), a distinctive loss feature is present at 2960 cm^{-1} , which can be rather straightforwardly assigned to the $\nu(\text{C-H})$ stretching mode

of singly bonded C-C downshifted from 3120 - 3180 cm^{-1} [17] of $\nu(\text{C-H})$ vibrations for sp^2 carbon atoms in the parent molecule. Therefore it should suggest, at a dosage of 3 L, maleic anhydride molecules chemisorb mainly in a di- σ configuration with a rehybridization of the olefin C=C bond (Fig. 4.3). Consequently, no disruption of C-H bonds occurs and significant loss intensity at 2080 cm^{-1} , which could be ascribed to the $\nu(\text{Si-H})$ stretching mode, is absent. A dissociated hydrogen atom is expected to bond to one of the nearest silicon dimer atoms. By comparison with infrared data of molecular maleic anhydride, the loss features at 440 cm^{-1} and 1050 cm^{-1} are assigned to a $\beta(\text{C=O})$ bending mode and the shoulder at 1205 cm^{-1} to a $\beta(\text{C-H})$ bending mode [17]. In addition, the $\nu(\text{C-O})$ stretching modes may also contribute to the loss features at 1050 cm^{-1} and at 1205 cm^{-1} . *Ab initio* calculations of maleic anhydride in a di- σ configuration on a silicon cluster indicate that the peak at 770 cm^{-1} can be assigned to an out-of-plane $\gamma(\text{C-H})$ bending mode [15]. The $\nu(\text{C=O})$ stretching vibrations of the anhydride group contribute to the tail of loss intensity at 1700 cm^{-1} [17]. The weak structure at 2300 cm^{-1} is most likely due to combination losses.

It seems evident from the HREELS data, that maleic anhydride chemisorbs on Si(100)-2x1 in a di- σ coordination with the anhydride group directed from the surface plane (Fig. 4.2). This finding contrasts the observation made in an earlier HREELS study, where Si(100)-2x1 was exposed to 20 L maleic anhydride [18]. The di- σ coordination of maleic anhydride in this study is attributed to the reduced dosage of 3 L. It is plausible to assume that at higher dosages, maleic anhydride chemisorbs also on defect sites with a single Si-C bond. Thus the HREELS data and the previous work [6,18] match with the [2+2] cycloaddition scheme proposed until now.

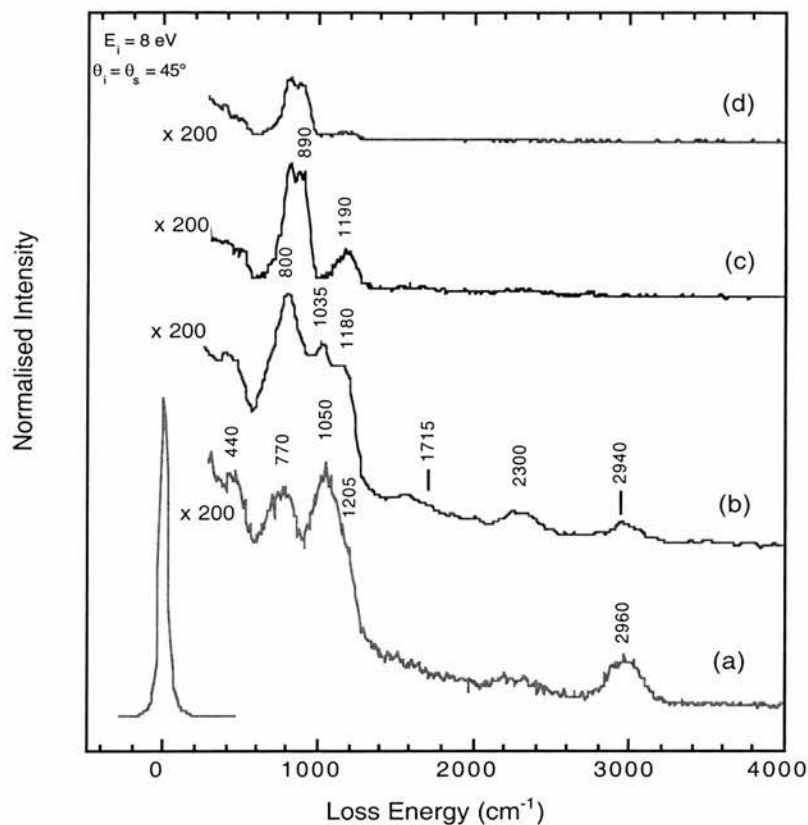


Fig. 4.5 HREEL spectra of 3L maleic anhydride adsorbed on Si(100)-2x1 (a) at room temperature, (b) after heating the sample to 805 K, (c) 970 K and (d) 1115 K.

4.3.2 Thermal decomposition of maleic anhydride.

The corresponding HREEL spectra of maleic anhydride/Si(100)-2x1 heated to 805 K, 970 K and 1115 K are shown in Figs. 4.5 (b)-(d). After heating the maleic anhydride overlayer to 805 K, the most intense peak is observed at 800 cm^{-1} and two smaller features are present at 1035 cm^{-1} and 1180 cm^{-1} . Since the peak at 800 cm^{-1} is also present after heating the substrate to more elevated temperatures, this loss feature is assigned tentatively to Si-C vibrations of maleic anhydride fragments. The peaks at 1035 cm^{-1} and

1180 cm^{-1} are most likely due to ring stretching mode [17]. In comparison with spectrum (a), the relative intensity of the $\nu(\text{C-H})$ stretch is significantly reduced.

It is evident that a thermally induced rearrangement and partial decomposition of the maleic anhydride layer has occurred. However, it should be noted that it was not observed a pressure rise which would have pointed to the desorption of molecule fragments. At temperatures above 970 K, it was observed a complete decomposition of chemisorbed maleic anhydride species and partial desorption of fragments. Loss intensities due to $\nu(\text{C-H})$ stretching, $\nu(\text{Si-H})$ stretching and $\nu(\text{C=O})$ stretching modes, respectively, are completely absent in the vibrational data. The loss intensities at 800 and 1190 cm^{-1} are due to $\nu(\text{Si-C})$ and $\nu(\text{Si-O})$ stretching vibrations [19,20]. The loss intensities at 890 cm^{-1} is most likely caused by $\nu(\text{Si-C})$ vibrations of three-dimensional SiC islands which are observed after high temperature treatments of silicon samples [20,21]. At this stage, the silicon surface consists of oxide and SiC structures. Heating the sample to 1115 K causes a significant decrease of Si-O related vibrational modes (spectrum 4.5d) in comparison with curve 4.5c which is indicative of the desorption of silicon oxide from the surface.

4.4 STM study of maleic anhydride on Si(100)-2x1

STM has been used to study the adsorption sites of maleic anhydride on Si(100)-2x1 surface at low coverage, in the submonolayer regime. Fig. 4.6 shows two different coverage with a predominantly adsorption of maleic anhydride in an inter-dimer sites, which can be seen as bright protrusions on those images. This adsorption site seems independent of the low coverage, well below to one monolayer, of this molecule, as shown in Figs. 4.6a, b. Both filled state STM images were taken at high resolution where the reconstruction of the surface after adsorption are seen as honey-comb reconstruction. A detailed analysis of the image (b) shows that more than 98% of maleic anhydride

molecules adsorb on inter-row positions. In areas of otherwise clean silicon, the adsorption of maleic anhydride induces a local $c(4\times 2)$ reconstruction of silicon dimers. The analysis also indicates the lack of a preferential adsorption of the unsaturated molecules at surface defects.

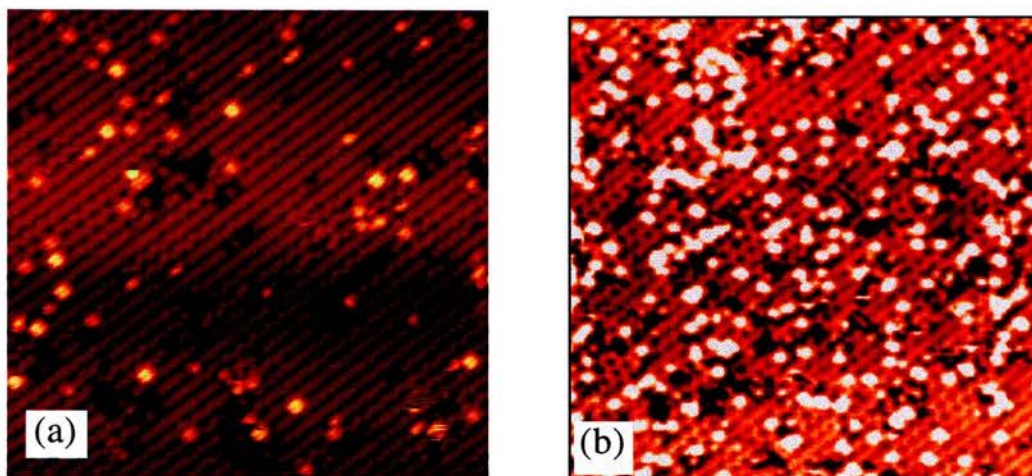


Fig. 4.6 Filled state STM images of maleic anhydride at different coverage. (a) Image ($220 \text{ \AA} \times 220 \text{ \AA}$) of 0.03 ML maleic anhydride adsorption at room temperature recorded at bias voltage -2.46 V , while (b) ($250 \text{ \AA} \times 250 \text{ \AA}$) corresponds to 0.15 ML maleic anhydride adsorption obtained with -1.8 V .

Coming through details of these features in a smaller scale, it is found that the Fig. 4.7a shows a filled state image of 0.03 ML maleic anhydride chemisorbed on Si(100)- 2×1 , where one monolayer (ML) corresponds to one maleic anhydride molecule for each silicon dimer. Two silicon terraces are present on the surfaces, which are separated by a single-height atomic step. On both terraces, the surface structure consists mainly of rows of symmetric dimers. However, at surface defects and at the step edge, zigzag rows of asymmetric dimers can be seen. Chemisorbed maleic anhydride molecules appear as brighter features in a butterfly shape, which are located almost exclusively between dimer rows.

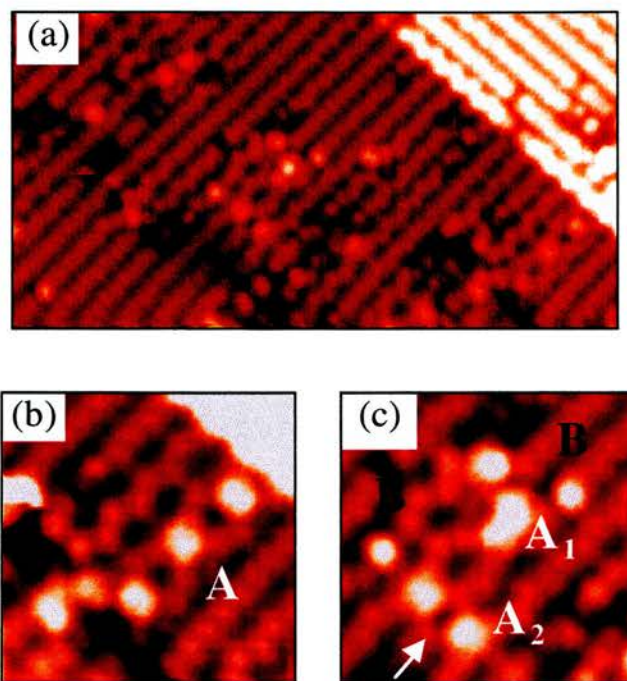


Fig. 4.7 Filled state images of 0.03 ML maleic anhydride on Si(100)-2x1 ($V_b = -2.3V$). (a) In the image ($200 \text{ \AA} \times 100 \text{ \AA}$), two silicon terraces are present which are separated by a monolayer step. Details of adsorbed molecules are shown in (b) and (c) ($50 \text{ \AA} \times 50 \text{ \AA}$). The arrow in (c) indicates most likely a broken silicon dimer bond.

In Fig. 4.7 b, three brighter objects (labelled A) are located between two dimer rows. Note that the chemisorption of the three maleic anhydride molecules, which are separated by two vacant adsorption sites along [011], leads to a local rearrangement or pinning of asymmetric silicon dimers. Also, the bright area in the top-left corner is the elevated adjacent silicon terrace. In Fig. 4.7c, two different adsorption geometries can be clearly distinguished. Two molecules are adsorbed on adjacent inter-row sites between the same dimer rows (A1) and two molecules on inter-row sites between neighboring dimer rows (A2). In addition, two brighter objects can be observed which are located on a dimer row (B). In the proximity of the adsorption sites, zigzag shaped asymmetric dimers are present. The arrow indicates most likely a broken silicon dimer bond between the two

adsorbed maleic anhydride molecules (A2), which will be discussed later in the following paragraph.

It is evident from the STM images that, at low coverage, maleic anhydride chemisorbs at room temperature almost exclusively on inter-row adsorption sites (reaction II in Scheme 1) which contrasts the observation made for unsaturated organic molecules previously studied [2,7]. In reaction II (also reaction I), the adsorption on inter-row sites involves the rehybridization of the carbon atoms in the olefin bond from sp^2 to sp^3 and the formation of two σ -like Si-C bonds between maleic anhydride and substrate. The *ab initio* Hartree-Fock calculations for the electrostatic potential, at the HF/6-31G* level [22], of free maleic anhydride indicates a substantial molecular dipole due to a charge transfer from the carbon to the oxygen atoms in the anhydride group. The charge transfer also lead to a strong electrophilic behavior of the organic compound, which is observed in many cycloaddition reactions of this molecule. In contrast, ethylene and cyclopentene, both of which prefer to adsorb on top of silicon dimers, do not possess such an electrostatic dipole.

Detailed self-consistent calculations of the electronic properties of reconstructed Si(100) surfaces by Zhu et al. [23] showed that the charge transfer from the “down-buckled” to the “up-buckled” silicon atom in the asymmetric dimer induces an electric dipole along the dimer axis, i.e., the upper atom is relatively electron rich. In the case of a $c(4 \times 2)$ -reconstruction, in adjacent rows “up-buckled” silicon atoms, which are negatively charged, are separated by 4.9 Å [23]. Thus, it is plausible to suggest that the electrophilic and polarized maleic anhydride molecule preferentially adsorbs on an inter-dimer row site between two “up-buckled” Si atoms in a [1+2+1] addition rather than on top of a single, neutral but polarized silicon dimer in a [2+2] cycloaddition. It is also expected that removal of the π -interaction in the silicon dimer by the adsorption of maleic anhydride leads to a lengthening of the Si-Si dimer bond. It should be noted that at room temperature, asymmetric dimers are known to rapidly switch orientation due to the low

activation energy involved so that dimers can appear to be symmetric in STM [24]. Domains of static asymmetric dimer structures are typically observed only at surface defects and step edges in room-temperature experiments [24].

Figure 4.8 shows the result of this cluster calculation at the AM1 level of two maleic anhydride molecules on $\text{Si}_{33}\text{H}_{35}$, which models the situation (A2) in Fig. 4.7c. The maleic anhydride molecules were assumed to have adsorbed in a trans geometry relative to one another. The silicon atoms in the two lowest layers were constrained in their positions to simulate bulk silicon (Si-Si distance $d_{\text{bulk}} = 2.35 \text{ \AA}$). The calculations show that the Si-Si bonds in the outermost dimers have increased from 2.38 \AA [25] to 2.5 \AA and the separation between silicon atoms, which are bonded to a common maleic anhydride molecule, is $d_{\text{SiMA-SiMA}} = 4.5 \text{ \AA}$ reduced from 5.0 \AA [25]. Note that the distance between the initially dimerized silicon atoms in the top layer between the maleic anhydride molecules is 3.1 \AA , which is substantially larger than observed in crystalline silicon. A Si-Si distance of 3.1 \AA points to a dramatic weakening of the σ -interaction between the silicon dimer atoms, which may lead to the breaking of the Si-Si bond. The *ab initio* calculations at the HF/6-31G* level for a $\text{SiH}_3\text{-(C}_4\text{H}_2\text{O}_3\text{)-SiH}_3$ cluster suggest a Si-Si distance of 3.58 \AA for the fully relaxed structure. Those calculations also show that the total energy of that cluster increases by 0.73 eV if the Si-Si distance is strained to 4.5 \AA . This relatively large strain energy suggests that the lower-level calculations on the larger cluster may misrepresent the nature of the Si-Si bonding between two adsorbates. A more accurate model might show that the Si-Si dimer bond is cleaved by adsorption of two maleic anhydride molecules to either side of the dimer, allowing $d(\text{Si-C}_4\text{H}_2\text{O}_3\text{-Si})$ to adopt the favored distance of 3.58 \AA .

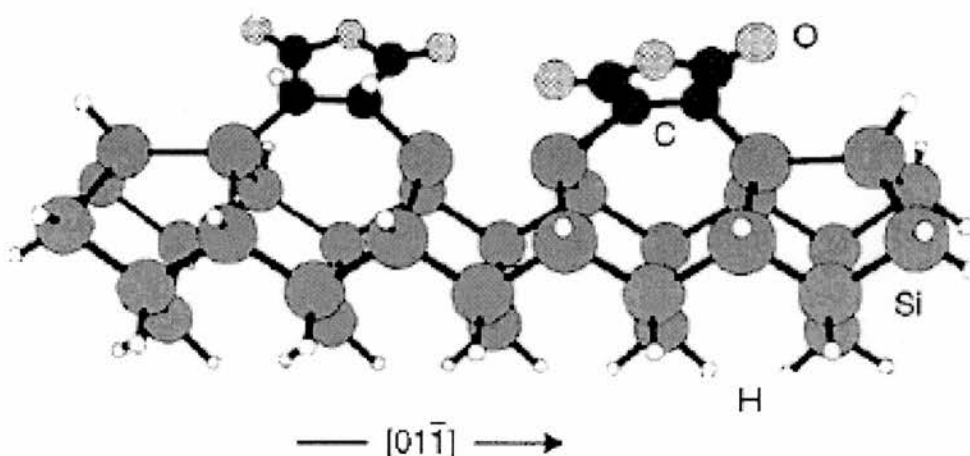


Fig. 4.8 Optimized geometry of two maleic anhydride molecules in a trans configuration of $Si_{33}H_{35}$. The cluster calculations have been carried out at the AM1 level. [12]

STM indicates that very few maleic anhydride molecules adsorb on top of silicon dimers (type B of Fig. 4.7c). In the case of missing silicon atoms we would expect that maleic anhydride molecules adsorb through a C-H bond cleavage with the double C=C bond being preserved (reaction path III in Scheme 1) as found at high coverage [18]. This chemisorption path would involve bonding of the dissociated hydrogen to one of the neighboring unsaturated silicon atoms. Unfortunately, the STM images do not provide evidence for the presence of Si-H bonds so that a direct [2+2] cycloaddition on intact silicon dimers (reaction I) cannot be ruled out as the interpretation of type B features. Note that type B features may also arise from contaminant species.

4.5 Influence of tunnelling conditions on maleic anhydride STM images.

4.5.1. Constant current

Detailed description of adsorption site of maleic anhydride has been done in the previous sections through STM experiments and theoretical calculation. Now, this section is focused on the difference of the appearances of MA involving a ranging of sample bias voltage. Fig. 4.9 shows a sequence of filled state STM images in the voltage range from

-2.7 up to -1.0 V at the same tunnelling current of 0.13 nA. Line profile for a single molecule is presented inset on each of those images (Figs. 4.9 b-g).

Changes in the tunnelling conditions leads to changes in filled state the STM images involving major contributions from silicon atoms instead of maleic anhydride molecule when the sample bias voltage is reduced. Figs. b, c and d were taken at sample bias voltage of -2.7, -2.5 and -2.0 V, respectively, there dimer rows are clearly visible and the maleic anhydride molecule are present as before, as bright protrusions. While Figs. e, f and d were taken at sample bias voltage below to -2.0V (-1.8, -1.5 and -1.0V, respectively). From this sequence, the maleic anhydride features changes its brightness until vanishes at -1.0 V. Line profile show that the intensity of those bright protrusions, reflecting the height of MA contribution, is also decreasing. Their apparent height varying from 1.2 Å (at -2.7 V where it has its maximum) to 0.2 Å (at -1.5 V) when it is still visible. But at -1.0 V the maleic anhydride feature appears as a depression, reflected into the line profile inset in Fig. 4.9 g.

In addition, STM images, Figs. 4.9 a and h, taken from the same region show clearly the surface appearance in the filled state and empty state, including silicon dimer rows and silicon atom rows, respectively. The contrasts show remarkably well the difference in the appearance of the same molecule, as protrusions and depressions, when the tunnelling current flow from the sample (filled state STM image) to the tip and *vice versa* (empty state images).

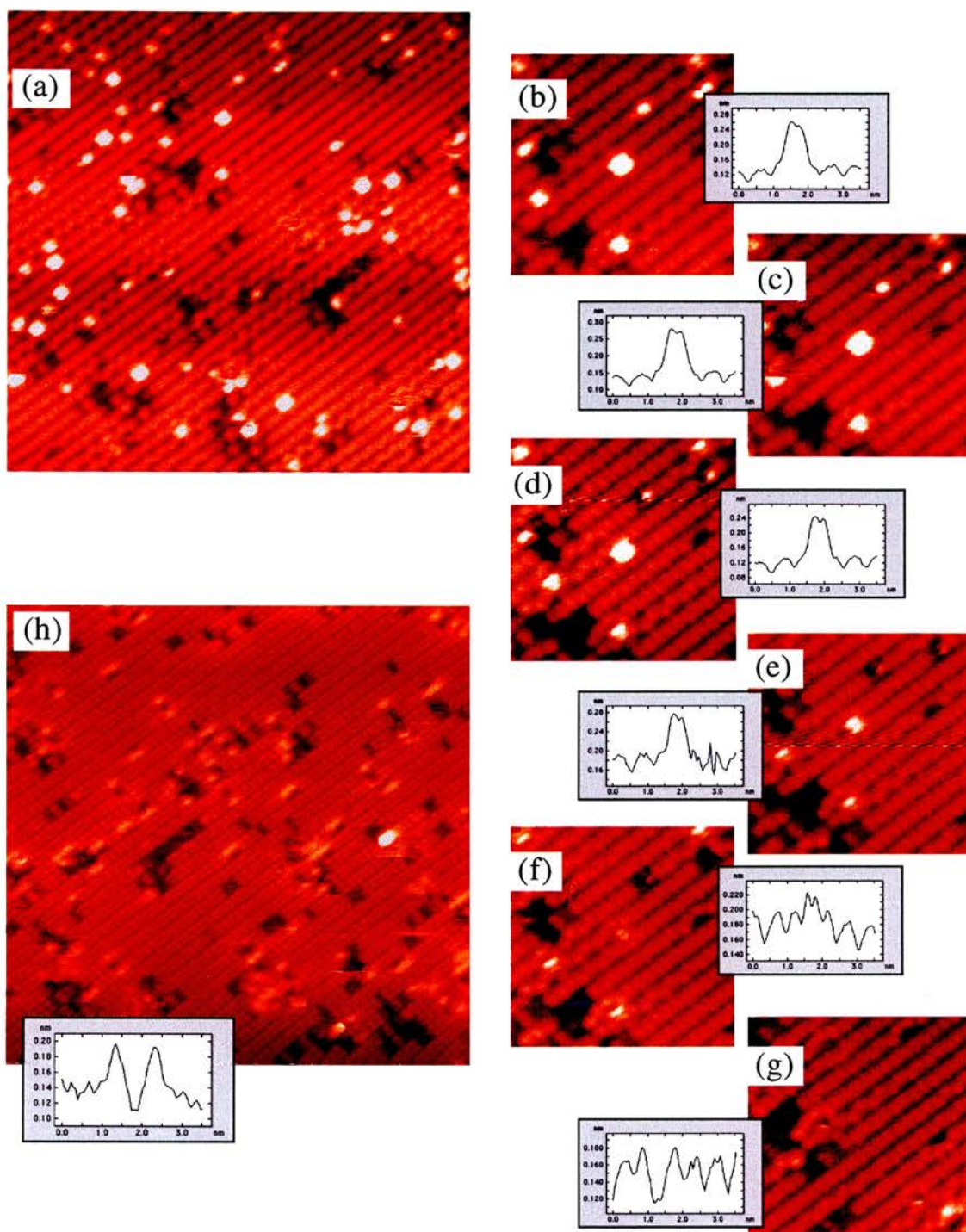


Fig. 4.9 A sequence of filled state STM images ($7.8 \text{ nm} \times 7.8 \text{ nm}$) at different sample bias voltage ranging from -2.7 V up to -1.0 V at 0.13 nA , (a)–(g), within a line profile inset of each image. (h) Shows an empty state image ($22.4 \text{ nm} \times 22.4 \text{ nm}$) of the same region as presented in (a).

4.5.2. Constant voltage.

In contrast to the changes in the constant current images (Fig. 4.9), changes in the tunnelling current seem to be less dramatic. The current was varied from 0.186 to 0.020 nA at sample bias voltage of -2.46 V, see Figs. 4.10 a-e. Their apparent height vary from 0.8 Å to about 0.2 Å. In all the cases the bright protrusion regarding maleic anhydride molecule are present within its characteristic butterfly shape.

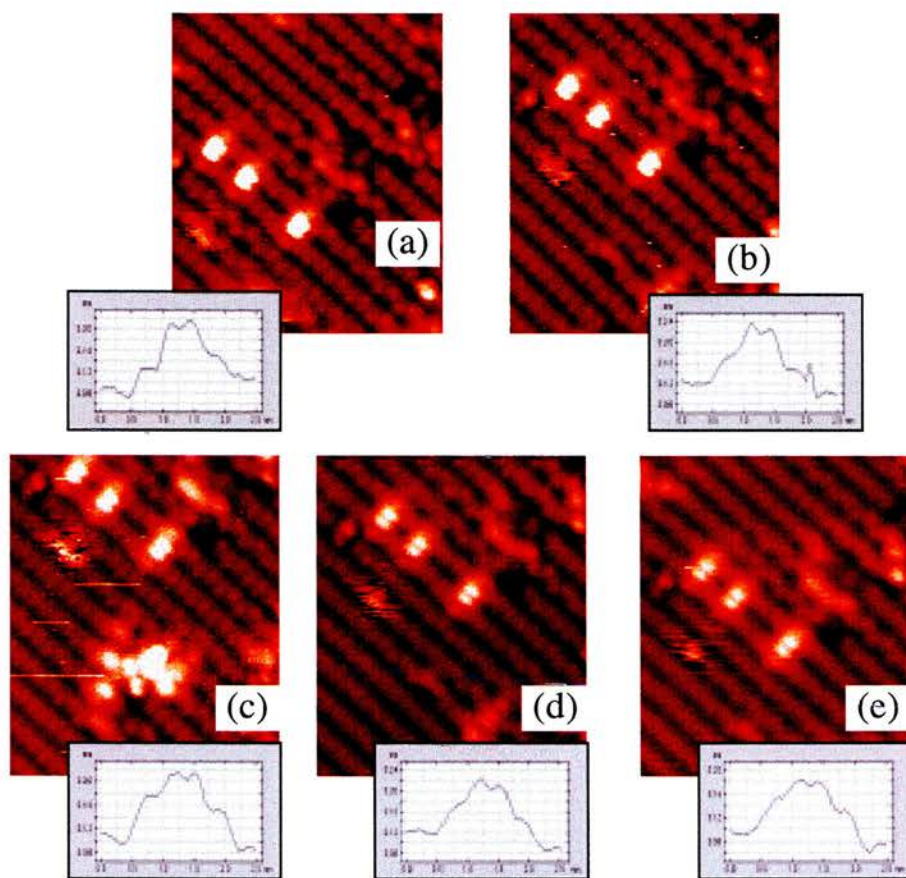


Fig. 4.10 Series of filled state STM images (6.8 nm \times 8.6 nm) at constant sample bias voltage -2.46 V. The current is varied from 0.186 nA to 0.020 nA in (a)–(e).

4.6 Simulations of scanning tunnelling images.

The outstanding STM results obtained at different tunnelling conditions inspired a close collaboration with Dr. Werner Hofer, Dept. of Physics and Astronomy -University

College London, to follow these results through advanced calculations of the MA/Si(100) system. Those results were published in Chem. Phys. Lett. [26], but the relevant information is given in the following paragraphs.

First principles density functional theory (DFT) calculations of the molecular adsorption on Si(100) have been performed in order to clarify the inhibition of [2+2] cycloaddition on top of the Si dimers. In addition, it has been simulated scanning tunnelling microscopy measurements of the adsorbed molecules in different adsorption geometries. The result of those calculations is unambiguous: the inter-dimer adsorption site is favored in all situations, where the silicon dimer bond is not substantially weakened. This limits inter-dimer adsorption to the low coverage regime below one molecule per about eight silicon dimers (1/8 ML). An analysis of the molecular orbitals shows that the main contributions to the tunnelling current are due to tunnelling processes into only two orbitals. By choosing the bias voltage the current flow into one of these orbitals, at about -2 eV below the highest occupied state, can be switched on, which changes the simulated corrugation by about 0.5 Å. This height difference is easily resolved in STM experiments.

The groundstate of the isolated molecule and the molecule adsorbed on Si(100)-2x1 was calculated with the Vienna *ab initio* Simulation Package (VASP) [27,28]. The method is based on nonlocal pseudo-potentials for the ion cores. The ultrasoft pseudo-potentials were of the Vanderbilt type [29]. Exchange correlations were described by the generalized gradient approach (GGA) of Perdew et al. [30] (PW91). The Brillouin zone of the silicon surface was sampled by (4x4x1) *k*-points of a Monkhorst–Pack grid [31]. The energy cutoff in all calculations was about 300 eV. Forces on single atoms in the final iterations were less than 0.01 eV/Å. The same method was used to calculate the electronic properties of the STM tip. For the tip it was used a pyramid model where the tungsten tetrahedron is terminated by a single tungsten atom [11]. In a final iteration the electronic properties of the tip were calculated with a single *k*-point, the Γ point of the surface Brillouin zone. The STM simulations are based on the Bardeen integral for the tunnelling

current between the sample surface and the STM tip. Details of the method are published elsewhere [32]. In STM scans on silicon surfaces the distance range under normal tunnel conditions (-2 V, 50 pA) is above 6 Å [33], therefore it expects the results of the simulations for this system, maleic anhydride on Si(100), to be free of errors due to atomic relaxations. By the same token it expects changes of the electronic surface structure due to tip potentials to be negligible. It has been shown previously that these changes occur only in the very low distance range (below 4.5 Å [34]), which is very rarely reached in experiments on semiconductor surfaces.

The relaxed surface geometry of Si(100) and its electronic structure have been calculated by a number of groups in the past [see for instance Ref. 23]. There it was found that the surface corrugation of the dynamically buckled dimers is about 0.5 Å. In the STM experiments with negative sample bias the anhydride molecules appear as protrusions, located at inter-dimer sites, their apparent height varying from 0.7 to about 1.2 Å (see Fig. 4.11), depending on the sample bias voltage. The maximum height was obtained at -2.7 V [26].

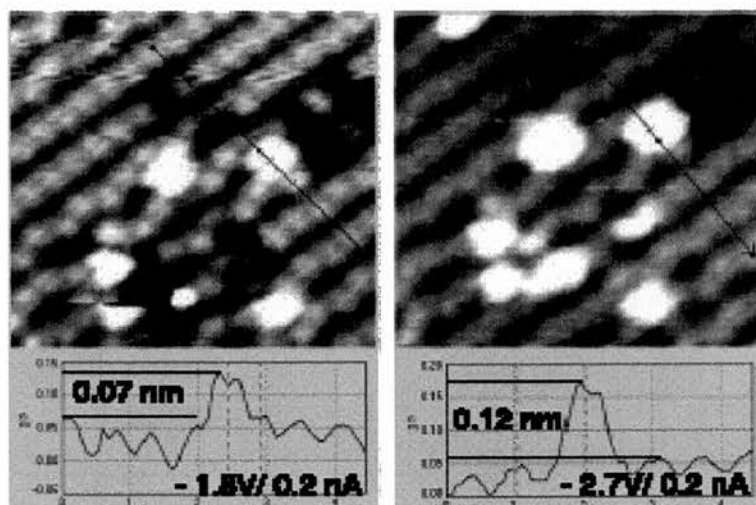


Fig. 4.11 STM images of maleic anhydride on Si(100) for two different bias voltages. In both images, the molecule is shown adsorbed between the silicon dimer rows. Note some irregular features in the images, which are due to surface defects and fragments of broken molecules. The left image was

recorded at $V_{bias} = -1.8$ V, the right image at $V_{bias} = -2.7$ V. The tunnelling current was 0.2 nA. The corrugation of the molecule is enhanced by 0.05 nm due to the increased bias voltage [26].

It was calculated four different setups with the first principles method, three of them for a Si(100)-2x1 surface, and one for the Si(100)-4x1 surface cell (see Fig. 4.12). (i) The [2 + 2] reaction, with the anhydride molecule on top of silicon dimers. (ii) A modified cycloaddition, where the molecule attaches itself to the end of two adjacent dimers along the dimer rows. (iii) An adsorption at the inter-dimer site on Si(100)-2x1. (iv) An adsorption at the inter-dimer site on Si(100)-4x1. The silicon surface was simulated by an eight layer (Si(100)-2x1) or a four layer (Si(100)-4x1) silicon film, separated from its adjacent film in the supercell geometry by more than 10 Å. The bottom layer was in every case passivated with hydrogen.

The reacted surfaces for the four adsorption geometries are shown in Fig. 4.12. In all cases, it started with the molecule close to the reaction position and relaxed the molecule and the surface atoms till the forces on the ions became negligible. In the final geometry, the electronic density distribution and the total energy of the systems were calculated. Comparing the total energy of the clean Si(100) surface, the total energy of the isolated molecule and the total energy of the coupled system, it was obtained the adsorption energy of the molecule in different reactions.

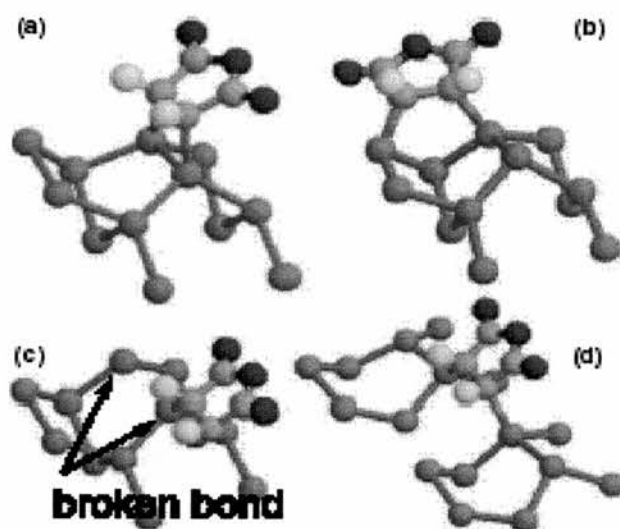


Fig. 4.12 Molecular adsorptions on the Si(100) surface. The images show the final setup in the simulations. (a) [2+2] cycloaddition, (b) molecule attached to the end of two dimers, (c) inter-row adsorption for high coverage (1/2 ML), and (d) inter-row adsorption for lower coverage (1/4 ML) [26].

Initially, the highest adsorption energy of 1.35 eV was achieved for a cycloaddition reaction (Fig. 4.12a). The modified reaction, where the molecule attaches itself to the end of two adjacent dimers, was marginally less favorable with 1.27 eV (Fig. 4.12b). At this stage it was obtained the lowest adsorption energy of only 0.29 eV for the inter-dimer site (Fig. 4.12c). The breaking of the silicon dimer bond reduces the adsorption energy in this case. This in turn reflects the strain on the lattice, because the two Si-atoms of the dimer are moved laterally by more than 0.5 Å to accommodate the adsorbed molecule. Experimentally, this would correspond to a situation where the surface coverage is 1/2 ML and where, furthermore, the anhydride molecules are in line. In STM images there is indeed evidence for the cleavage of the silicon dimer bond if two anhydride molecules adsorb on adjacent inter-row sites (Fig. 4.7c). However, this feature is observed very rarely, presumably owing to its substantially lower adsorption energy. The adsorption energy obtained on the Si(100)-2x1 surface is too low because in this structure every

inter-row position is occupied. For this reason it was also studied the adsorption on a larger unit cell. On a Si(100)-4x1 cell the coverage is lowered to 1/4 ML. Even though this value is still higher than under experimental conditions, it allows a detailed understanding of the energetics involved in the inter-row adsorption. The adsorption geometry is shown in Fig. 4.12d. For this reaction, an adsorption energy of 0.93 eV was obtained.

The energy for the inter-row adsorption is still about 0.4 eV less than for a cycloaddition reaction. But it involves a too high coverage. The coverage of 1/8 ML has not been calculated directly, because even for pseudo-potential methods the system size is larger than a reasonable timescale of computation allows for. Instead, the energetics was analyzed and show that the inter-row reaction is favorable in the low-coverage regime. The energy components which are important for the adsorption process are: (i) The Si-C bond energy, which has to be determined using the total energy calculation and accounting for the lattice strain. The bond energy is about -2.11 eV. (ii) The lattice strain can be calculated by computing the total energy of the Si-lattice in its fully relaxed state and after the adsorption of an anhydride molecule. The strain energy is +1.28 eV. The main contribution to the strain should be due to the strain on the Si-Si dimer bonds. The effect of surface coverage can be estimated by two different methods: either elasticity theory, or direct calculation. The elastic energy of the strained lattice is proportional to the square of the displacement. The point of expansion for the harmonic energy is the fully relaxed silicon surface without an adsorbed molecule. The appropriate elastic constant can then be determined from the strain energy at the coverage of 1/4 ML. Assuming, that the displacement is reduced by about 50% if the coverage is only 1/8 ML, we gain an elastic energy of 0.96 eV. This means that the adsorption energy for 1/8 ML coverage amounts to 1.89 eV, which is 0.54 eV higher than the adsorption energy in the [2 + 2] cycloaddition reaction (1.35 eV). Even a substantially smaller energy gain still leads to an adsorption energy well in excess of 1.35 eV. It has been checked the result by an independent calculation, where the computed electronic groundstate of a Si-Si dimer in a

frozen geometry for three different inter-atomic distances. Here the energy difference between the strained dimers ($d = 2:64 \text{ \AA}$, 1/4 ML; and $d = 2:48 \text{ \AA}$, 1/8 ML) is 0.58 eV. Considering only the contributions from the strain on the silicon dimers, the inter-dimer site for 1/8 ML coverage is energetically favored by at least 0.16 eV. This value is sufficient, at room temperature, where more than 99% of all molecules will be found at inter-row positions. The energy components from this calculation are summarized in Table 4.1. Due to the polarity of the anhydride molecule repulsive dipole interactions should also be present. We have not calculated these contributions explicitly, we note only that they will also decrease with decreasing surface coverage.

Table 4.1. *Energy components for different coverage in the inter-row adsorption geometry*

Energy (eV)	Coverage (ML)		
	1/2	1/4	1/8
Si-Si	+1.80	+0.96	+0.38
Lattice	-	+0.32	(+0.32)
Si-C	-	-2.11	(-2.11)
Total	-0.29	-0.93	-1.51

The energy of lattice strain and the Si-C bonds for 1/8 ML coverage are assumed to remain unchanged, the energy lost in the lengthening of the dimer bond has been calculated. It is clear, from these values, that the adsorption energy is highly coverage dependent.

The molecule remains intact in the adsorption process, the bond characteristics only change for the carbon atoms in the olefin bonds. This is clearly indicated by the bond lengths C(1)-O(5) and C(1)-O(6), which remain the same, 1.40 and 1.21 \AA , respectively, in all reactions. The number in brackets, e.g. C(1), refers to the atomic label

of the isolated molecule. These labels are shown in Fig. 4.13, inset at the bottom. It was noted that also the Si–C bonds are only slightly affected by different adsorption geometries, the bond length varies from 1.97 (see Figs. 4.12a, b) to 2.03 Å (see Figs. 4.12c, d). The bond lengths in different adsorption geometries are tabulated in Table 4.2.

Table 4.2. Bond lengths (Å) for different adsorption geometries of the molecule

Bond (Å)	Adsorption site		
	On-top (a)	End-dimer (b)	Inter-row (d)
Si–C(2)	1.97	1.97	2.03
C(1)–C(2)	1.54	1.56	1.60
C(2)–C(3)	1.50	1.51	1.50
C(1)–O(5)	1.40	1.39	1.38
C(1)–O(6)	1.21	1.21	1.21
C(2)–H	1.10	1.09	1.09

The labels for the adsorption sites refer to Fig. 4.12. The numbers, e.g. C(1), refer to the atoms of the isolated molecule as displayed in Fig. 4.13, inset at the bottom.

Within a perturbation approach, the tunneling current in an STM depends on the overlap of tip and sample orbitals. For this reason, it has been analyzed the density of states (DOS) and the orbitals of the isolated anhydride molecule. Since the C–O bonds do not change in the adsorption, it expects the states with the highest density on top of the anhydride molecule to be also the states contributing the most to the tunnelling current. From the constant density plots of molecular states, shown in Fig. 4.13, it is clear that only two molecular states, (18) and (20), will add substantially to the tunnelling current for a sample bias from 0 to -3 V. Both states have essentially p_z symmetry, here the electron density is a maximum above the atomic position. Their energy with respect to the

highest occupied state is -2.0 (18), and -0.56 eV (20). The onset of current contributions from state (18) is expected to be somewhat below -2.0 V bias voltage, but it should fully contribute for voltages below -2.5 V. In the DOS of the coupled system (Fig. 4.13, grey curve in the DOS frame) both states can be clearly distinguished. To establish unambiguously that this state plays the essential role in the increase of the corrugation amplitude it has also simulated LDOS contours for intervals of 0.1 eV. The upper bond of the interval was varied from -2.0 to -2.7 eV. The highest contour, by about 0.5 Å, was obtained for the intervals from -2.2 to -2.5 eV below the Fermi level. This broadening of the state due to hybridization with Si orbitals can be seen directly in the DOS of the coupled system (Fig. 4.13).

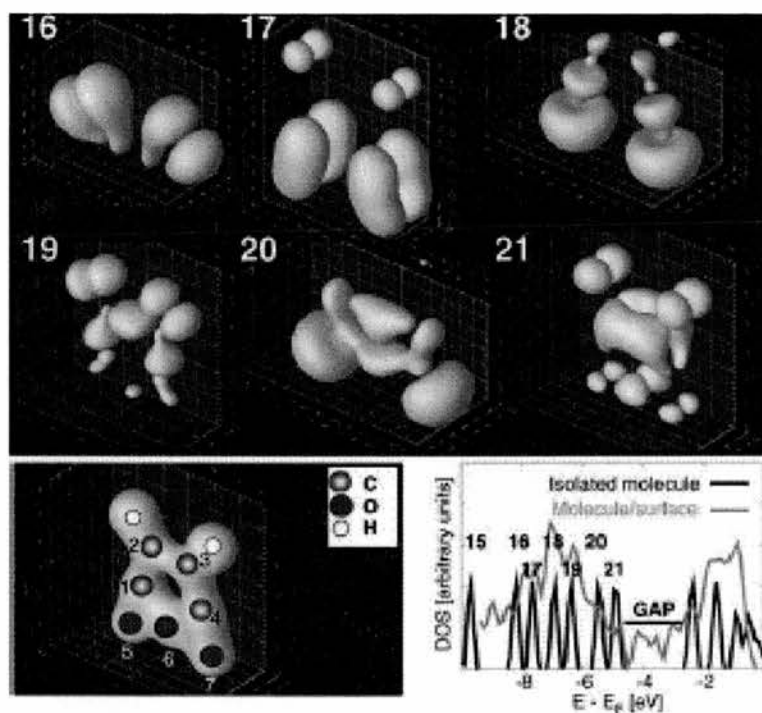


Fig. 4.13 Isolated maleic anhydride molecule. The density distribution of single states in the range of STM measurements is shown in the top frames, the total density distribution, the position of molecular atoms (left), and the density of states (right) in the bottom frames [26].

Only two states of the molecule, 18 and 20, possess a substantial density of charge beyond the oxygen atoms. Since the C–O bond is not substantially affected by the bonding to the surface, these states are also the only states with a substantial overlap with the STM tip orbitals. Both states can be clearly distinguished in the DOS of the coupled system (grey curve). The orientation of the molecule is upside down, so that the STM tip, in these frames, approaches from below.

Given the p_z character of the two dominant molecular states, the main current contributions should be due to the wavefunction overlap of these states with states of the STM tip. To show that tunneling via these states can indeed be unambiguously resolved it has simulated STM scans with -1.8 and -2.7 V and 0.2 nA, as in the STM experiments. It should be noted that the distance for currents this high is already rather low (in the range of 5 Å above the silicon surface). The difficulty, in these simulations, is the high protrusion of the molecule. It renders the approach less precise, because it only computes currents directed perpendicular to the surface. If the tip apex atom is close to the surface the error due to this assumption will increase. For this reason we can expect agreement between the simulation and the experiment only for the apparent height of the molecule, not for its exact shape in the measured STM images.

Comparing the simulation of the reacted surface with the simulation of the unreacted surface for identical tunneling conditions, it can be calculated the apparent height of the molecule on the surface. The results of STM simulations are shown in Fig. 4.14. The surface as it would appear with a coverage of 1/4 ML is given in the left images. The enlarged image on the right shows the position of the Si and O atoms. The anhydride molecule appears as a bright, two-lobed protrusion above the silicon surface. The molecule covers more than 50% of our unit cell. The qualitative features of the image do not depend on the bias voltage. The height difference between the two simulations amounts to 0.8 Å, which is reasonably well in accordance with the experimental value of 0.5 Å. The agreement of absolute values (apparent height 1.0 Å at -1.8 V, and 1.8 Å at -2.7 V versus 0.7 Å and 1.2 Å, respectively) is within the same error range.

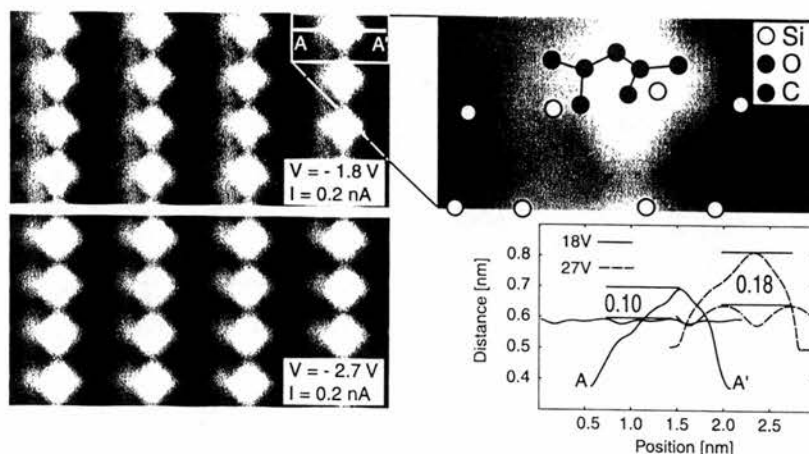


Fig. 4.14 Simulated STM images for two different bias voltages. Top: $V_{bias} = -2.7$ V. Bottom: $V_{bias} = -1.8$ V. The position of the anhydride molecule on the surface is shown in the enlarged image on the right. Simulated linescans are shown in the graph below (scan along A–A'). The two simulated scans are compared with simulated scans on a clean silicon surface. The offset between the two scans is chosen to facilitate the comparison, it is not a feature of the simulation itself. The change due to change of bias voltage (an increase of the corrugation of 0.8 \AA), is slightly higher than the difference obtained in the experiments [26].

To demonstrate the localization of state (18), which mainly contributes to the current in this range, we have simulated the current contours for energy intervals of 0.1 eV , from -2.0 to -2.8 eV . They are displayed in Fig. 4.15. In all intervals the contour maximum is on top of the molecule and exhibits a two-lobed shape similar to the charge density distribution of state (18) (Fig. 4.13). This signifies that the main current contributions in this voltage range are due to an electron state of the molecule, and not of the silicon surface. Furthermore, it can be seen from the contrast of the images, that the intervals from about 2.3 – 2.5 eV yield the highest localization. This is also the energy value of state (18) relative to the highest occupied level of the anhydride molecule, if we

allow for some broadening due to hybridization. The simulated STM images thus not only agree with the experiments, but they also provide a detailed understanding of the origin of the tunneling current. With the help of a theoretical analysis the increase in apparent height of the molecule can be traced back to the electronic structure of the molecule itself. What happens, when the bias voltage decreases to below -2.5 eV, is, in fact, a tuning in on the energy range of a single molecular state.

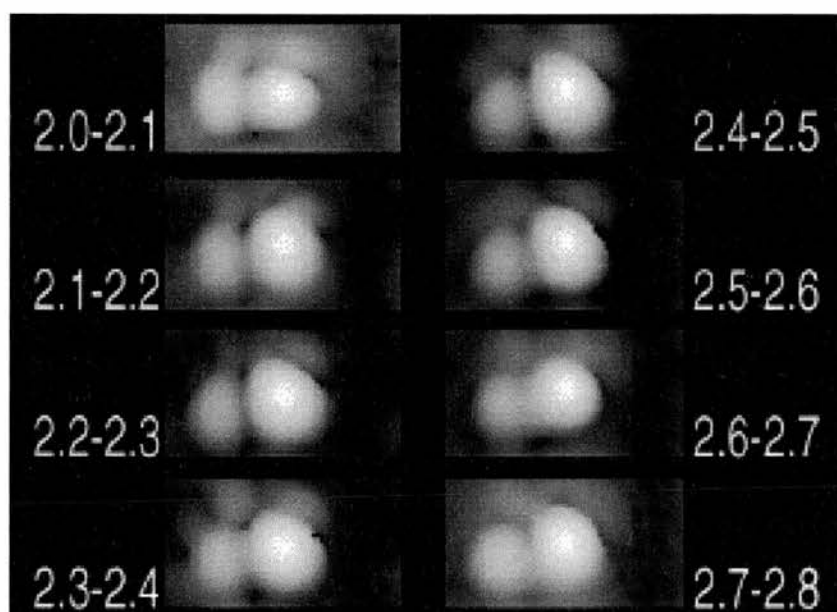


Fig. 4.15 Localization of the molecular state on the silicon surface. In this image we have simulated the current contour from selected energy intervals between 2.0 and 2.8 eV below the Fermi level. Black denotes the lowest, white the highest point of a current contour. The contours for 2.0–2.1 eV and 2.7–2.8 eV have a high local spread and a low contrast. The highest contrast, and thus the highest localization, is obtained at 2.3–2.5 eV. The contrast increase reflects the larger corrugation height of current contours in the middle intervals (about 3.5 Å) compared to the end intervals (about 2.8 Å) [26].

4.7 PL experiments

4.7.1 Formation of electronic states in the fundamental gap at MA/Si(100)-2x1

At the beginning in this chapter, it was stated that the adsorption of some organic molecules on silicon surfaces have been studied in some detail, but little is known about the electronic properties at the organic film/semiconductor interface. Details of the experimental set up were described previously in section 2.11.

Initially, after the removal of the native oxide layer, a density of gap states of $D_{it} = 2.6(3) \times 10^{12} \text{ eV}^{-1} \text{ cm}^{-2}$ at the Si(100)-2x1 surface it is observed (Fig. 4.16a). Later, the exposure of Si(100)-2x1 to maleic anhydride at room temperature reduces the gap state density to $1.8(2) \times 10^{12} \text{ eV}^{-1} \text{ cm}^{-2}$, which is slightly lower than the D_{it} determined for clean Si(100)-2x1, and it is attributed to the removal of pinned ordered asymmetric dimers. In order to calibrate the PL signal, the time evolution of the PL signal has been recorded after 3 L (1 Langmuir (L) = 1×10^{-6} Torr s) exposure to maleic anhydride/Si(100)-2x1 (Fig. 4.17a). It should be noted that the measurement of the time integrated PL signal only provides information regarding the relative change of the gap state density D_{it} . The solid line (a) in Fig. 4.17 shows the calculated PL transient of 3 L maleic anhydride/Si(100)-2x1 with an assumed $D_{it} = 1.8(2) \times 10^{12} \text{ eV}^{-1} \text{ cm}^{-2}$. Details of the calculations were described in chapter 1 (section 1.5).

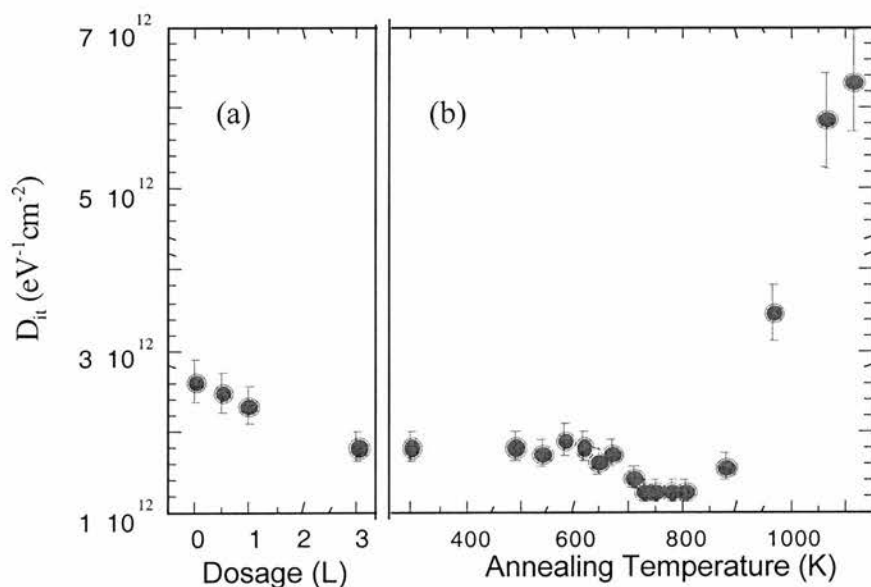


Fig. 4.16 Density of gap states D_{it} derived from PL measurements of silicon exposed to maleic anhydride at room temperature. (a) Evolution of D_{it} during

the sequential dosing of maleic anhydride; (b) D_{it} of 3 L maleic anhydride on Si(100)-2x1 after heating the sample for 30 s.

As can be seen in Fig. 4.17a, the calculated PL transient describes well the decay of the PL signal for times larger than the resolution of the detector.

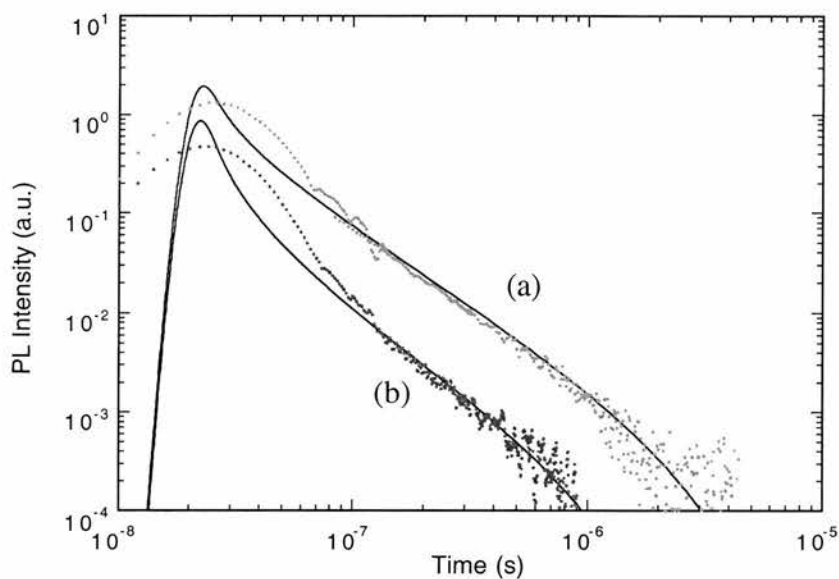


Fig. 4.17 PL transients (dots) of Si(100)-2x1 exposed to 3 L maleic anhydride at room temperature (a) and after heating the organic film to 1115 K (b). The superimposed solid curves are the calculated PL transients for silicon surfaces with $D_{it} = 1.8 \times 10^{12} \text{ eV}^{-1} \text{ cm}^{-2}$ (a) and $D_{it} = 6.8 \times 10^{12} \text{ eV}^{-1} \text{ cm}^{-2}$ (b).

However, the PL measurements indicate, the direct Si-C attachment of the organic molecules does not induce the formation of states in the fundamental gap at the silicon surface. Indeed, the chemisorption of maleic anhydride decreases slightly the gap state density.

4.7.2 Desorption of MA and changes in the electronic states.

Here, it is described the chemisorption of the model compound maleic anhydride on Si(100)-2x1 and the subsequent investigation of the gap state density at the organic film/semiconductor interface. The chemical characterization of the organic film was performed with HREELS.

The gap state density D_{it} after heating the maleic anhydride film for 30 s is shown in Fig. 4.16b. Three characteristic temperature ranges can be distinguished in Fig. 4.16b. Firstly, below an annealing temperature of 650 K, the gap state density is virtually constant. Above 650 K, the D_{it} decreases slightly to $1.3(2) \times 10^{12} \text{ eV}^{-1} \text{ cm}^{-2}$. Finally, at temperatures above 850 K the gap state density increases steadily to $6.4(6) \times 10^{12} \text{ eV}^{-1} \text{ cm}^{-2}$. The corresponding PL transient of maleic anhydride/Si(100) after heating to 1115 K is given in Fig. 4.17b. As observed for the room temperature film, the calculated PL transient, in which a gap state density of $D_{it} = 6.4 \times 10^{12} \text{ eV}^{-1} \text{ cm}^{-2}$ was assumed, describes well the exponential decay of the PL response to the pulsed laser light.

The PL measurements show clearly that heating of the organic film to temperatures above 900K increases the gap state density. Thus, it is plausible to suggest that the increase of D_{it} is related to the presence of silicon carbide on the silicon surface as indicated by the $n(\text{Si-C})$ stretching mode in the vibrational data. It is known that carbon impurities in silicon induce donor states in the fundamental gap at 0.35 eV and 0.87 eV above the valence band edge [35]. However, the diffusion rate of carbon atoms at temperatures below 1200 K is considerably less than $10^{-13} \text{ cm}^2/\text{s}$ [35] so that a significant insertion of carbon atoms into the silicon crystal can be neglected. Thus, it can be concluded that most of the carbon atoms remain on the surface after heating the sample to 1115 K in form of silicon carbide structures. It is likely that the lattice mismatch between carbide complexes and Si(100) surface may have lead to the formation of interfacial gap states. In addition, carbon atoms on the silicon surface may induce domains of ordered asymmetric dimers, which lead to the formation of gap states. However, it should be noted that HREELS is not able to provide detailed structural information of the decomposed maleic anhydride film.

4.8 Conclusions

In conclusion, this work shows unambiguously that the unsaturated maleic anhydride molecule adsorbs preferentially on inter-dimer sites in a [1+2+1] addition reaction. It is reasonable to suggest that the carbon atoms in the olefin bond rehybridize from sp^2 to sp^3 upon chemisorption. After the adsorption of maleic anhydride molecules on adjacent inter-dimer sites, it is observed the cleavage of the silicon dimer bond between two adsorbed molecules. The inter-row adsorption is the energetic minimum for the low-coverage regime. In addition, it is demonstrated by the *ab initio* analysis that STM experiments do reveal single molecular states of the reacted surface.

Also, the study has shown that the chemisorption of maleic anhydride on Si(100)-2x1 does not induce the formation of gap states at the silicon surface. In contrast, we observe that the sequential exposure of Si(100)-2x1 to maleic anhydride at room temperature results in a small reduction of the gap state density possibly due to the removal of ordered asymmetric dimer domains. Heating the organic film to temperatures above 650 K induces the partial decomposition of maleic anhydride and the further reduction of the density of surface states. However, the decomposition of maleic anhydride and almost complete removal of hydrogen and oxide structures from the silicon surface at temperature above 850 K leads to a significant increase of the gap state density.

References

-
- 1 C. Joachim, J. K. Gimzewski, A. Aviram, *Nature* **408**, 541 (2000).
 - 2 D. I. Gittins, D. Bethell, D. J. Schiffrin, R. J. Nichols, *Nature* **408**, 67 (2000).
 - 3 R. A. Wolkow, *Ann. Rev. Phys. Chem.* **50**, 413 (1999).
 - 4 C. C. Cheng, R. M. Wallace, P. A. Taylor, W. J. Choyke, J. T. Yates Jr., *J. Appl. Phys.* **67**, 3693 (1990).
 - 5 P. A. Taylor, R. M. Wallace, C. C. Cheng, W. H. Weinberg, M. J. Dresser, W. J. Choyke, J. T. Yates Jr., *J. Am. Chem. Soc.* **114**, 6754 (1992).

-
- 6 R.J. Hamers, J. S. Hovis, S. Lee, H. Liu, J. Shan, *J. Phys. Chem. B* **101**, 1489 (1997).
 - 7 J. S. Hovis, S. Lee, H. Liu, R. J. Hamers, *J. Vac. Sci. Technol. B* **15**, 1153 (1997).
 - 8 J. S. Hovis, H. Liu, R. J. Hamers, *Surf. Sci.* **402**, 1 (1998).
 9. J. Yoshinobu, H. Tsuda, M. Onchi, M. Nishijima, *J. Chem. Phys.* **87**, 7332 (1987).
 10. A. J. Fisher, P. E. Blochl, G. A. D. Briggs, *Surf. Sci.* **374**, 298 (1997)
 - 11 W. A. Hofer, A. J. Fisher, R. A. Wolkow, *Surf. Sci.* **475**, 83 (2001).
 - 12 T. Bitzer, T. Rada, N. V. Richardson, *J. Phys. Chem. B* **105**, 4535 (2001).
 - 13 T. Bitzer, T. Dittrich, T. Rada, N. V. Richardson, *Chem. Phys. Lett.* **331**, 433 (2000).
 - 14 J. Yoshinobu, H. Tsuda, M. Onchi, M. Nishijima, *J. Chem. Phys.* **87**, 7332 (1987);
A.J. Mayne, A. R. Avery, J. Knall, T. S. Jones, G. A. D. Briggs, W. H. Weinberg, *Surf. Sci.* **284**, 247 (1993).
 - 15 A. Lopez, T. Bitzer, T. Heller, N. V. Richardson, *Surf. Sci.* **477**, 219 (2001).
 - 16 S. F. Bent, *Surf. Sci.* **500**, 879 (2002), references therein.
 - 17 P. Mirone, P. Chiorboli, *Spectrochimica Acta* **18**, 1425 (1962).
 - 18 T. Bitzer, N. V. Richardson, *Appl. Surf. Sci.* **144-145**, 339 (1999).
 - 19 C. Huang, W. Widdra, X. S. Wang, W. H. Weinberg, *J. Vac. Sci. Technol. A* **11**, 2250 (1993).
 - 20 J. A. Schaefer, W. Göpel, *Surf. Sci.* **155**, 535 (1985).
 - 21 B. S. Swartzentruber, Y.-W. Mo, M. B. Webb, M. G. Lagally, *J. Vac. Sci. Technol. A* **7**, 2901 (1989).
 - 22 GAMESS, Schmidt, M. W.; Baldrige, K. K.; Boatz, J. A.; Elbert, S. T.; Gordon, M. S.; Jensen, J.J.; Koseki, S.; Matsunaga, N.; Nguyen, K. A.; Su, S.; Windus, T. L.; Dupuis, M.; Montgomery, J. A. *J. Comput. Chem.*, **14**, 1347 (1993).
 - 23 Z. Z. Zhu, N. Shima, M. Tsukada, *Phys. ReV.B*, **40**, 11868 (1989).
 - 24 R. A. Wolkow, *Phys. ReV. Lett.* **68**, 2636 (1992).
 - 25 R. M. Tromp, R. G. Smeenk, F. W. Saris, *Surf. Sci.* **133**, 137 (1983).

-
- 26 W. Hofer, A. J. Fisher, T. Bitzer, T. Rada, N. V. Richardson, Chem. Phys. Lett. 355, 347 (2002).
- 27 G. Kresse, J. Hafner, Phys. Rev. B **47**, R558 (1993).
- 28 G. Kresse, J. Furthmuller, Phys. Rev. B **54**, 16697 (1996).
- 29 K. Laasonen, R. Car, C. Lee, D. Vanderbilt, Phys. Rev. B **43**, 6796 (1991).
- 30 J. P. Perdew, J. A. Chevary, S. H. Vosko, K. A. Jackson, M. R. Pederson, D. J. Singh, C. Fiolhais, Phys. Rev. B 46, 6671 (1992).
- 31 H.J. Monkhorst, J.D. Pack, Phys. Rev. B **13**, 5188 (1976).
- 32 W.A. Hofer, J. Redinger, Surf. Sci. **447**, 51 (2000).
- 33 W.A. Hofer, A.J. Fisher, G.P. Lopinski, R.A. Wolkow, Phys.Rev.B **63**, 85314 (2001)
- 34 W. A. Hofer, A. J. Fisher, R. A. Wolkow, P. Grutter, Phys. Rev. Lett. **87**, 236104 (2001).
- 35 S. M. Sze, *Semiconductor Devices, Physics and Technology*, 2nd Ed. (John Wiley & Sons, New York 1981).

CHAPTER 5

Adsorption of Perylene on Silicon Surfaces

5.1 Introduction

Since the report of efficient organic electroluminescence (EL) from double-layered devices by Tang and Van Slyke [1], a number of attempts have been made to improve their emission spectral range, long-term stability, and further conversion efficiency [2,3]. Different classes of organic compounds have been newly synthesized for electron- and hole-transport layers (ETLs) and (HTLs) as well as emitting layers.

In the organic devices, carrier transport, and luminescent behaviour are remarkably governed by the solid state properties in thin films. Therefore, molecular aggregation, packing, and orientation also affect the device properties as well as the intrinsic molecular properties. Yanagi's group, working on organic photovoltaic cells, have reported that epitaxial growth of π -conjugating cyclic molecules such as porphyrin [4,5], and phthalocyanine [6] enhanced the conversion efficiency due to preferable molecular orientation for carrier generation and transport.

Organic field-effect transistors (OFETs) offer inherent advantages of low-cost, simple packaging, or compatibility with flexible and transparent plastics substrates requiring low operating voltages. Therefore applications such as identification tags or emissive displays are envisioned, in general as a viable alternative to more traditional transistor materials [7].

5.2 Review of previous work on perylene.

5.2.1. Perylene: half a century ago.

The crystal and molecular structure of perylene have been studied since the second half of the last century [8,9]. Those early studies describe perylene molecule as monoclinic with four molecules in a unit cell of dimensions $a=11.35 \text{ \AA}$, $b=10.87 \text{ \AA}$, $c=10.31 \text{ \AA}$, $\beta=100.8^\circ$, Fig. 5.1a. For Donaldson et al. [8] the results did not make it possible to find any projection of the structure, which gives a clear picture of a well-resolved single molecule. Camerman et al. [9] considered perylene as one of the simplest examples of a type of polynuclear aromatic hydrocarbon, which contains formally single bonds. They established that the four perylene molecules in the unit cell are grouped in pairs about centres of symmetry, so that the mean planes of the molecules in each pair are parallel, and the perpendicular distance between the plane is 3.46 \AA . Thus, examination of the intermolecular distances reveals that all the shortest contacts are between molecules related by a centre of symmetry. When the centrosymmetrically related molecules are projected on their own plane it is found that the carbon atoms do not lie directly over one another but are staggered as shown in Fig. 5.1b.

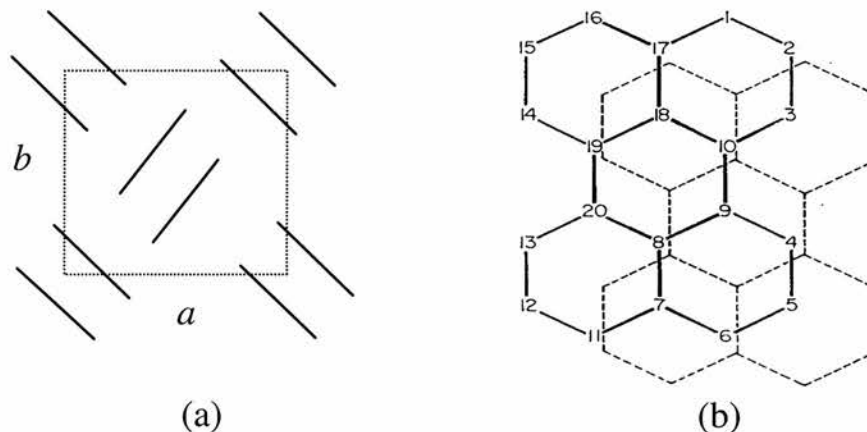


Fig. 5.1 (a) View of the perylene molecules in the unit cell projected on to (100).
 (b) Normal projection of two parallel molecules [8].

5.2.2 Epitaxial growth

Toda and Yanagi [10] found a dependence of the electroluminescent (EL) spectrum on molecular orientation in the organic EL device with a thin film of perylene. They prepared two types of double-layered thin film EL cells, see Fig. 5.2, by vapour deposition with epitaxial or polycrystalline perylene films as an emission layer and *N,N'*-diphenyl-*N,N'*-bis(3-methylphenyl)-[1,1'-biphenyl]-4,4'-diamine TPD as hole transport layer (HTL).

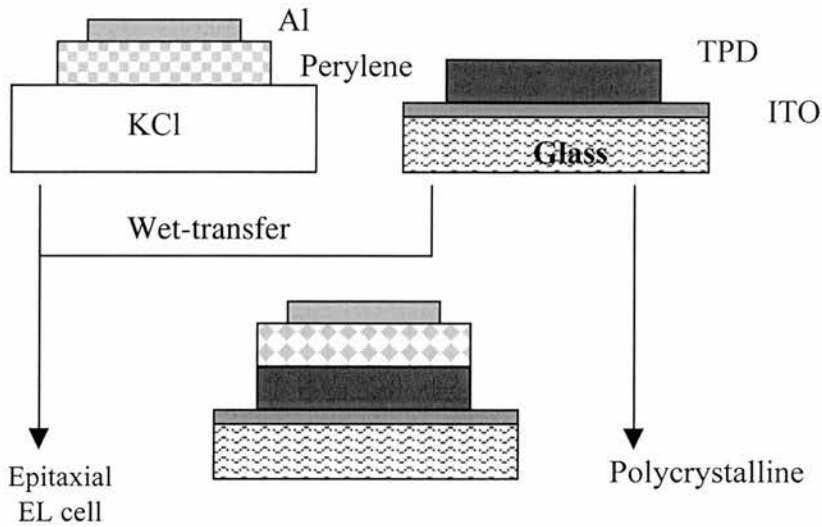


Fig. 5.2 Schematic diagram for EL device [10].

Perylene vapour deposition was used to prepare the epitaxial EL cell. It was deposited onto the (001) cleavage surface of KCl single crystal at room temperature [9]. This process is shown as diagram in Fig. 5.2. The polycrystalline perylene film was composed of particles with about $0.5 \mu\text{m}$ in diameter and its electron diffraction showing a Debye-Scherrer ring pattern, which demonstrated that the randomly oriented crystalline particles were defined as reported α -form crystal of perylene [9]. Atomic force microscopy (AFM) images of both films are shown in Fig. 5.3. The epitaxial perylene film grew in a platelike morphology aligning along the [110] direction of the KCl substrate, as shown in Fig. 5.3a. In addition, the ab -plane of the perylene crystals (see Fig. 5.1a) comes into parallel contact with the KCl (001) surface. An x-ray diffraction pattern taken from this epitaxial film indicated reflection peaks corresponding to the (001) and (002) spacing of the α -form perylene crystal. Therefore,

the longer axis in the molecular plane of perylene orients almost perpendicular to the KCl surface and the crystal grows layer by layer taking the epitaxy of $(001)_{\text{perylene}} \parallel (001)_{\text{KCl}}$, $[100]_{\text{perylene}} \parallel [100]_{\text{KCl}}$.

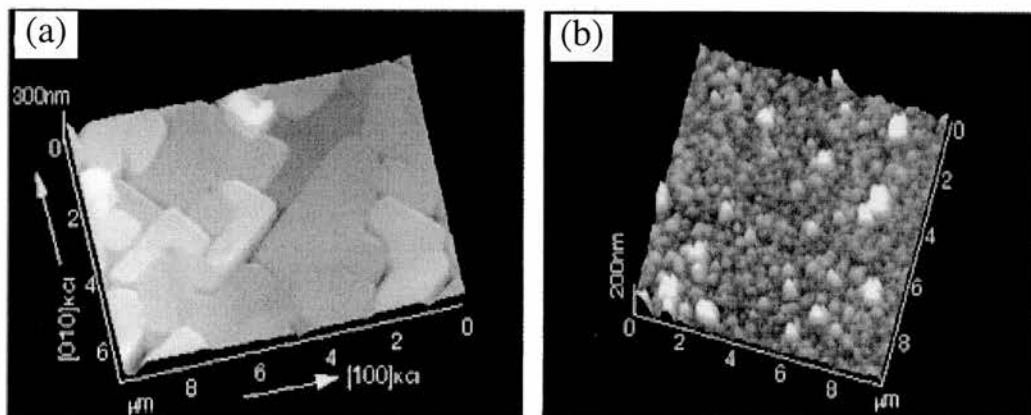


Fig. 5.3 AFM images of epitaxial perylene film ($7 \times 10 \mu\text{m}^2$) vapour deposited on the KCl (001) surface (a) and polycrystalline perylene film ($10 \times 10 \mu\text{m}^2$) vapour deposited on glass substrate (b). Figure taken from Toda et al. [10].

Also, the surface topography taken from the epitaxial crystal reveals a molecular orientation in which upright molecules form dimeric aggregates and packs in a herringbone structure. Finally, their emission colour looked significantly different; bluish–white in the polycrystalline EL cell while yellowish–green in the epitaxial EL cell [10].

Chen et al. [11] have also investigated the epitaxial growth of perylene on $\text{Cu}\{110\}$, with a combination of different techniques, including HREELS, LEED and STM. According to vibrational spectra, the perylene molecular planes are parallel to the

substrate. Electron diffraction indicates an almost square unit cell in the ab plane in which the a axis is commensurate along the $\langle 110 \rangle$ azimuth of the Cu substrate, while the b axis is incommensurate along the $\langle 001 \rangle$ azimuth. STM images show a large scale smooth morphology of the organic crystal indicative of layer-by-layer growth, see Fig. 5.4. This image shows that individual terraces are defined by the overlayer structure rather than the terraces of the clean Cu surface. In fact, the multilayer structure can be well resolved, confirming the layer-by-layer growth mechanism. Also, perylene and pyrene adlayer structures on Cu(111) in HClO_4 were investigated by *in situ* STM [12], where one dimensional ordered molecular arrays along $\langle 110 \rangle$ direction were observed. It was found that the interaction between aromatic molecules and substrate increases with an increase in the number of aromatic rings.

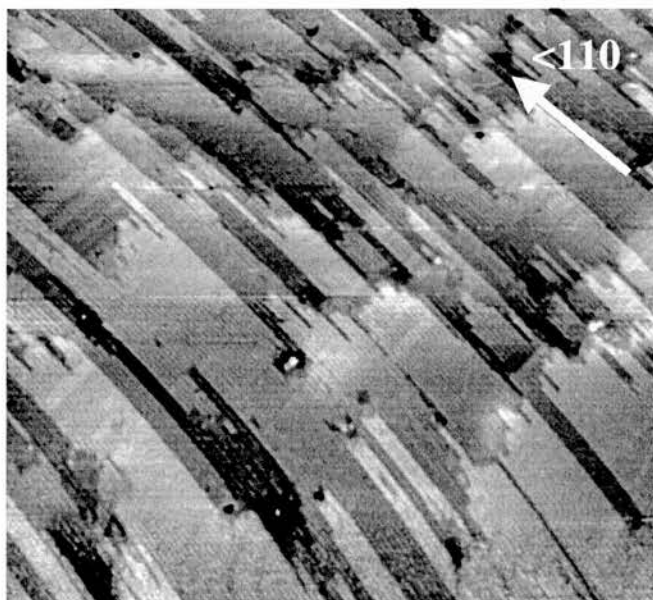


Fig. 5.4 STM image (270 nm x 270 nm) obtained at a sample bias = 0.01 V and a tunnelling current = 0.47 nA [11].

When the molecular orientation within a layer and those in different layers are compared, it is found that molecules on the same line along the $\langle 001 \rangle$ azimuth have the same molecular orientation, even a in different layers [11]. A further enlarged image (Fig. 5.5) shows the molecular details of the ordered structure. In STM, the tunnelling junction is achieved with molecular orbitals that match both the substrate and the tip in energy, space and symmetry. Since the π -orbitals of aromatic molecules are very close to the Fermi level of metals, zero bias is suitable for forming stable tunnelling conditions to resolve the molecular features.

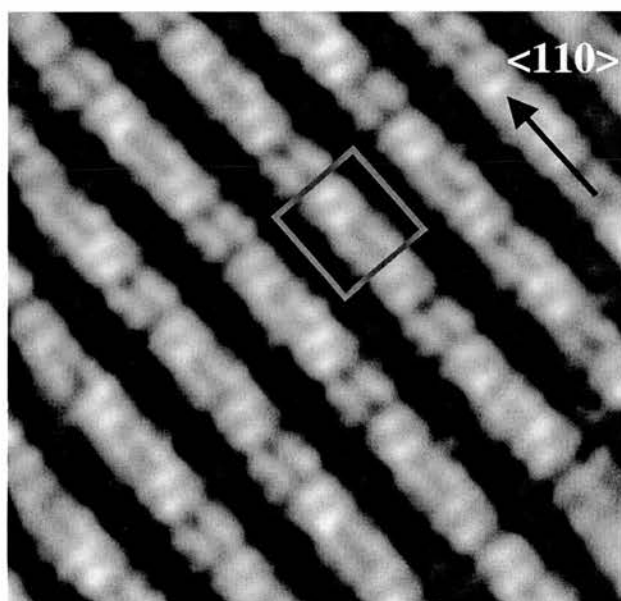


Fig. 5.5 STM images showing (a) the molecular arrangement between different layers and (b) a high resolution terrace with the unit cell (rectangular box) [11].

Vapour phase grown perylene has been used to form single-crystal OFETs by Schon et al. [13] at Bell laboratories. Perylene single crystals were grown in a stream of flowing hydrogen from the vapour phase [14]. Ambipolar charge transport with electron mobilities, $5.5 \text{ cm}^2/\text{V s}$, were observed. Also, the temperature dependence of the electron and hole mobilities in the temperature range from 50 to 300 K was analysed. They found that the mobility increase with decreasing temperature reaching values as high as $120 \text{ cm}^2/\text{V s}$ for electrons at low temperatures. The OFET device presents a strong increase of the drain current I_d at high drain voltages V_d , related to a p-channel (n-channel) formation in the electron (hole) enhancement mode, which have been observed for other ambipolar transistors [15,16].

Until now, there have been no previous studies of perylene adsorption on silicon single crystal surfaces. Therefore, it is of interest to study the adsorption and growth properties of this interesting molecule on both clean and hydrogen-terminated silicon surfaces.

5.2.3 Vibrational studies.

Many vibrational studies have been carried out regarding perylene [11], perylene cation [17,18] and perylene derivatives, including studies in solvents [19]. For perylene infrared (IR) spectrum of the free molecule indicates that the in-plane modes are inherently weaker than the out-of-plane modes [11]. In addition, in the EELS of perylene/Cu(110) [11], the out-of-plane modes are about 40 times stronger than the in-plane modes. Such a high intensity ratio in EELS can be attributed only to the fact that most of the molecules are in a flat-lying geometry relative to the substrate with excitation of in-plane modes forbidden by the surface selection rule.

5.3 HREELS study

High resolution electron energy loss spectroscopy studies have been carried out of perylene on both hydrogen-terminated Si(111) and clean Si(100)-2x1 surfaces. Table 5.1 contains the frequencies and assignments of modes observed in EELS and compared with IR absorption of perylene in KBr and results of a Gaussian 98 calculations of an isolated molecule.

5.3.1 Perylene on clean Si(100)-2x1

Figure 5.6 shows the spectra of perylene adsorption on clean Si(100)-2x1 surface, followed by annealing the sample at different temperatures, ranging from 353 until 400 K. Details of those spectra are as follows. Spectrum of clean silicon before dosing is shown in Fig. 5.6a. After dosing the sample for 15 min (9×10^{-9} mbar), some perylene induced peaks can be distinguished at 776, 940, 1180, 1348, 1582 and 3046 cm^{-1} as well as small features at 436 and 520 cm^{-1} , see spectrum (b). The peak at 3046 cm^{-1} is characteristic of C-H aromatic stretching, which appears with a high intensity. The features at 1348 and 1582 cm^{-1} are related to C-C stretching [20]. The peak located at 776 cm^{-1} corresponds to the C-H out-of-plane bending mode, typical of adsorbed aromatic hydrocarbons. The C-H in-plane bending mode are presented at 940 and 1180 cm^{-1} . According to these descriptions and the observed band intensities, it is reasonable to conclude that the perylene molecules do not lie flat on the reactive surface, instead the molecules seem to adopt a mere vertical orientation. Annealing the sample to 350, 420 and 450 K, spectra (c)-(e), it is noticeable that molecules stay intact on the surface, but now there is a slight presence of Si-H band at 610 and 2090 cm^{-1} , which confirms the relatively strong chemisorption of perylene molecules on Si(100)-2x1 surface. The frequency of the peaks with their assignments is summarized in the table 5.1(below).

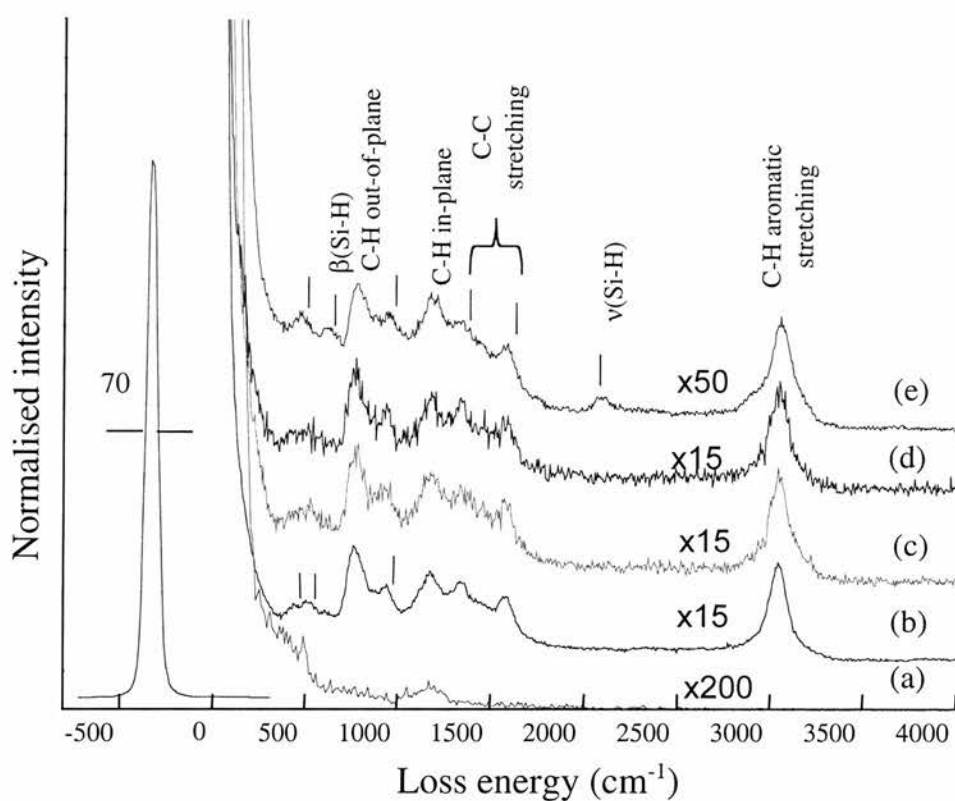


Fig. 5.6 HREEL spectra of clean Si(100)-2x1 (a), and after dosing for 15 min at RT (b). Spectra (c) – (e) after annealing the sample at 350, 420 and 450 K, respectively.

5.3.2 Perylene on H:Si(111)

The hydrogen-terminated Si(111) surface spectrum is shown in Fig. 5.7a with its typical Si-H bending (β) and stretching (ν) modes at 624 and 2080 cm^{-1} , respectively. Dosing the sample at room temperature for 15 min, caused the appearance of small features at 776 and 3050 cm^{-1} , besides the pre-existing Si-H peaks, Fig. 5.7b. Increasing the exposure leads to increase in the intensity peaks at 776 and 3048 cm^{-1} , which are attributed to C-H out-of-plane bending and C-H aromatic stretching modes,

respectively (spectrum c). Further dosage of perylene, for about 30 min (4×10^{-9} mbar), cause the appearance of more intense and sharper peaks at 760, 1188, 1352, 1580 and 3048 cm^{-1} , as well as smaller peaks at 440, 524, 880 and 944 cm^{-1} , vibrational spectrum (d). Description of those peaks are similar to the previous perylene adsorption on Si(100)-2x1. A difference between the surfaces is that the peak located at 760 cm^{-1} has higher intensity compared with the other peaks in the case of H:Si(111). This important feature suggests a more random orientation of the perylene molecule on this passivated surface. It is important to point out that a high dosage was necessary in order to achieve enough coverage of perylene to be sensitive to the HREELS technique. In table 5.1 are detailed those peaks from a high perylene exposure on hydrogen-terminated Si(111).

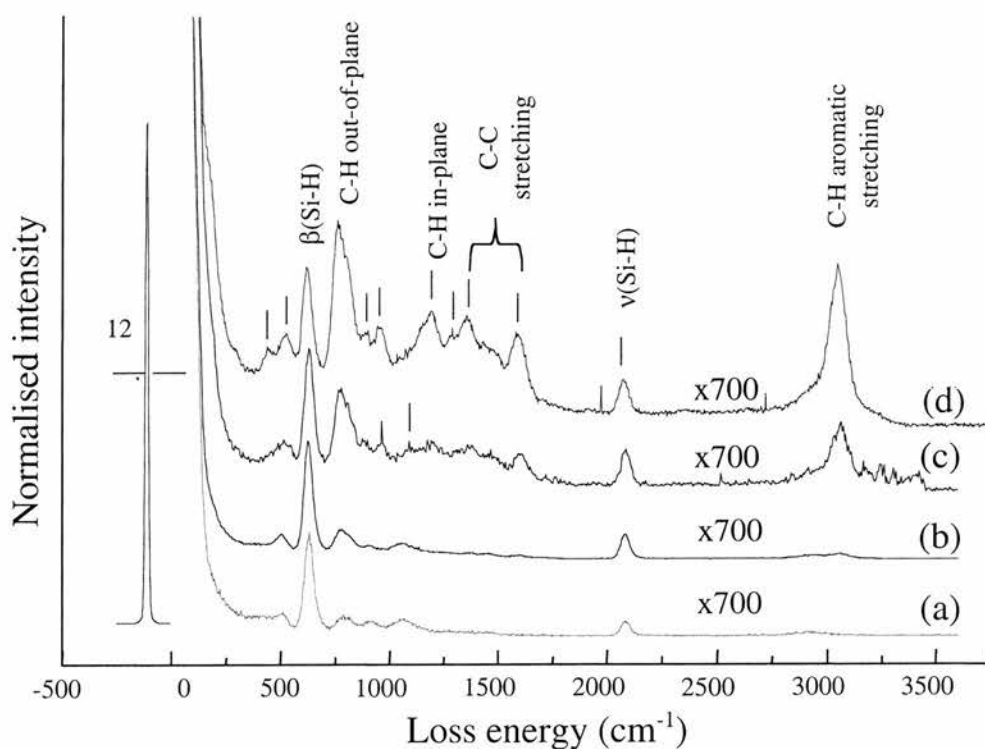


Fig. 5.7 Vibrational spectra of (a) H:Si(111), b) after dosing with perylene for 15 min, c) further dosage 20min and d) after dosing for 30min with doser temperature at 500K.

Infrared spectra of perylene, both experimental in KBr [21] and calculated, for an isolated molecule using Gaussian 98 [22] are presented, in Fig. 5.8. Those spectra show basically an excellent agreement with EEL spectra of perylene on both Si(100) and Si(111) surfaces. Some similarities have been found on such surfaces and are concerned to a random molecular orientation rather than crystal or well ordered orientation growth at high coverage. However, a key feature was found in silicon (100) surface regarding its chemisorption after annealing the surface.

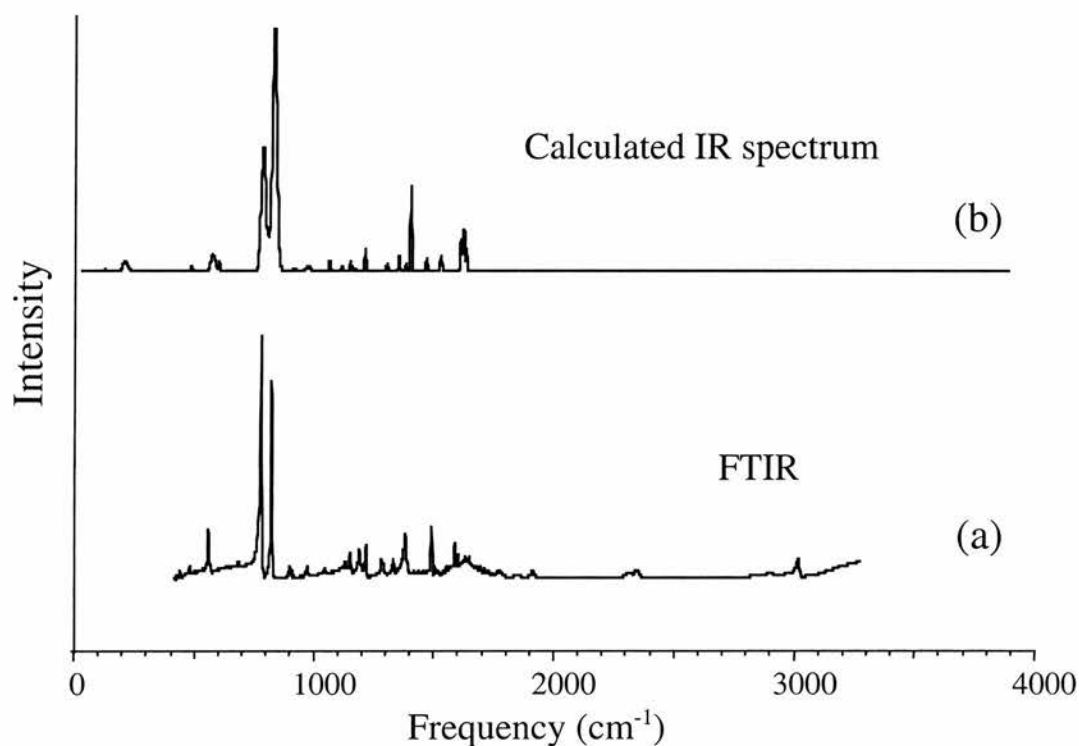


Fig. 5.8 Infrared spectra of perylene (a) experimental in KBr and (b) calculated using Gaussian 98

Table 5.1 The frequencies (cm^{-1}) of perylene in different conditions, including absorption on silicon surfaces. Calculated frequencies (unscaled) obtained using Gaussian 98 on an isolated perylene molecule.

IR Calc.	IR Exper.	Si(100)	H:Si(111)	Assignment
469	462	436	440	C–C–C out-of-plane
	571	520	524	C–C–C out-of-plane
		610	620	Si–H bend.
782	734	776	776	C–H out-of-plane
	809			
830	861		888	C–H out-of-plane
917	939	940	944	C–H in-plane
	1025			
1162	1122			
1178	1151	1180	1188	C–H in-plane
1225	1236			
1319	1302	1348	1352	C–C stretch
1371	1407			
	1507			
1552	1595	1582	1580	C–C stretch
1639				
1650				
		2072	2080	Si–H stretch
3182	3120	3046	3048	C–H aromatic stretch
3200	3135			

5.4 STM

5.4.1 Clean Si(100)-2x1.

A high resolution STM image of perylene adsorbed at room temperature on Si(100)-2x1 is shown in Fig. 5.9. In this STM image, obtained at low coverage, perylene molecules appear as bright features and forming molecular “chains” aligned perpendicular to the silicon dimer rows. These chains are clearly observed on different terraces and always perpendicular to Si dimer rows. Also, five-molecule groups are seen to form blocks in the chain, where some molecules are brighter than other in the same block and there are always a weak feature in the middle of these blocks. The intensity variation is the same in each group.

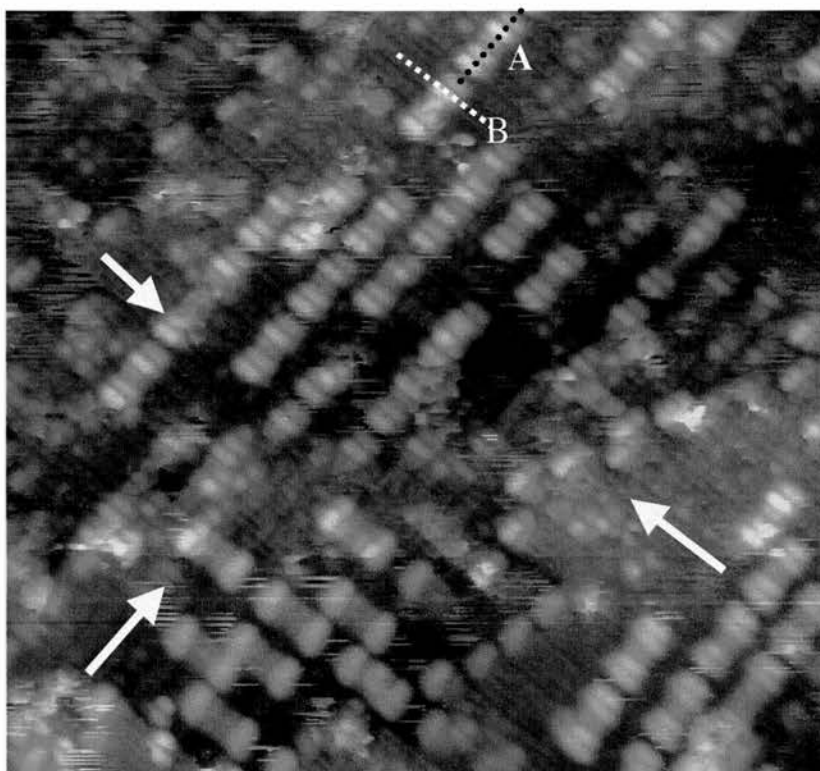


Fig. 5.9 STM image (30 nm x 30 nm) of perylene on Si(100)-2x1 at low coverage (-2.225 V and 0.065 nA). Chains of perylene molecules are seen perpendicular

to dimer rows (arrows) in different terraces. Dash lines labelled as A and B represent the site along which the line profiles were taken (See Fig. 5.14).

Further enlargement of the STM image (Fig. 5.10) and the line profile, across this five-molecule block, reveals clearly that perylene adsorbs with the longer molecular axis parallel to the dimer rows, [011] direction. The length of this brightest feature, in the five-molecule block, measured along [011] direction is 11.35 Å, which is similar to the Van der Waals length of perylene along the longer axis, 11.25 Å. The shorter molecular axis seems to be perpendicular to the silicon surface, but a small tilting angle can not be ruled out, this part will be discussed further. This upright configuration is consistent with the vibrational EELS data, which indicated high intensity for the C–C and C–H in-plane modes. Also, individual perylene molecules are aligned along Si dimer rows direction, but stacking next each other to form blocks in a chain-like structure perpendicular to the Si dimer rows. The questions why those chains are divided in small five-molecule blocks and why the molecules chemisorb upright on Si(100) instead of a flat-lying configuration, like benzene, pentacene or tetracene for instance, remain unsolved yet.

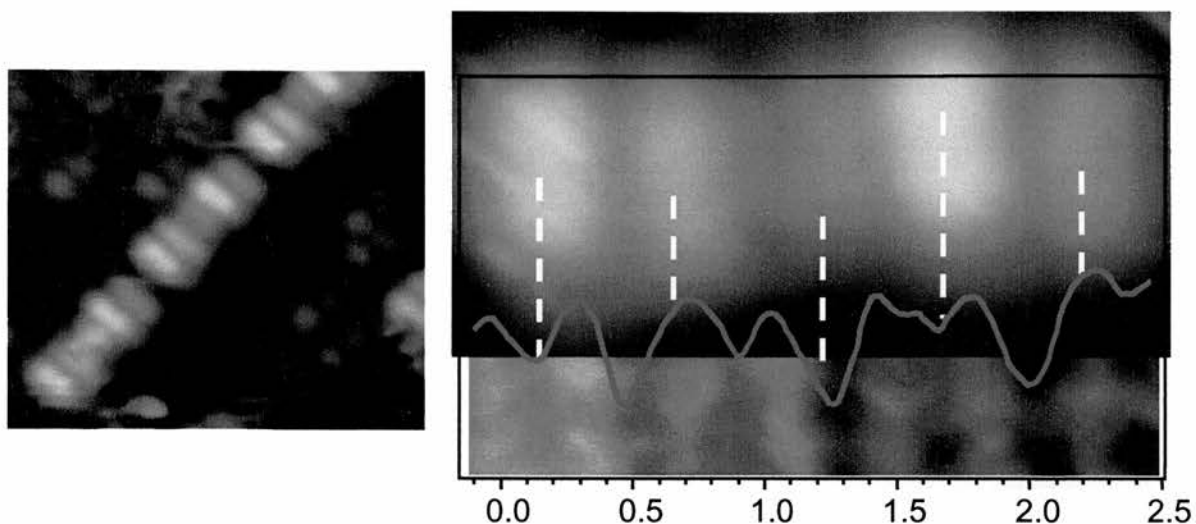


Fig. 5.10 Small area of STM image reveals perylene molecules attach with the longer molecular axis parallel to the surface (left). Registry of perylene with Si(100)-2x1 shows that the brighter features in the perylene chains corresponds to on-top of the dimer position (right).

However, registry of perylene with Si(100) dimers is also shown in Fig. 5.10. It is unambiguously found that brighter features are located on top of the dimers, making a combined contribution, between silicon atoms and perylene molecule, to the tunnelling current. Meanwhile, the weakest feature in the middle of these blocks is located in the inter-dimer rows site, where a silicon contribution to the tunnelling current is lower.

STM studies of perylene at higher coverage on Si(100)-2x1 reveal that multilayers of perylene are formed, as seen in Fig. 5.11. This STM image shows rows of small clusters of perylene with size range between 4-8 nm mainly. Those rows seem to follow, somehow, the silicon dimer pattern, therefore it is possible to see a preferential orientation of those small clusters rows. Since the underlying dimer structure is not observed, it is not possible to confirm whether the cluster rows lie parallel or perpendicular to the silicon dimer rows.

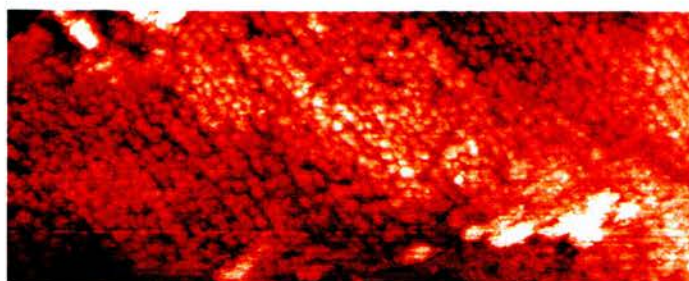


Fig. 5.11 STM image (400 nm x 150 nm) of multilayers of perylene on Si(100)-2x1 (2.3 V; 0.238 nA).

5.4.2 Hydrogen-terminated Si(111)

The room temperature deposition of perylene on hydrogen-passivated Si(111) was followed by STM. Fig. 5.12 shows STM images at different coverage, including submonolayer and multilayers regime. A low coverage image (a) obtained after perylene dosing for 5 min at 8×10^{-10} mbar pressure shows some small clusters spread over the surface. The size of these cluster range between 2.5 to 3.5 nm and the height of them are around 12 Å, as can be noticed from the line profile. Also, some terraces and surface defects created during the etching procedure are seen, but evidence of isolated molecules was not found at this coverage. Further increase of the dosing time, 10 min, led to full coverage of the surface with molecular clusters, Fig. 5.12b. In addition, the clusters size is also increased, as shown in the line profile for this image. The third STM image (c), at large scale, was obtained after additional dosing for 10 min. There, the appearance of clusters is the dominant characteristic and the size of these clusters remains small, in addition evidence of large island or any ordered structure was not

found, even at high exposure of perylene. The line profile did not show dramatic change in either the clusters size or their height.

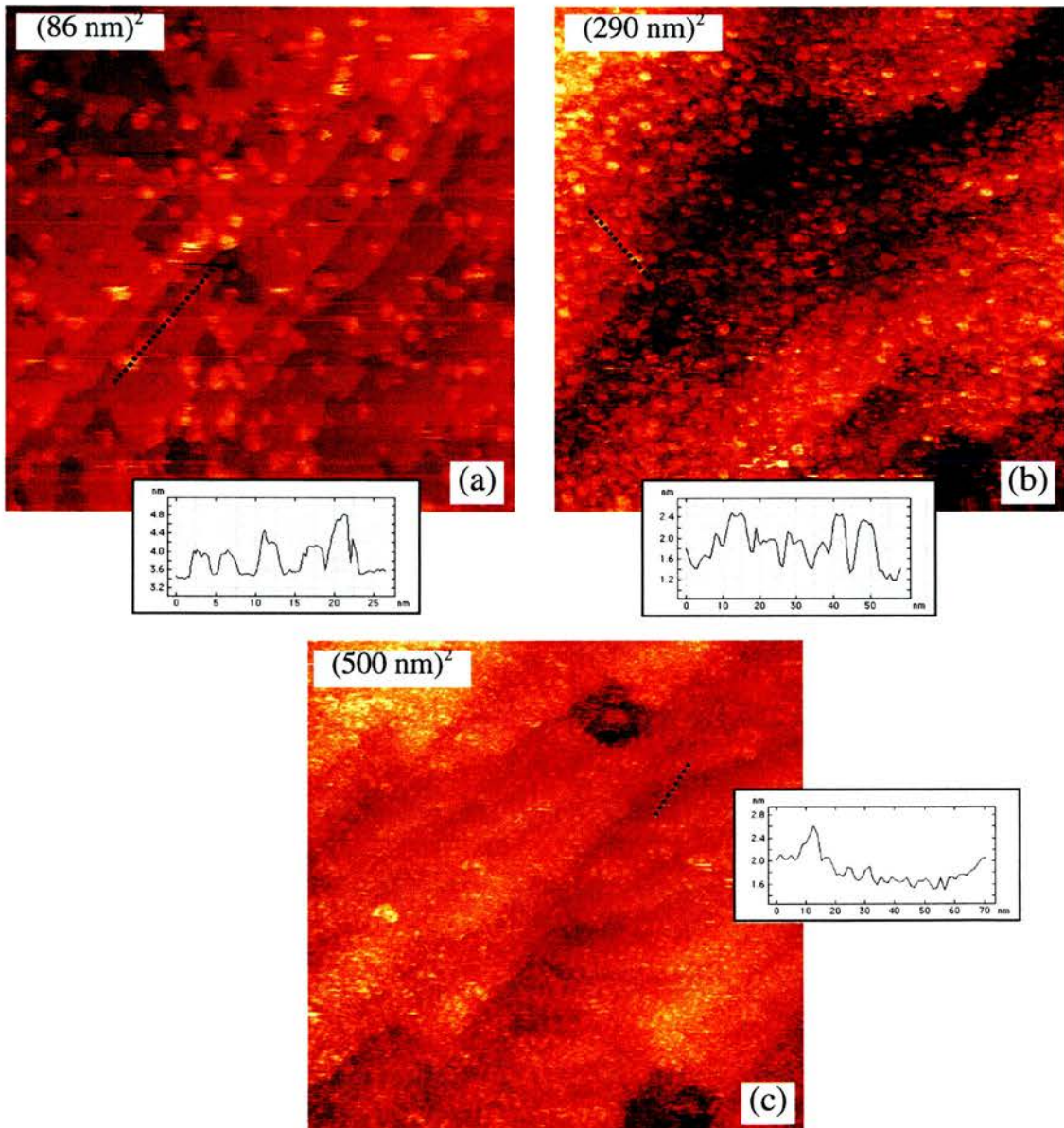


Fig. 5.12 STM images of perylene adsorption on hydrogen-terminated Si(111) at different coverage. (a) Low coverage image (2.73 V; 0.07 nA) in the submonolayer regime, (b) monolayer coverage (1.97 V; 0.07 nA) and (c) multilayers coverage. Line profiles of each image are inset.

5.5 Calculation

Ab initio calculations on a fully optimized free molecule were carried out with the B3LYP density functional and the 6-31G basis set using GAUSSIAN 98. The IR spectrum obtained from these calculations is shown on Fig. 5.8, and the charge density distributions associated with the highest occupied molecular orbital (HOMO) and the lowest unoccupied molecular orbital (LUMO) are shown in Fig. 5.13.

From the charge density distribution for both HOMO and LUMO, which are relevant to the STM images in the molecule, it is found that the molecule has a nodal plane bisecting each of the two naphthalenes and dividing the perylene into two biphenyl units.

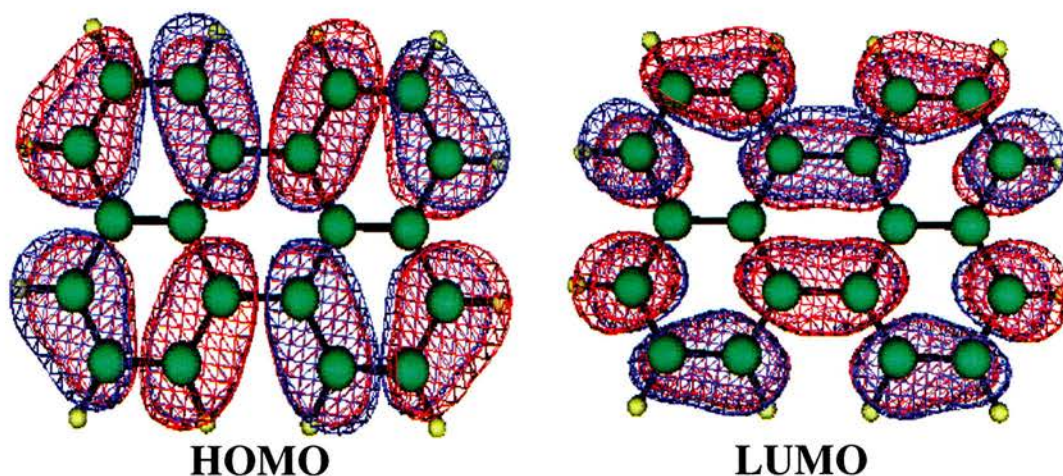


Fig. 5.13. The charge density distribution of the HOMO and LUMO.

5.6 Discussion

STM results of perylene adsorption on clean Si(100)-2x1 show that at low coverage, submonolayer, chains of perylene are seen, Fig. 5.9. The chains are located perpendicular to the silicon dimer rows with perylene molecules, forming five-molecule groups, in an upright configuration. Measurements of the brightest feature in both line profiles A and B, Fig. 5.14, suggest that perylene molecule adsorbs upright with the shortest molecular axis either perpendicular to the silicon substrate or tilted a small angle, the [001] direction. Taking the width over length ratio ($W/L= 1/3$), the tilting angle estimated is less than 15° with respect to the normal.

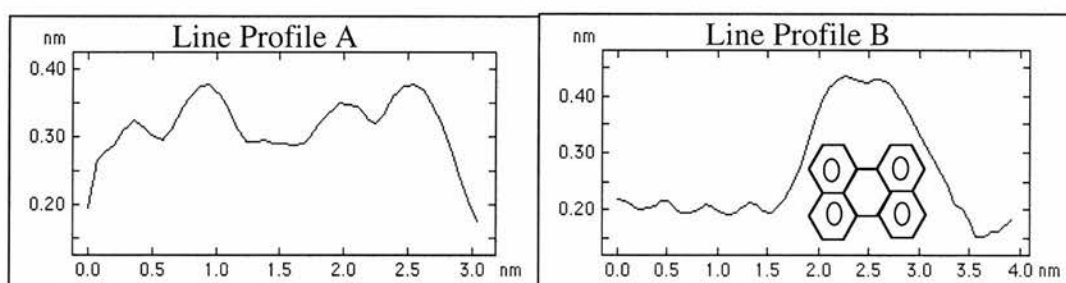


Fig. 5.14 Show the line profile for A and B, as labelled in a previous STM image (figure 5.9).

Figure 5.15 presents a scheme for the proposed adsorption according to the STM images obtained for low coverage. In this scheme five perylene molecules are located in four dimer rows, according to Fig. 5.10, with the first and fourth molecules from the left, located on top of the silicon dimer row corresponding to the brightest feature. The perylene molecules are tilted 15° to the left but it is also possible to be considered tilted

to the right or even complete vertical. The second and fifth molecules are located on top of one silicon atom per dimer. The molecule in the middle of the group, which appears as the weakest feature in the STM images, is located in the inter-dimer site. However, from these images is not possible to conclude how perylene molecules are attached to the silicon surfaces in greater detail. Therefore, the bonding mechanism between perylene and silicon atoms needs to be analysed in more details. In particular, more information is required on the precise location of surface silicon atoms relative to the perylene.

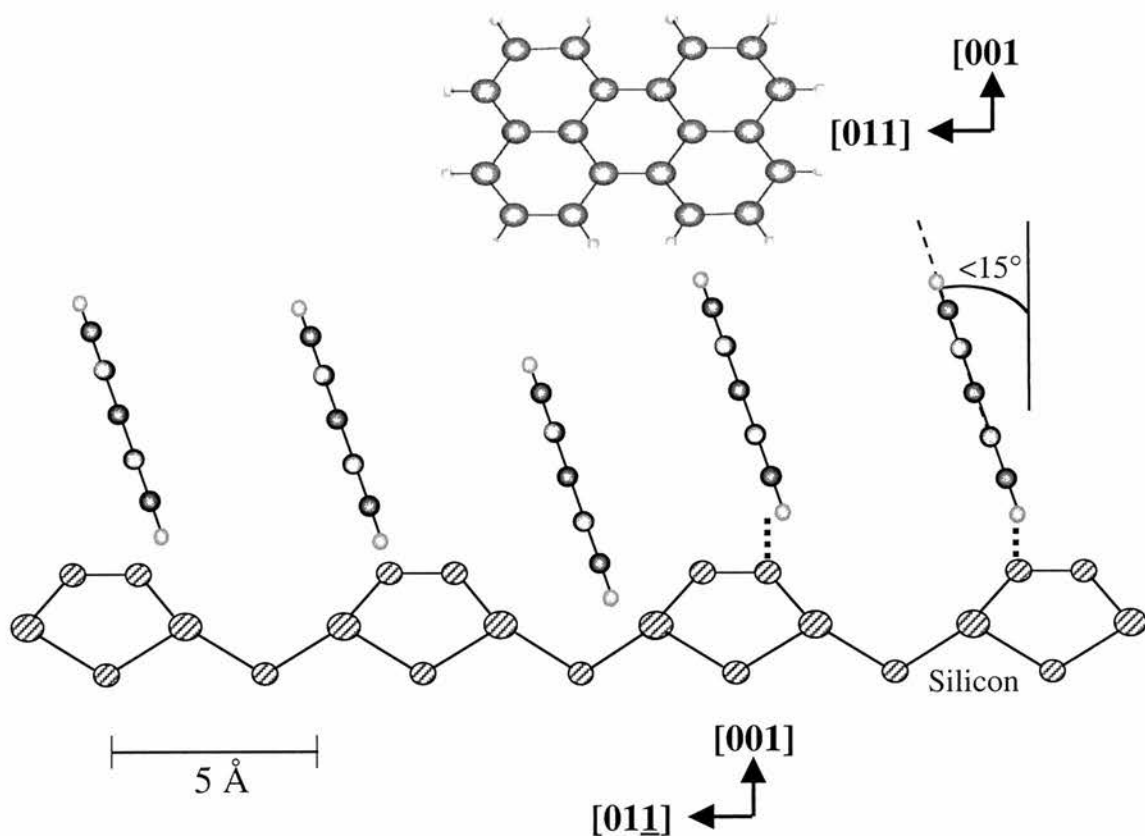


Fig. 5.15 A perylene molecule with the longer axis aligned along [011] direction in an upright configuration (above). Scheme of a five-molecule group

distributed over four silicon dimer rows (bottom). The molecules are tilted to the left but is also possible to be vertical or tilted to the right.

At the moment, it is relatively clear the way that perylene attaches (approach) to the surface with the biphenyl unit close to the silicon atoms. Thus, it is reasonable to deduce that the carbon atoms 5 and 8, Fig. 5.16, are involved in the bonding process. Therefore, two options can be considered which are a direct Si-C bond, replacing the hydrogen bond, and the rehybridization of carbons atoms from sp^2 to sp^3 . The latter seems unlikely for a vertical adsorption or with a small tilted angle, which are the cases achieved for perylene on clean silicon, but also involve more energy exchange. The former is more probably because it implies a simple reaction without changes in the aromatic properties for the benzene rings in the perylene molecule, therefore Si-C, via C-H bond cleavage, and Si-H bonds are formed. Unfortunately, the vibrational spectrum for such low coverage could not be achieved and for higher coverage there are other stronger contributions that can dominate the Si-C modes.

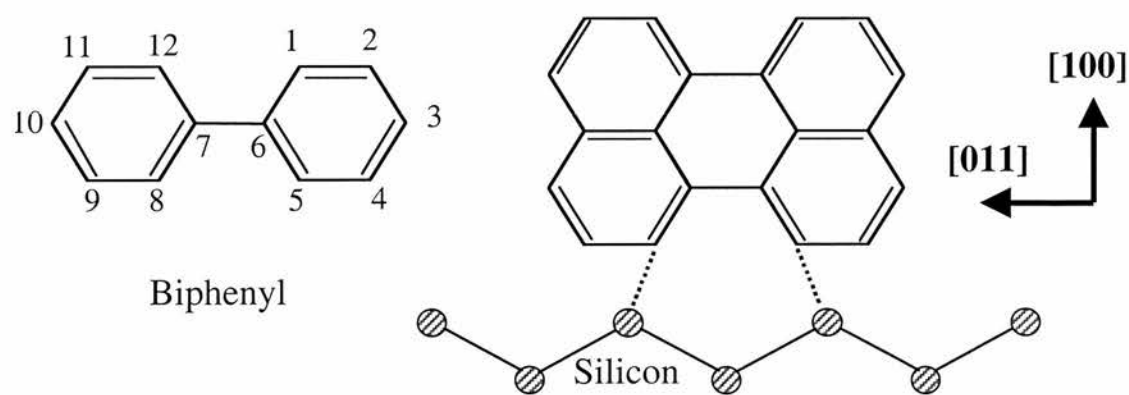


Fig. 5.16 Scheme of a biphenyl molecule (left) and perylene molecule on silicon with the carbon atoms involved in a possible bonding mechanism (right).

The relatively upright orientation of perylene on Si(100) compared to benzene and other polyaromatic species such as tetracene and pentacene is a key feature of this adsorption system. It is significant that the bonding orientation suggests that adsorption occurs across the biphenyl unit through the carbon atoms 5 and 8. This carbon atom configuration is not present in the linear polyaromatics, or benzene itself. Although the adsorption site excludes bonds of the next perylene molecule in the five-molecule group to the silicon atoms in the same dimer, those on the next dimer across (along [011]) are readily available as long as the molecules are relatively upright. The limitation to five molecules in the chain is presumably related to the strain introduced into the system perhaps as a result of distortion to the silicon dimer structure needed to accommodate the perylene molecules.

For perylene adsorption on passivated Si(111), STM images show that perylene form small aggregates independent of the coverage. This feature is due to weak interaction between both molecule–molecule and molecule–substrate, which cause a random orientation with a low cluster mobility. The small clusters are usually less than 10 nm diameter, forming a polycrystalline thin film, which was expected from the vibrational results on HREELS.

5.7 Conclusions

The room temperature adsorption of perylene molecule on both clean S(100)-2x1 and hydrogen–terminated Si(111) has been investigated. At high coverage, perylene forms a polycrystalline thin film, according to STM and HREELS studies, on both surfaces. High resolution STM images have shown, at lower coverage, that perylene molecules adsorb upright on Si(100)-2x1, with the short molecular axis either

perpendicular to the silicon surface or tilted a small angle, less than 15°. In this stage, perylene stack in a five-molecule group forming chains perpendicular to silicon dimer rows.

References

- 1 C. W. Tang, S. A. VanSlyke, *Appl. Phys. Lett.* **51**, 913 (1987).
- 2 C. Adachi, S. Tokito, T. Tsutsui, S. Saito, *Jpn. J. Appl. Phys. 1* **27**, L269 (1988).
- 3 C. Adachi, S. Tokito, T. Tsutsui, S. Saito, *Jpn. J. Appl. Phys. 1* **27**, L713 (1988).
- 4 H. Yanagi, M. Ashida, Y. Harima, Y. Yamashita, *Chem. Lett.* **1990**, 385 (1990).
- 5 S. Hayashi, H. Yanagi, M. Ashida, *Mol. Cryst. Liq. Cryst.* **218**, 135 (1992).
- 6 H. Yanagi, S. Douko, Y. Ueda, M. Ashida, D. Wohrle, *J. Phys. Chem.* **96**, 1366 (1992).
- 7 A. Dodabalapur, Z. Bao, A. Makhija, J. G. Laquindanum, V. R. Raju, Y. Feng, H. E. Katz, J. Roger, *Appl. Phys. Lett.* **73**, 142 (1998); T. N. Jackson, Y. Y. Lin, D. J. Glundlach, H. Klauk, *IEEE J. Sel. Top. Quantum Electron.* **4**, 100 (1998); C. D. Dimitrakopoulos, D. J. Masearo *IBM J. R&D.* **45**, 11 (2001).
- 8 D. M. Donaldson, J. M. Robertson, J. G. White, *Pro. Roy. Soc.* **220**, 311 (1953).
- 9 A. Camerman, J. Trotter, *Pro. Roy. Soc.* **279**, 129 (1963).
- 10 Y. Toda, H. Yanagi, *Appl. Phys. Lett.* **69**, 2315 (1996).
- 11 Q. Chen, T. Rada, A. MacDowall, N. V. Richardson, *Chem. Mat.* **14**, 743 (2002).
- 12 D. Wang, L.-J. Wan, Q.M. Xu, Ch. Wang, C.-L. Bai, *Surf. Sci. Lett.* **478**, L320 (2001).
- 13 J. H. Schon, Ch. Kloc, B. Batlogg, *Appl. Phys. Lett.* **77**, 3776 (2000).
- 14 Ch. Kloc, P. G. Simpkins, T. Siegrist, R. A. Laudise, *J. Cryst. Growth* **182**, 416 (1997).

-
- 15 G. W. Neudeck, H. F. Bare, K. Y. Chung, *IEEE Trans. Electron Devices* ED-**34**, 344 (1987).
- 16 A. Dodabalapur, H. E. Katz, L. Torsi, R. C. Haddon, *Science* **269**, 1560 (1995).
- 17 See for example: J. Szczepanski, M. Vala, *Apj*, **414**, 646 (1993); L. J. Allamandola, A. G. G. M. Tielens, J. R. Barker, *Apj*, **290**, L25 (1985).
- 18) H. Torii, Y. Ueno, A. Sakamoto, M. Tasumi, *J. Phys. Chem. A* **103**, 5557 (1999).
19. S. N. Goldie, G. J. Blanchard, *J. Phys. Chem. A* **105**, 6785 (2001).
- 20 J. Szczepanski, M. Vala, *The Astrophysical J.* **414**, 646 (1993).
- 21 A. McDowall, private communication.
- 22 Gaussian 98 Revision A.7, M. J. Frisch, G. W. Trucks, H. B. Schlegel, G. E. Scuseria, M. A. Robb, J. R. Cheeseman, V. G. Zakrzewski, J. A. Montgomery, Jr., R. E. Stratmann, J. C. Burant, S. Dapprich, J. M. Millam, A. D. Daniels, K. N. Kudin, M. C. Strain, O. Farkas, J. Tomasi, V. Barone, M. Cossi, R. Cammi, B. Mennucci, C. Pomelli, C. Adamo, S. Clifford, J. Ochterski, G. A. Petersson, P. Y. Ayala, Q. Cui, K. Morokuma, D. K. Malick, A. D. Rabuck, K. Raghavachari, J. B. Foresman, J. Cioslowski, J. V. Ortiz, A. G. Baboul, B. B. Stefanov, G. Liu, A. Liashenko, P. Piskorz, I. Komaromi, R. Gomperts, R. L. Martin, D. J. Fox, T. Keith, M. A. Al-Laham, C. Y. Peng, A. Nanayakkara, C. Gonzalez, M. Challacombe, P. M. W. Gill, B. Johnson, W. Chen, M. W. Wong, J. L. Andres, C. Gonzalez, M. Head-Gordon, E. S. Replogle, and J. A. Pople, Gaussian, Inc., Pittsburgh PA, 1998.

CHAPTER 6

Diffusion Limited Growth of PTCDA Crystals on H:Si(111) Surface

6.1 Introduction

The possibility of including organic semiconductors as the active component in various devices, such as, the light-emitting diodes, transistors and optical switches, has increased the interest in these materials during the last decade [1,2,3]. Such organic devices certainly have the advantages of cheap processing, tunability and flexibility. However, it has also been realized for some time, that the electronic conductivity of these organic materials may restrict the development of commercial devices with long lifetime and low power consumption [4]. The low conductivity or the mobility of the charge carrier is directly related to the quality of the organic thin film, in other words, the density of impurities and particularly of structural defects. Only recently, it has been suggested the use of high quality organic single crystals provides the possibility to increase the conductivity or the mobility of the charge carriers substantially [2,5].

For the development of commercial devices, efforts have been focused on controlling the structures of ordered thin films of the organic semiconductors, using molecular beam methods [6,7,8]. The methods can be identified either as Organic Molecular Beam Deposition (OMBD) or Organic Molecular Beam Epitaxy (OMBE): The distinction between the two depends on whether the substrate plays a chemical

role in influencing the overlayer structure, to the extent that the overlayer is commensurate with the substrate or not. The detailed discussion on these two growth modes has been published elsewhere [9].

Most of the work that has made the greatest impact to date has concentrated on the study of the growth and optoelectronic characteristics of planar stacking molecules such as polycyclic aromatic compounds based on perylene. In particular, a molecular system based on 3,4,9,10-perylene tetracarboxylic dianhydride (PTCDA) has been world widely studied focusing on the fundamental interactions on a variety of substrates, *vide infra*, to better understand the factors that may affect molecular ordering [10,11,12]. Applications of this polyaromatic molecule have been found in some optoelectronic devices for instance in a organic light emitting device (OLED) [2,13] and stacked organic light emitting device (SOLED) [14], see Fig. 6.1 and 6.2, respectively.

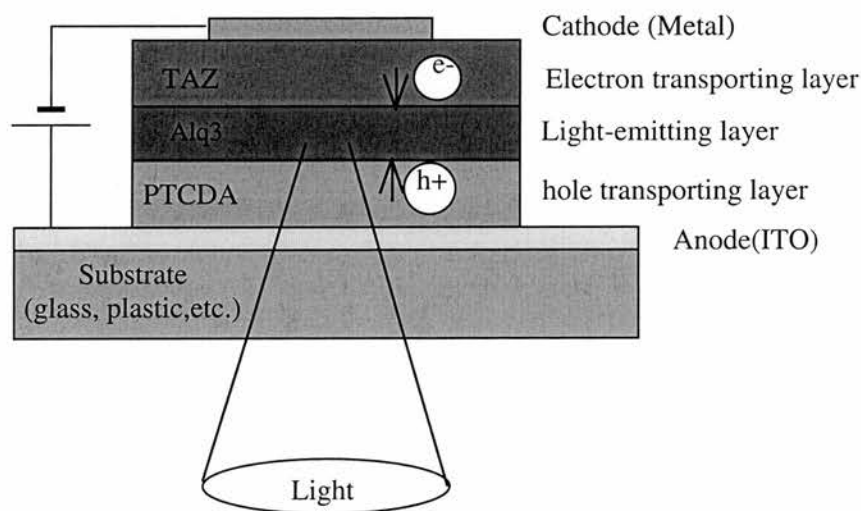


Fig. 6.1 Conventional organic light emitting device double heterostructure showing the contacts, the electron transport layer (ETL), light emitting layer

(EL), hole transport layer (HTL) and the active element for each layer, including TAZ, Alq₃ and PTCDA [6].

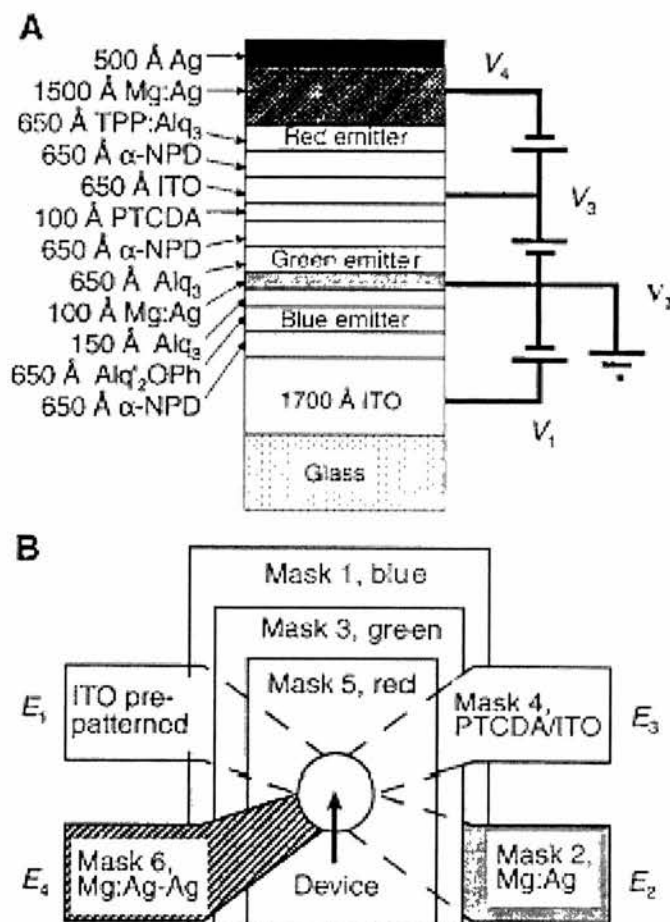


Fig. 6.2 (A) Schematic view of a three-colour stacked organic light emitting device (SOLED) showing the various material layers and the biasing scheme. The total thickness of the contacts and organic layers is $\sim 0.8 \mu\text{m}$. (B) Top view of a SOLED device. Figure taken from Shen et al. [14].

The particular interest in this molecule as described by Ostrick et al. [13] is that PTCDA transports electrons in the direction parallel to the molecular planes and mainly

holes in the direction perpendicular to the molecular planes. Zang et al. [15] have also documented the huge anisotropies in the optical and dielectric properties of PTCDA along different crystal directions. Additionally, PTCDA has been shown to be a very good optical waveguide material, possessing a large refractive index (2.0) and low optical loss at near-infrared wavelengths along the molecular planes [16]. Recently, Hudej and Bratina have found evidence of bipolar charge transport in PTCDA through transient photocurrent measurements [17]. Their results showed that both holes and electrons are transported in the direction perpendicular to the molecular layers. Also, charge transport is strongly dependent on the electric field.

6.2 Relevant work on PTCDA: a brief review

For molecules containing functional groups, such as the anhydride groups in 3,4,9,10-perylene tetracarboxylic dianhydride molecule, the intermolecular potential energy surfaces become much deeper and narrower than their unfunctionalised analogues. This tends to ensure the multilayer structure is same as the thermodynamically stable bulk structure(s) [18,19,20] which, of course, is then most likely incommensurate with the inactive substrates. In that respect, Hirose et al. [21] have pointed out that interactions between this organic molecule and passivated substrates, such as Se-passivated GaAs and graphite, results in non-epitaxial growth of PTCDA films with good crystallinity. Crystalline order is achieved due to intramolecular Van Der Waals force, H bonding and quadrupole interaction.

Thin PTCDA films have been studied on different substrate, such as HOPG [21,22], Au(111) [23], Au(100) [24], Ag(111) [25,26], Ag(110) [25,27], Ag(100)

[28], Cu(110) [29], InSb (111) and InAs(111) [30]. It has been found that PTCDA forms well-ordered monolayers. In most cases, the PTCDA grows in a herringbone fashion, reflecting a small distortion (a few per cent) of the (102) bulk plane with two flat-lying molecules per unit cell with p2gg symmetry. So far only two other formations of PTCDA are known. On Ag(110) the molecules form a “brickwall” structure [27] and on Au(111) [23] a quadratic one. In both cases, the substrate plays a crucial role in determining the superstructure, through substrate reconstruction and strong bonding to the PTCDA molecule. Fig. 6.3 shows PTCDA molecules in two different adsorption structures [26].

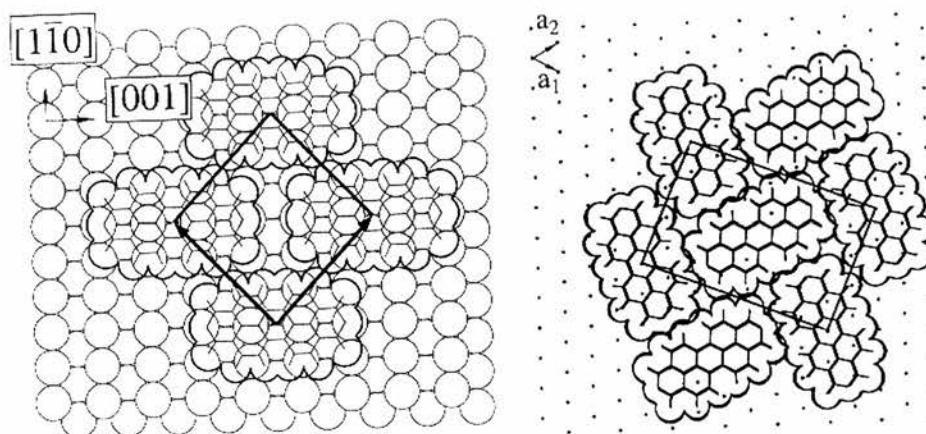


Fig. 6.3 Structural models of PTCDA submonolayers on Ag(110) (“brickwall”, left) and Ag(111) (“herringbone”, right). Unit cells are indicated [26].

Hydrogen terminated Si(111) obtained through wet chemical procedure is one of the most stable and smooth surfaces [31]. Therefore, it is a suitable candidate for studies of organic crystal growth. Previous low energy electron diffraction (LEED)

intensity, Raman peak shape and AFM studies have shown some evidence of PTCDA clusters formed on H:Si(111) surfaces [12,32], while a scanning tunnelling microscopy (STM) study suggested an almost completely covered surface[33]. These apparently contradictory results may be related to different growth modes.

OMBD deposition of PTCDA on alkali halide single crystal surfaces has shown the formation of dendritic crystals [18,19]. X-ray [18] and electron diffraction [19] have been used to study the 3D structures of the both α and β phases of PTCDA on alkali-halide crystal substrates. It has also been suggested that the (102) basal plane of the PTCDA crystals are aligned parallel to the substrate. The structures of this (102) plane in the α and β phases are shown in Fig. 6.4a and 6.4b respectively. The angle between the longer molecular axes of the two molecules within the unit cell is different for the two phases: 96° for the α phase and 104° for the β phase. Of course, diffraction techniques are not sensitive to the details of defects, domain boundaries, steps and shape of the crystals. Although AFM [34] and TEM [18] studies have revealed some of the shape and size properties of PTCDA crystals, until now there has been neither a study of molecular resolution in real space to demonstrate the molecular arrangement within that (102) basal plane of the PTCDA crystal nor how the macroscopic crystal morphology is determined by the intermolecular interactions within that unit cell.

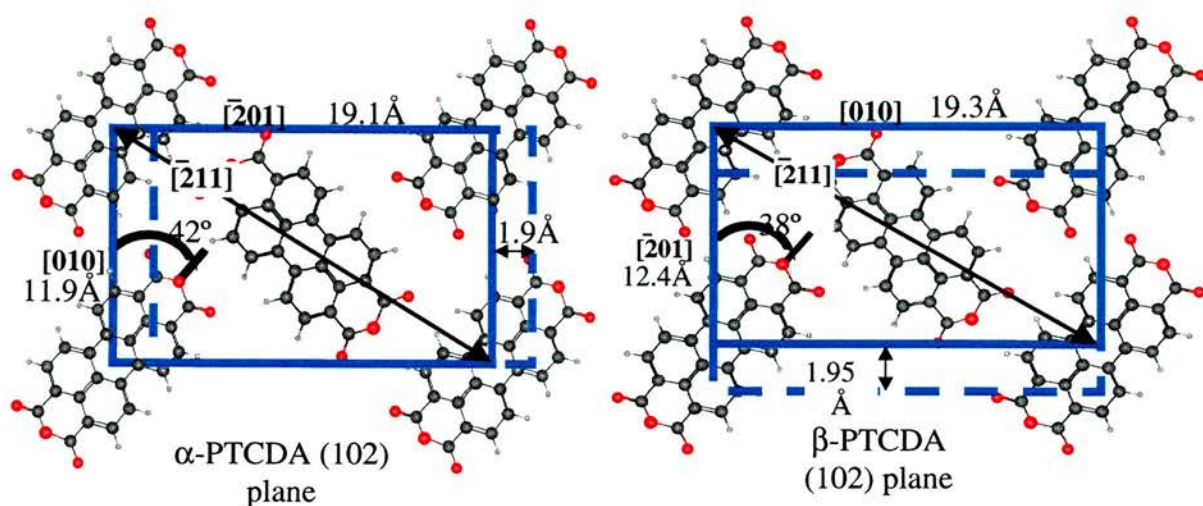


Fig. 6.4 Structures of α phase (a) and β phase (b) of bulk PTCDA crystals.

The dashed lines indicate the shift of the second layer unit cell.

6.3 Vibrational study.

Prior to dosing the PTCDA, the H:Si(111) sample is isolated in chamber to maintain the cleanliness of the surface, while the doser is gradually heated to 200°C and maintained at that temperature for 30min. The PTCDA is then dosed at a temperature between 200 and 250°C with a dosing pressure about 5×10^{-10} mbar, while the sample was kept at room temperature. All spectra were recorded at room temperature. Vibrational studies of PTCDA adsorption on hydrogen-terminated Si(111) were carried out, see Fig. 6.5. HREEL spectrum (a) taken after dosing 1.5L, which corresponds to multilayer coverage, reveals several loss features of PTCDA in the range from 380 to 1800 cm^{-1} . The first peak in this range, at 380 cm^{-1} , and its shoulder at 440 cm^{-1} can be assigned to C–C=O and C–O–C bending vibrations modes in the anhydride group [25]. High coverage is confirmed by the intensity of the peaks in the range between 700 and

900 cm^{-1} , according to Tautz et al. [25] and the spectrum is dominated by the peak at 780 cm^{-1} with two shoulders at 810 and 860 cm^{-1} , corresponding to C–C “ripple” (as labelled by Tautz in Ref. 25) the first two peaks and HC–CH “wagging” to the last peak. The principal C–O–C stretch vibration occurs at 1030 cm^{-1} , which is also accompanied by a small shoulder at 1240 cm^{-1} . CH bending in-plane vibrations extend from 1000 cm^{-1} up to 1400 cm^{-1} . The peak at 1310 cm^{-1} can be related to C–C stretch or C–H bending mode, while the peak located at 1600 cm^{-1} corresponds to C–C stretch. The last peak found in this spectrum at 1780 cm^{-1} belongs to the C=O stretch modes [25]. Because of the film thickness the peaks presented are mainly due to the molecular contribution rather than interaction with the substrate due to the absence of characteristic features at 620 and 2080 cm^{-1} corresponding to H–Si vibrations, as appear in spectrum (d). Spectra (b) and (c), which were recorded after annealing the sample at 150 and 175°C respectively, show no changes to the film. However, annealing the sample at higher temperature, 200 °C, a complete PTCDA desorption from the passivated Si(111) is obtained, spectrum (d). Therefore, PTCDA physisorption on the hydrogen-terminated surface is confirmed, and showing a weak Van Der Waals’ interactions between PTCDA and H:Si(111).

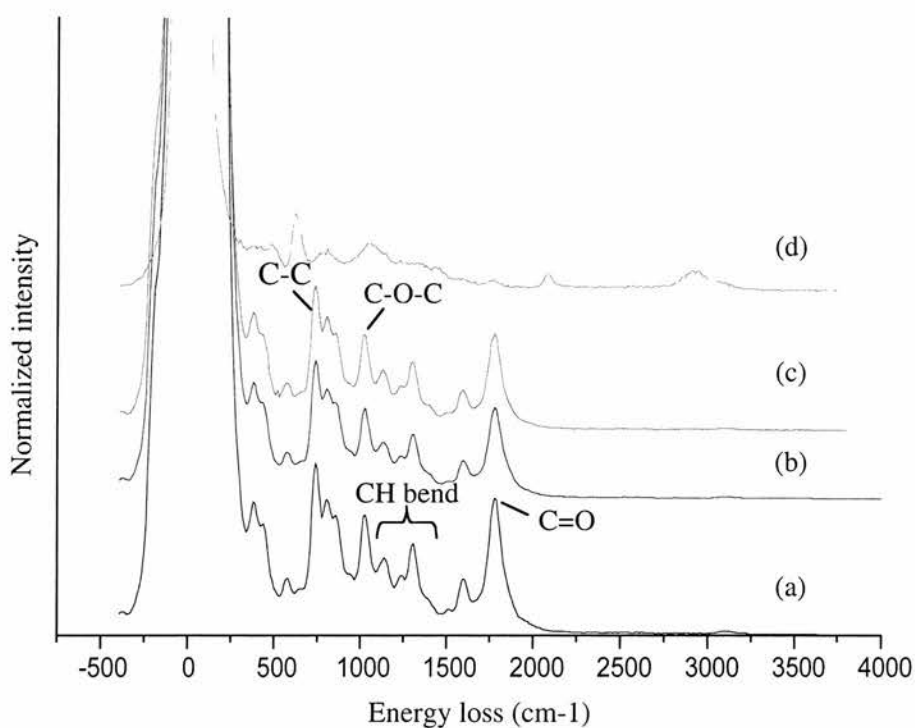


Fig. 6.5 Vibrational spectra of PTCDA on hydrogen-terminated Si(111) showing adsorption at room temperature (a), and annealing at 150°C (b), 175°C (c) and 200°C (d).

6.4 STM study

Firstly, STM images of PTCDA thin films grown at low surface coverage and low evaporation temperature are presented. Fig. 6.6 shows both the clean H:Si(111) surface and the surface after dosing with PTCDA for 5 min at 200 °C with the sample at room temperature. On the clean surface, shown in Fig. 6.6a, defects and step edges can be clearly identified. The defects with one atomic step height were created during the solution etching process. After exposure to PTCDA for 5 min, clusters, in a narrow

size range of $18 \text{ nm} \pm 4 \text{ nm}$ diameter, can be identified on the surface shown in Fig. 6.6b.

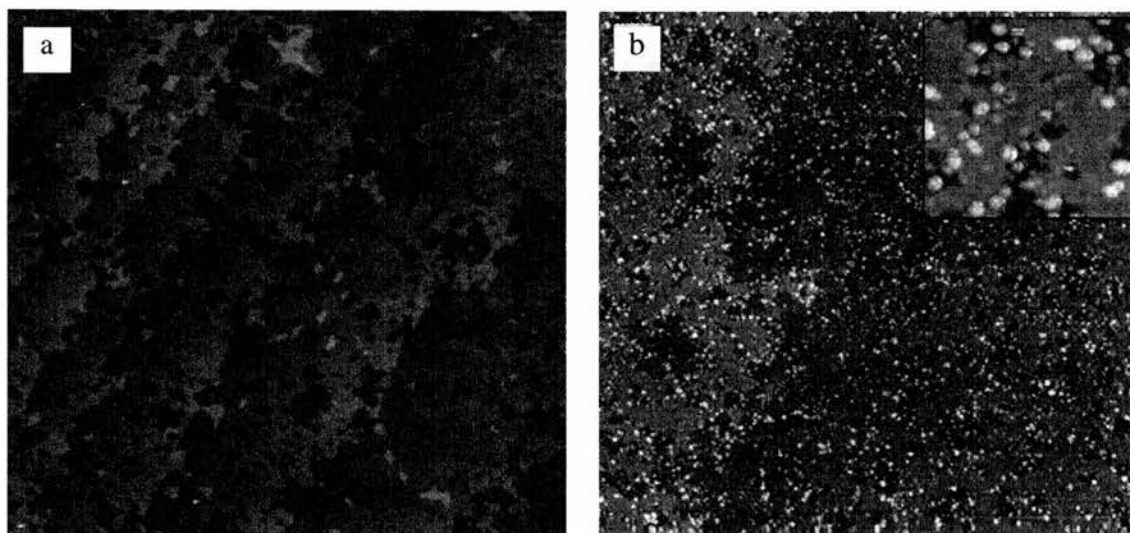


Fig. 6.6 STM images of (a) clean hydrogen passivated Si(111) surface (880 nm x 880 nm, bias=2.8 V, tunnelling current=0.06 nA) and (b) after 5 min dosing of PTCDA at 200°C (440 nm x 440 nm, bias=2.9 V, tunnelling current=0.15 nA). The insert shows a small area of the same image (50 nm x 50 nm).

After dosing for a further 10 min, a thick film is formed with a layered structure as shown in Fig, 6.7. The measured thickness of each layer is about 3.5 \AA , which is very close to the (102) interplanar spacing in the bulk crystal of PTCDA, 3.7 \AA , typical of π - π stacking distances in many crystals of aromatic molecules. On the image shown in Fig. 6.7a, the terraces appear to be elongated and terminated with bright features with a single molecular dimension. These bright features probably indicate a different structure or orientation for the molecules at the step edge compared to those in the

terrace. Fig. 6.7b shows an enlarged area within which molecular ordering can be identified as well as the enhanced tunnelling of step edge molecules.

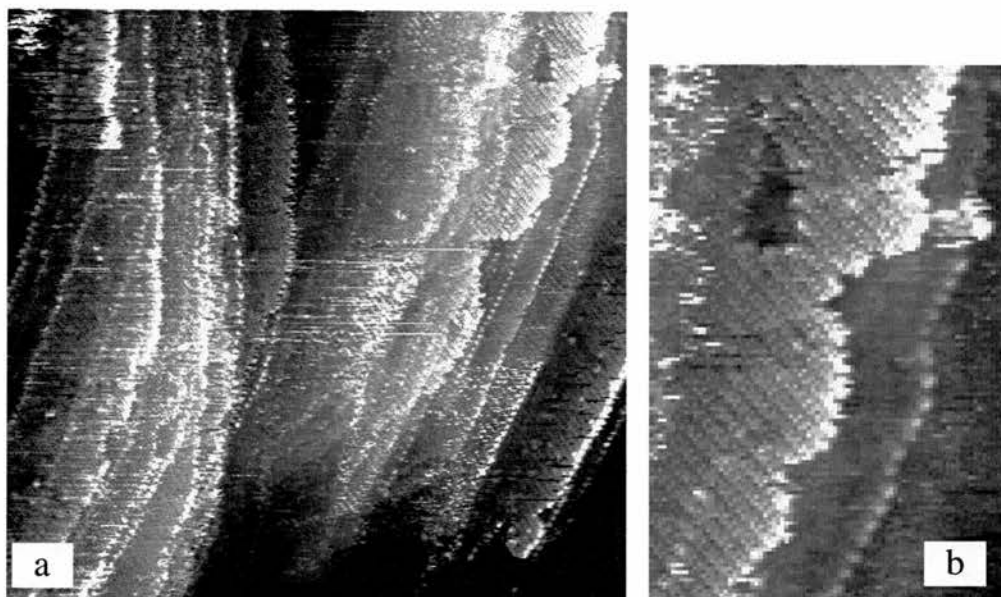


Fig. 6.7 STM image of PTCDA multilayer on H:Si(111) (a) large area (200 nm x 200 nm, bias=3.27 V, tunnelling current-0.1 nA). (b) An enlarged upper left corner of the same image.

A somewhat higher resolution STM image of the ordered structure is shown in Fig. 6.8a, while a small highly resolved area of a single terrace is shown in Fig. 6.8b. The unit cell has dimensions of $13 \text{ \AA} \times 21 \text{ \AA}$, which contains two molecules and appears as a centred structure. In the PTCDA bulk crystal, the (102) plane has very similar unit cell dimensions, either $11.96 \text{ \AA} \times 19.91 \text{ \AA}$ for the α phase or $12.45 \text{ \AA} \times 19.30 \text{ \AA}$ for the β phase [35]. These unit cells also contain two molecules related by glide lines. Although the 2D unit cell in the bulk has a rectangular shape ($\gamma=90^\circ$), the unit cell derived from the STM image is slightly distorted to an included angle of

$\gamma=103^\circ$, which is most likely due to a thermal drifting of the piezo scanner. Since there is no other known geometry on the same image, any fine calibration of the image becomes almost impossible. Nevertheless, both the angular and distance dimensions are within 15% and 8% of the bulk unit cell dimensions.

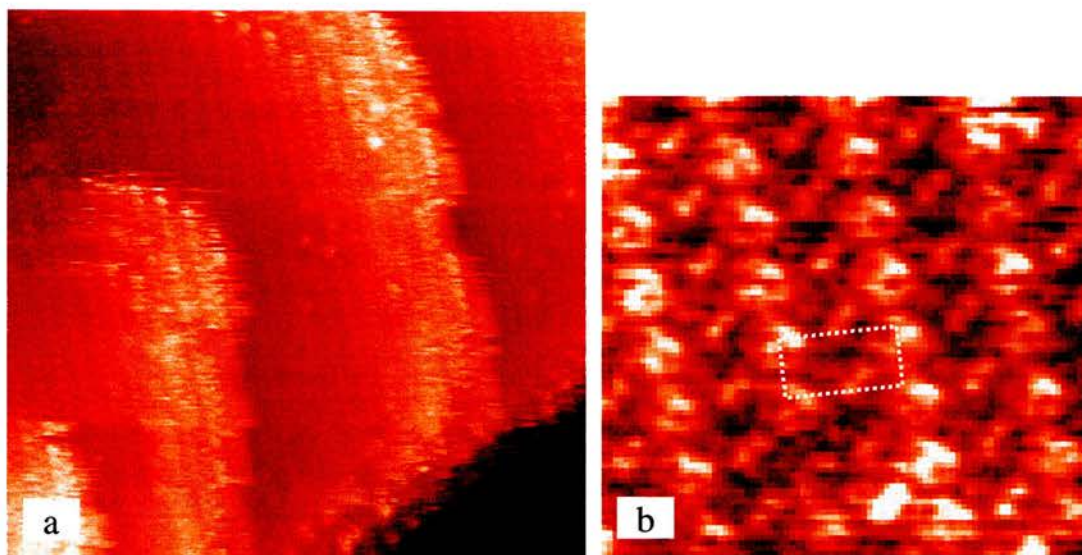


Fig. 6.8 (a) STM image of small area of PTCDA multilayer with molecular resolution. (56 nm x 56 nm, bias=2.84 V tunnelling current=0.06 nA). (b) An enlarged area (10 nm x 10 nm) shows the molecular arrangement within the unit cell.

A screw dislocation, presumably caused by the extension of a bulk defect, can be identified on the left side of the image in Fig. 6.8a. This screw dislocation indicates that the intermolecular interactions in the bulk crystal have multiple energy minima, particularly along the screw direction. This is also to be inferred from the observation, that there are two different forms of PTCDA crystal, namely α and β modifications [18,19,35]. Both forms contain a (102) plane (Fig. 6.4), to which the molecular plane is

parallel, forming a herringbone structure. While the quantitative differences of the 2D unit cell in the (102) plane are small, a major difference is found in the π -stacking direction (z-direction). For the α phase, the 2D unit cell of one molecular sheet is shifted along the long axis of the unit cell relative to the next molecular sheet, whereas for the β phase, it is translated along the short axis. The existence of different molecular arrangement along the z-direction makes it relatively easy to create local screw dislocation defects.

In the STM image with molecular resolution (Fig. 6.8b), the two features within the unit cell appear different in their brightness. Of course, it could be due to the difference in either the physical height, the electronic properties of those molecules or conceivably tip effects. Learning from the bulk crystal structure of PTCDA, the (102) basal plane has a glide plane symmetry, which implies that two molecules within the unit cell should be structurally equivalent. Also, the molecular plane is parallel to the (102) plane with only a small tilting angle [35]. Therefore, the height of the two molecules within the unit cell would be expected to be similar. However, in the presence of the underlying substrate, it has also previously been recognised that the PTCDA thin film does recognise the registration of the substrate. For example, for multilayer PTCDA on graphite surfaces [36] and KCl [18], a certain amount of strain was found for the first several layers of PTCDA. Here, it is suggested that the difference in the conductivity of two molecules within the unit cell reflects a difference in the registration of each molecule relative to the substrate.

The small clusters (18 nm diameter on average) adsorbed by heating the PTCDA doser to 200°C are highly mobile, which allows the formation of large crystalline domains even at room temperature. A variation in the mobility of clusters, as a function

of average size, has been proposed from *in-situ* photo luminescence measurement of PTCDA growth on alkali halide surface [34]. Here, in these experiments, by increasing the evaporation temperature to 230 °C, larger, but less mobile, clusters are deposited onto the surface. Fig. 6.9 shows a sequence of STM images at increasing dosing times. It is clear that, while the number of clusters increases with the exposure time, the average size of the clusters (65 nm) increases only very slightly. This indicates a typical diffusion limited growth process.

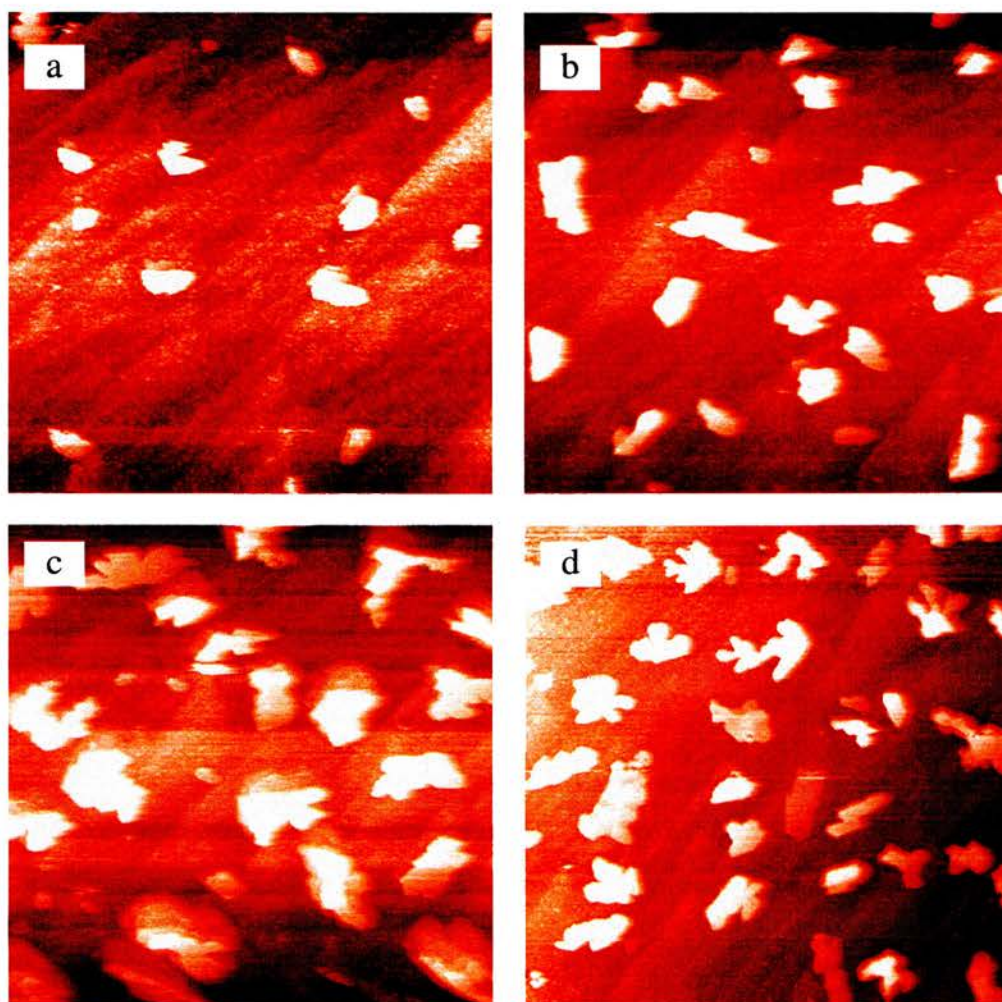


Fig. 6.9 STM images as a function of dosing time (a) 2 min, (b) 5 min, (c) 15 min, and (d) 17 min. All images have the same size $1 \mu\text{m} \times 1 \mu\text{m}$ (bias=2.7 V, tunnelling current=0.06 nA).

The slowly increase of the average size is contributed by the incorporation of the few small, mobile cluster species, which are likely to be present although not imaged because of their mobility at room temperature. Subsequently, the low diffusion of large clusters inhibits the growth of larger clusters and, therefore, the well-ordered domains described earlier, which are possible when the deposited clusters are much smaller and mobile. It seems clear, therefore, that, rather than individual molecules, clusters are deposited on the surface under these dosing conditions with a cluster size dependent on the dosing temperature. Higher evaporation temperatures create larger PTCDA clusters, and when the cluster has a size larger than about 30 nm, measured from the smallest diameter of the cluster in the images, the diffusion barrier becomes sufficiently high and diffusion at room temperature becomes inhibited. In turn this inhibits the formation of continuous films

To confirm that the average cluster size is determined by the evaporation temperature, the dosing temperature was further increased up to 250 °C. Fig. 6.10 shows a large area STM image with many large clusters. Typically, the crystal has a dimension of 150 nm along the longer side of the cluster. Combined with the previous dosage time dependent STM observations, it can be readily concluded that it is the evaporation temperature that determines the average cluster size, although it is difficult to measure the thickness of each cluster while the dosing time determines the number of clusters.

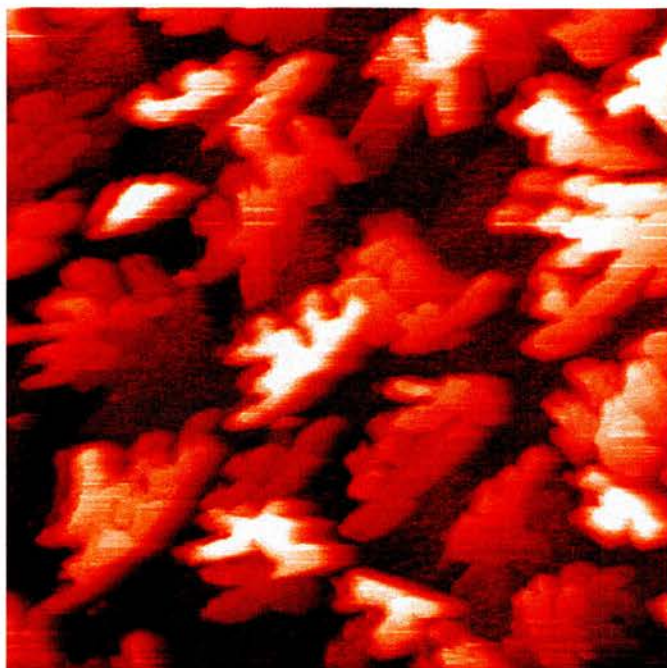


Fig. 6.10 STM image of PTCDA crystals deposited at 250°C. ($1\ \mu\text{m} \times 1\ \mu\text{m}$, bias=2.32 V, tunnelling current=0.07 nA).

Under the high evaporation temperature conditions, individual crystallites show a dendritic structure, which is due to the preferential growth of the crystal along different directions. Along these crystal growth directions, the intermolecular interactions must be more strongly attractive compared with other directions. When the unit cell has two or more directions with similar attractive interactions, alternating growth of the crystal between these directions can lead to dendritic structures. Similar dendritic crystal shape has also been observed for PTCDA growth on alkali halide surfaces with AFM [34] and pentacene on Si(001) and SiO₂ surfaces [37]. For molecules, such as PTCDA with D_{2h} symmetry, quadrupole interactions are responsible for the formation of typical herringbone structures. Specifically, for PTCDA, the quadrupole interactions are aligned along the diagonal of the unit cell on the (102) plane.

Figure 6.11a shows the STM image of a single cluster with lateral dimensions greater than 120 nm. Angles at the edge of the cluster are characteristic of the bulk PTCDA structure. The cluster is terminated with a flat terrace. Interestingly, on the upper right side of the cluster, a hole with a dimension of 20 nm x 10 nm can be identified as a large 3D defect. Since the large terrace is flat and the crystallite shows good conductivity, it was possible to achieve molecular resolution within this terrace. Fig. 6.11b and c show the high resolution STM images in two different areas of the cluster. The herringbone structure can be clearly identified, with a typical unit cell of 12 Å x 19.5 Å containing two molecules per unit cell. The bright STM features appear to be slightly elongated consistent with the rectangular shape of the molecule. The longer axis of the molecule can be easily identified. The measured enclosed angle between the long axis of the two molecules in the unit cell is about $98^\circ \pm 1^\circ$. This angle suggests that it is the α phase (96°) rather than the β phase (104°) is formed at room temperature.

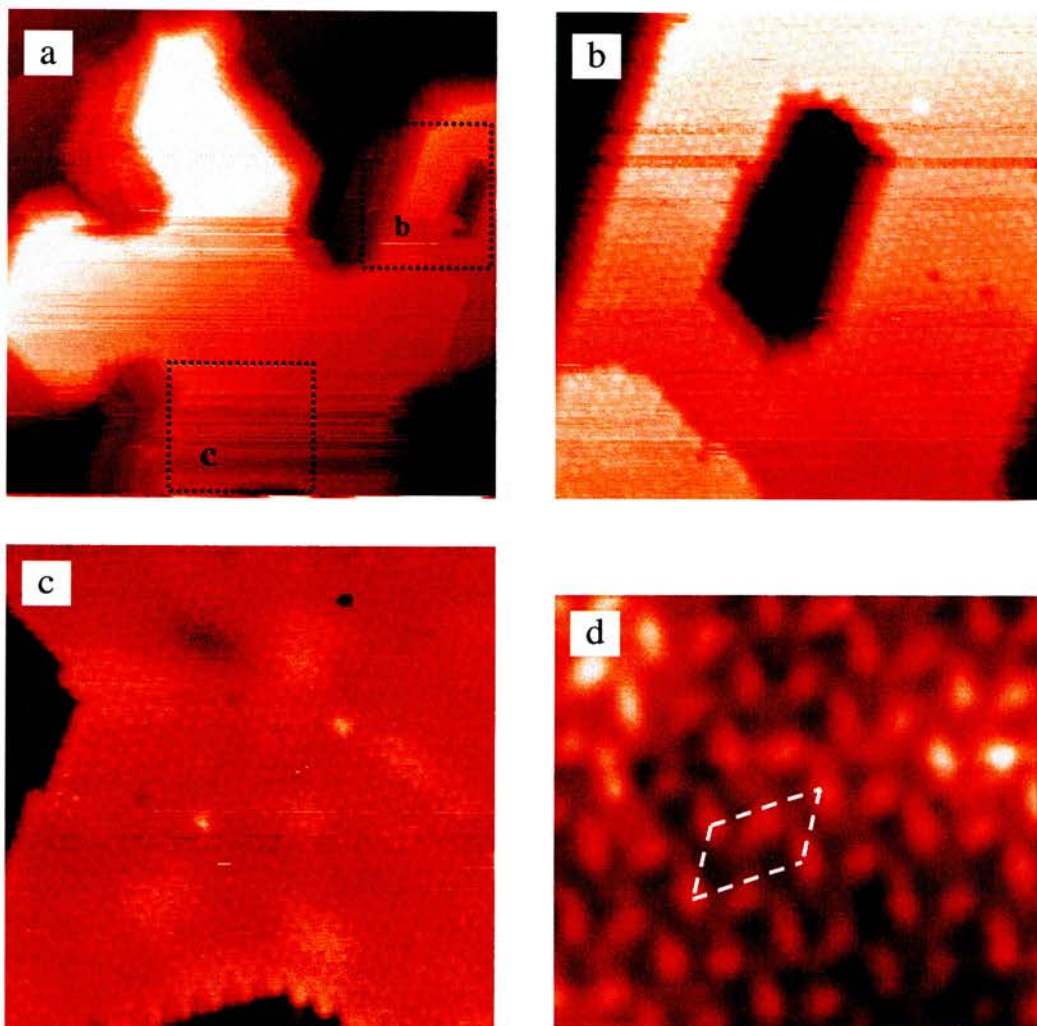


Fig. 6.11 a) STM image (118 nm x 118 nm) of a PTCDA single crystal. b) An enlarged area (39 nm x 39 nm) of the upper left corner. c) An enlarged area (40 nm x 40 nm) of the lower part of the crystal. d) Further enlarged flat terrace (12 nm x 12 nm) with molecular resolution. The herringbone structure is clearly resolved. All images are taken at bias=2.32 V, tunnelling current=0.07 nA.

In the bulk PTCDA crystal, the unit cell of the (102) plane has a rectangular shape, with a short vector of 11.96 Å ([010] direction of the α -phase) and 12.45 Å ([201] direction of the β -phase). Along these directions, molecules are closely

packed. The obtuse angle between the diagonal and the shorter unit cell vector is 121.0° (121.8°) in the α -phase (β -phase), while between the diagonal and the longer unit cell vector is 149.0° (147.2°). Meanwhile, the angle between diagonals is 118.0° (114.4°). The crystal angles measured in the STM images are about 120° , which are close to the angle between two diagonal directions or that between the shorter unit cell side and the diagonal direction. However, an image with molecular resolution can, in principle, distinguish which of these alternatives defines the crystal morphology and in turn therefore able to give direct evidence for the driving force responsible for the formation of particular dendritic structures. Note that calibration of the STM image is not sufficiently precise to distinguish between α - and β -phases, on the basis of the macroscopic crystal angles.

The crystal structure of PTCDA has already been examined with either x-ray [18] and electron diffraction [19] techniques. Both techniques extract the structural information from the reciprocal space. To our knowledge, this is the first time to study the PTCDA crystal in real space with molecular resolution. With molecular resolution, one can easily identify the termination of the step edges. It is clear that only two types of step edges are formed to define the macroscopic α phase crystal shape, either along [010] vector, the short axis, and [-211] vector, the diagonal axis, of the PTCDA bulk crystal unit cell. Of course, these two directions are important in the bulk PTCDA crystal. Along the short unit cell vector, molecules are densely packed which could be a result of local attractive columbic interactions between the negatively charged oxygen of the anhydride group and the positively charged hydrogen atoms on the adjacent CH bonds. The nearest distance between the hydrogen atoms and the oxygen atoms is about

1.9 Å, and the O··H—C distance is about 3.0 Å. For a typical H-bonding, the X-H---Y distance is about 2.8 Å to 3.4 Å. Therefore, it is likely that the H-bonding is responsible for the stabilisation of in-plane structures.

6.5 *Ab initio* results

As mentioned before, along the close packed direction molecules achieve maximum interactions between these two opposite charged groups (atoms). Meanwhile, along the diagonal direction, similar columbic interactions are also satisfied, forming an H-bonding matrix. To quantify these attractive intermolecular interactions, *ab initio* calculations have been carried out on clusters of PTCDA molecules resembling part of the unit cell in the bulk (102) plane. Fig. 6.12a shows the charge distributions of an isolated molecule calculated using the Gaussian 98 package [38] within the B3LYP density functional method and an STO-3g basis set. As expected, opposite charges are localised on oxygen and hydrogen atoms, which decorate the sides of the molecule. Therefore, attractive interactions are expected between these sides. In Fig. 6.12b and c, the interaction energy of two different PTCDA dimers, using their relative positions within the unit cell are indicated. To simplify the calculation, the average dimension between α and β phases were used, that is 12.2 Å x 19.6 Å with an angle of 40° between the long molecular axis and the short axis. The arrangement shown in Fig. 6.12b corresponds to the attractive interaction (22.3 kJ/mol) between the translationally inequivalent molecules of the unit cell which define the herringbone structure, while the parallel aligned model of Fig. 6.12c relates to the attractive interaction (21.5 kJ/mol) between translationally equivalent molecules along the shorter unit cell vector. To confirm that these attractive interactions are the dominating forces responsible for

the formation of the molecular arrangement within the (102) plane of the PTCDA crystal, a cluster of five PTCDA molecules was also calculated. The total attractive interaction was found to be 133.9 kJ/mol. As there are four T-type interactions and two of parallel interactions along the short axes, the total interaction based on the sum of molecular pairwise interactions should be 132.3 kJ/mol. The small difference (1.6 kJ/mol) between these estimation suggests that indeed these are the strongest intermolecular interactions within the (102) plane. Meanwhile, because the interactions in these two different arrangements are very similar, the boundaries of the crystal edges are dominated by alignment along the short axis and the diagonal axis of the unit cell. Therefore, the crystal shape is determined by the growth along the short axis and the diagonal which, in turn, contributes to the form of the dendritic crystal with enclosed angles of 120°.

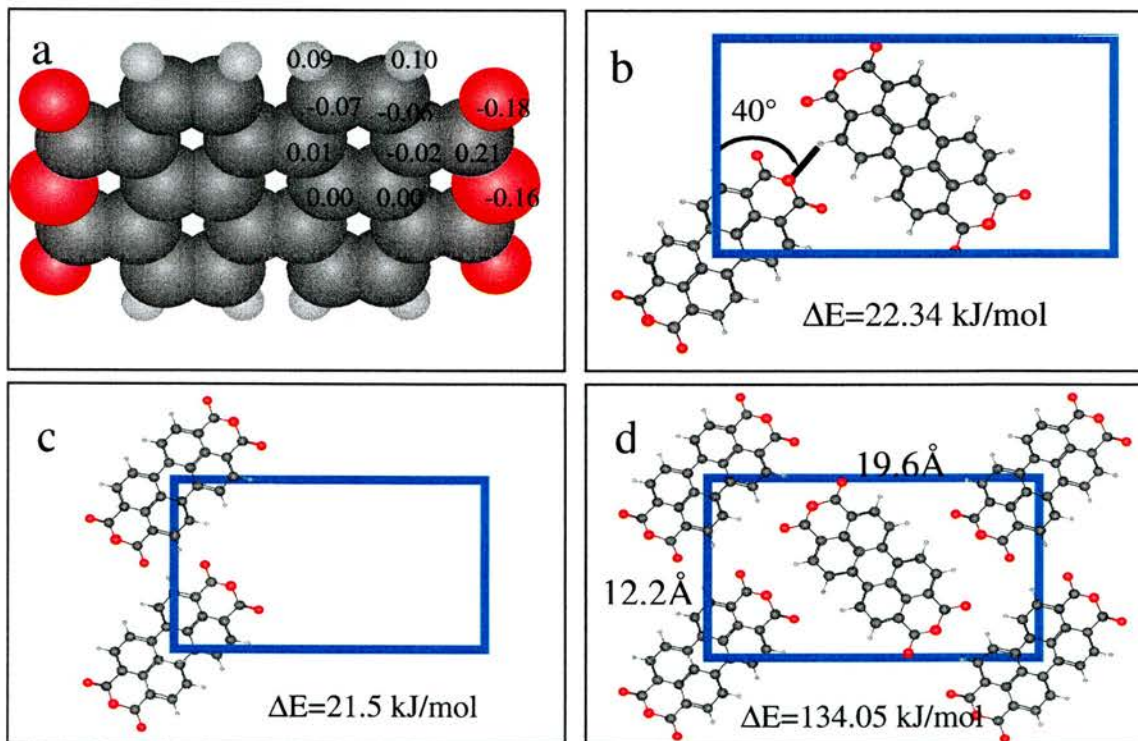


Fig. 6.12 a) Calculated atomic charges of a free, single PTCDA molecule. b) Molecular dimer with perpendicular arrangement, c) dimer of molecules

aligned parallel along the short axis of the unit cell and d) a cluster of five molecules corresponding to the unit cell.

6.6 Conclusions

In this work, an STM study of molecular deposition of PTCDA on an passivated hydrogen terminated Si(111) surface is presented. At low evaporation temperature, 200 °C, small clusters, with a diameter of 18 nm, are deposited on the surface, which are able to diffuse and coalesce to form large ordered domains. Larger clusters are deposited onto the surface at higher evaporation temperatures. The diffusion of cluster with a size larger than 30 nm is limited at room temperature. For the larger clusters, dendritic crystal shapes are observed. STM images with molecular resolution have been analysed to identify the molecular mechanism for the formation of the dendritic crystals. Physisorption of PTCDA on H:Si(111) was confirmed through HREELS results.

References

- 1 J. M. Shaw, P. F. Seidler, IBM J. R&D. 45, 3 (2001).
- 2 C. D. Dimitrakopoulos, P. R. L. Malenfant, Adv. Mater. 14, 99 (2002).
- 3 A. Bohler, P. Urbach, D. Ammermann, W. Kowalsky, Mat. Sci. Eng. B-Solid 51, 58 (1998).
- 4 Y. Toda, H. Yanagi, Appl. Phys. Lett. 69, 2315 (1996).
- 5 J. H. Schon, Ch. Kloc, A. Dodabalapur, B. Batlogg, Science 289, 599 (2000).
- 6 S. R. Forrest, Chem. Rev. 97, 1793 (1997).

-
- 7 W. Kowalsky, T. Benstem, A. Bohler, S. Dirr, H-H. Johannes, D. Metzdorf, H. Neuner, J. Schobel, P. Urbach, *Phys. Chem. Chem. Phys.* 1, 1719 (1999).
 - 8 T. U. Kampen, G. Salvan, M. Friedrich, D. A. Tenne, S. Park, D. R. T. Zahn, *Appl. Surf. Sci.* 166, 387 (2000).
 - 9 Q. Chen, T. Rada, A. McDowall, N. V. Richardson, *Chem. Mater.* 14, 743 (2002).
 - 10 C. Ludwig, B. Gompf, J. Petersen, R. Strohmaier, W. Eisenmenger, *Z. Phys. B* 93, 365 (1994).
 - 11 M. Tangelin-Nilsson, L. Ilver, J. Kanski, *Surf. Sci.* 464, 265 (2000).
 - 12 A. O. Morozov, T. U. Kampen, D. R. T. Zahn, *Surf. Sci.* 446, 193 (2000).
 - 13 J. R. Ostrick, A. Dodabalapur, L. Torsi, A. J. Lovinger, E. W. Kwock, T. M. Miller, M. Galvin, M. Berggren, H. E. Katz, *J. Appl. Phys.* 81, 6804 (1997).
 - 14 Z. Shen, P. E. Burrows, V. Bulovic, S. R. Forrest, M. E. Thompson, *Science* 276, 2009 (1996).
 - 15 D. Y. Zang, F. So, S. R. Forrest, *Appl. Phys. Lett.* 59, 823 (1991).
 - 16 D. Y. Zang, Y. Q. Shi, F. So, S. R. Forrest, W. H. Steier, *Appl. Phys. Lett.* 58, 562 (1991).
 - 17 R. Hudej, G. Bratina, *Solid State Commun.*
 - 18 M. Mobus, N. Karl, T. Kobayashi, *J. Cryst. Growth* 116,495 (1992).
 - 19 T. Ogawa, K. Kuwamoto, S. Isoda, *Acta Crystallogr. B* 55, 123 (1999).
 - 20 D. Schlettwein, H. Tada, S. Mashiko, *Thin Solid Film* 331, 117 (1998).
 - 21 Y. Hirose, S. R. Forrest, A. Kahn, *Phys. Rev. B* 52, 14040 (1995).
 - 22 T. Schmitz, F. Sellam, R. Staub, M. Torker, T. Fritz, T. Kubel, K. Mullen, K. Leo, *Surf. Sci.* 445, 358 (2000).
 - 23 T. Schmitz, T. Fritz, F. Sellam, R. Staub, K. Leo, *Phys. Rev. B* 55, 7972 (1997).

-
- 24 T. Schmitz, T. Fritz, R. Staub, A. Back, N. R. Amrstrong, K. Leo, *Surf. Sci.* 437, 163 (1999).
- 25 F. S. Tautz, S. Sloboshanin, V. Shklover, R. Scholtz, M. Sokolowski, J. A. Schaefer, E. Umbach, *Appl. Surf. Sci.* 166, 363 (2000).
- 26 K. Glockler, C. Seidel, A. Soukopp, M. Sokoloswki, E. Umbach, M. Bohringer, R. Berndt, W. –D. Schneider, *Surf. Sci.* 405, 1 (1998).
- 27 M. Bohringer, W. –D. Schneider, K. Glockler, E. Umbach, R. Berndt, *Surf. Sci. Lett.* 419, L95 (1998).
- 28 F. S. Tautz, M. Eremtchenko, J. A. Schaefer, M. Sokolowski, V. Schlover, K. Glockler, E. Umbach, *Surf. Sci.* 502, 176 (2002).
- 29 M. Gabriel, M. Stohr, R. Moller, *Appl. Phys. A-Mater.* 74, 303 (2002).
- 30 J. J. Cox, T. S. Jones, *Surf. Sci.* 457, 311 (2000).
- 31 G. S. Higashi, R. S. Becker, Y. J. Chabal, A. J. Becker, *Appl. Phys. Lett.* 58, 1656 (1991).
- 32 T. U. Kampen, G. Salvan, D. Tenne, R. Scholz, D. R. T. Zahn, *Appl. Surf. Sci.* 175, 326 (2001).
- 33 B. Uder, C. Ludwig, J. Petersen, B. Gompf, W. Eisenmenger, *Z. Phys. B* 97, 389 (1995).
- 34 D. Schlettwein, H. Tada, S. Mashiko, *Thin Solid Films* 331, 117 (1998).
- 35 B. Krause, A. C. Durr, K. A. Ritley, F. Schreiber, H. Dosch, D. Smilgies, *Appl. Surf. Sci.* 175, 332 (2001).
- 36 C. Ludwig, B. Gompf, W. Glatz, J. Petersen, W. Eisenmenger, M. Mobus, U. Zimmermann, N. Karl, *Z. Phys. B* 86, 397 (1992).
- 37 F. J. M. Z. Heringdorf, M. C. Reuter, R. M. Tromp, *Nature* 412, 517 (2001).

38 M. J. Frisch, G. W. Trucks, H. B. Schlegel, G. E. Scuseria, M. A. Robb, J. R. Cheeseman, V. G. Zakrzewski, J. A. Montgomery, R. E. Stratmann, J. C. Burant, S. Dapprich, J. M. Millam, A. D. Daniels, K. N. Kudin, M. C. Strain, O. Farkas, J. Tomasi, V. Barone, M. Cossi, R. Cammi, B. Mennucci, C. Pomelli, C. Adamo, S. Clifford, J. Ochterski, G. A. Petersson, P. Y. Ayala, Q. Cui, K. Morokuma, D. K. Malick, A. D. Rabuck, K. Raghavachari, J. B. Foresman, J. Cioslowski, J. V. Ortiz, B. B. Stefanov, G. Liu, A. Liashenko, P. Piskorz, I. Komaromi, R. Gomperts, R. L. Martin, D. J. Fox, T. Keith, M. A. Al-Laham, C. Y. Peng, A. Nanayakkara, C. Gonzalez, M. Challacombe, P. M. W. Gill, B. G. Johnson, W. Chen, M. W. Wong, J. L. Andres, M. Head-Gordon, E. S. Replogle, and J. A. Pople, , Revision A.7 ed. (Gaussian, Inc., Pittsburgh PA, 1998).

Scanning tunnelling microscopy of tetracene on Si(100)-2x1

7.1 Introduction

There has been much recent interest in the electronic and optoelectronic properties of polyaromatic hydrocarbons, such as tetracene, pentacene and perylene, because of their potential use as organic laser, OLEDs, and OFETs [1,2,3]. An enormous improvement in the performance of these devices has been achieved, and it is likely that the performance is strongly influenced by the structural quality of crystals or preferably thin films. Since silicon retains its powerful influence in the microelectronic industry, it is important to consider in detail the interaction between Si(100) surfaces and those molecules which can contribute to its advanced applications.

Pentacene, which is a planar molecule with five, in line, benzene rings, has been widely studied in the past [3,4] with reference to its applications in OLEDs. Pentacene and tetracene, in particular, display a startling range of phenomena related to correlated electronic behaviour. These are the only known materials that exhibit the quantum Hall effect [5]. Among the interest for studying these aromatic molecules are the high mobility for hole transport (p-channel) [6], and low defect densities which can be achieved in FET devices. Also, it has been found that the charge transport in the acene crystals such as anthracene, tetracene or pentacene, is dominated by electron-phonon

interaction [5,7,8,9]. In general, the electronic structure of the polyacene (tetracene, pentacene, etc.) crystals is characterized by an energy gap of several electron volts between the states derived from the HOMO (highest occupied molecular orbital) and the LUMO (lowest unoccupied molecular orbital) [8]. Although these studies relate to bulk pentacene crystals, its adsorption on Si(100)-2x1 substrate has also been investigated [5,10,11]. It has been suggested that the molecule adopts a flat-lying configuration with orientation both parallel and perpendicular to the dimer rows [10].

The polyacene family consists of strongly bonded aromatic molecules arranged on a bulk crystal lattice with weak van der Waals intermolecular interactions. The tetracene molecule $C_{18}H_{12}$ is also a planar molecule and in this case four aromatic rings form a linear array, see Fig. 7.1. Also, it is assumed that tetracene molecule retains its full D_{2h} symmetry with the Van Der Waals' size of $13.63 \text{ \AA} \times 6.99 \text{ \AA}$. The molecular lattice is easily polarizable, so it has been suggested for polyacenes that the charge carriers are small polarons [9].

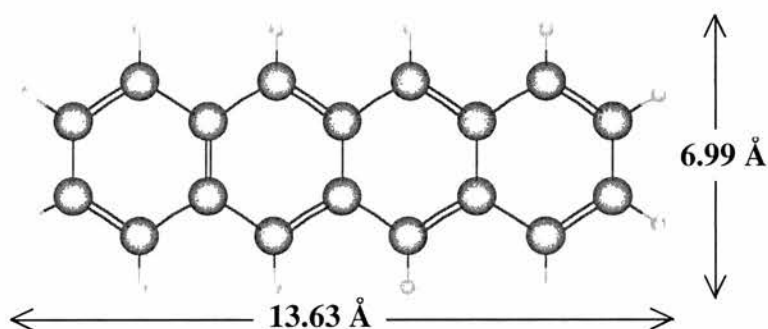


Fig. 7.1 shows the tetracene molecule with its van der Waals radii.

In the present chapter, vibrational and topographical studies of the adsorption of tetracene molecule on both hydrogen-terminated Si(111) and Si(100)-2x1 surfaces at

room temperature are described. Also, some *ab initio* calculations have been done in order to obtain additional information regarding the electronic structure of an isolated tetracene molecule. Charge densities arising from specific molecular orbital are then compared with STM images obtained at different bias polarities.

Although STM provides us with real space images, which it is desired to relate to structure, size and shape of organic molecules adsorbed on various surfaces [12,13,14], it is necessary to keep in mind that those images are presumed to originate from molecular orbitals which are modified by adsorption, but also influenced by different tunnelling factors at the molecular adsorption site, such as effective barrier height, atomic structure, and resonant tunnelling [10,15,16,17]. These factors are difficult to address but relevant to a detailed interpretation of this system and understanding of the detailed physical and electronic structure of tetracene on Si(100)-2x1.

7.2 Review of benzene on silicon surfaces

The interaction of benzene with the (100) and (111) surfaces of silicon has proven to be an interesting model system for molecular adsorption on semiconductor surfaces. The earliest experiments revealed a strong chemisorption state for benzene on cleaved Si(111)-2x1 at room temperature [18]. Later experiments found that benzene is also chemisorbed on Si(111)-7x7 at room temperature, although rather weakly, with an energy barrier for desorption of approximately 1.0 eV [19, 20]. In one of the first definite demonstrations of crystal-face specificity in chemical bonding on Si, benzene was found to chemisorb on Si(100)-2x1 through σ orbitals [21], in contrast to the π orbital observed on Si(111)-7x7 [20].

The adsorption of benzene on Si(100)-2x1 surface has been studied in recent years by both experimental surface science techniques and theoretical methods [21,22,23,24,25]. Based on a combined study using HREELS, thermal-desorption spectroscopy, and Auger electron spectroscopy, Taguchi et al. [21] showed that benzene is non-dissociatively chemisorbed on the surface at room temperature. Borovsky et al. [26] reported that benzene initially adsorbs in a metastable state and subsequently converts to a lower-energy configuration. Using high-resolution images (see Fig. 7.2) they investigated the appearance of each state and its location relative to the surface dimers.

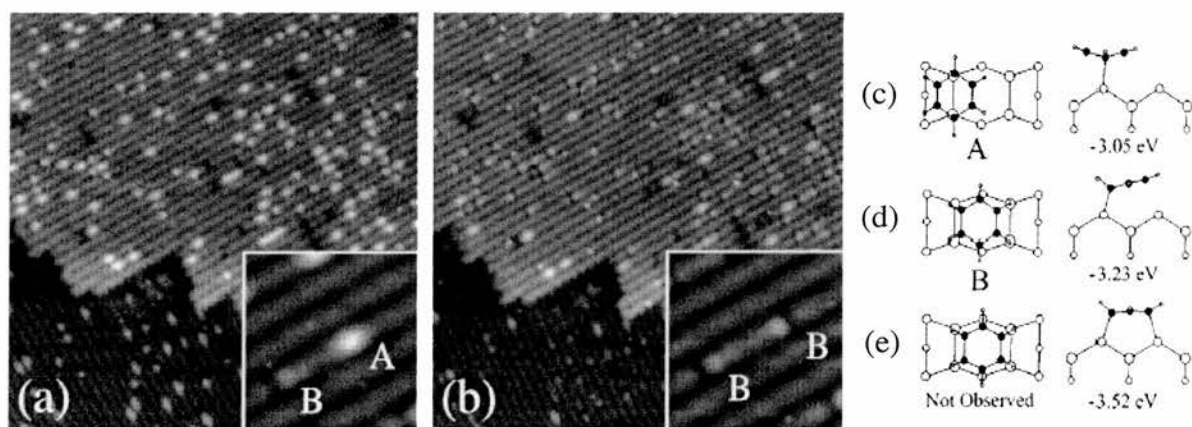


Fig. 7.2 A pair of $400 \times 400 \text{ \AA}^2$ STM images from a room-temperature experiment in which a clean Si(001) surface was exposed to 0.06 L of benzene. Part (a) shows that benzene is initially adsorbed into a state (A) that appears bright and symmetric. Part (b) shows that nearly all of the benzene converts to a state (B) that is fainter in appearance. The insets show a $60 \times 60 \text{ \AA}^2$ area from two higher-resolution images. Also, the top and side views of structural models of benzene chemisorbed on Si(100) (c) assigned to state A, and (d)

assigned to state B. (e) shows the lowest-energy state calculated by Jeong *et al.* (Ref. 23), which is not observed. From Ref. 26, Borovsky *et al.*

Wolkow's group has studied some organic molecular adsorption on Si(100) in particular benzene [24], both experimentally and theoretically. In an experimental investigation, STM images showed that the molecule can adopt three distinct adsorption geometries. The STM images reveal approximately where molecular adsorption occurs (see Fig. 7.3), but not enough information to determine the details of the structure. Thus, they considered various adsorption configurations and calculated fully optimized structures and absolute adsorption energies for each.

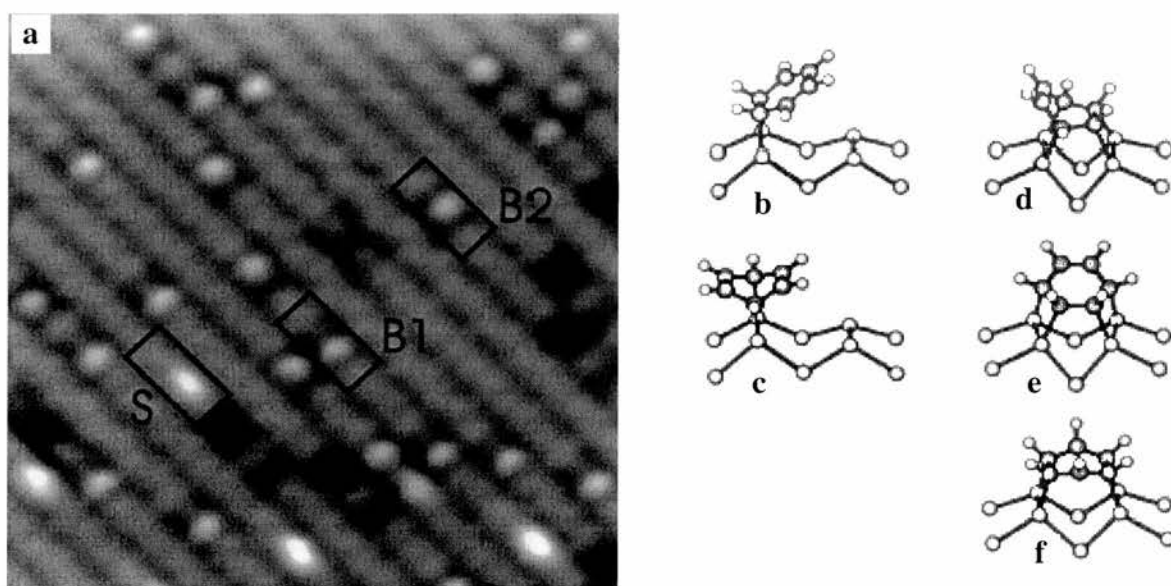


Fig. 7.3 STM image of benzene on Si(100) at 293 K ($V_{\text{sample}} = -1.5$ V, $I = 40$ pA). The labels indicate examples of single dimer bound benzene (S) and two different bridging configurations (B1 and B2). The rectangles denote the four dimers units. (b-f) Schematic diagrams of benzene–Si(100) adsorption geometries: (b) 1,2 single dimer; (c) 1,4 single dimer; (d) tight bridge; (e) twisted bridge; (f) symmetric bridge. Taken from Wolkow [24].

In Fig. 7.3a, the largest protrusions, labelled S, are centred over one dimer. The features labelled B1 and B2 occupy two dimers and are associated with bridge bonded benzene. B1 and B2 are asymmetric with respect to the dimer row and the dimer bond respectively. In addition, Fig. 7.3 also shows the five bonding geometries used to model benzene adsorption using semiempirical AM-1 method. It was concluded that the type S features in the image are due to the 1,4 structure shown in Fig. 7.3d. Also, the features labelled B1 and B2 correspond well with the simulated images for the tight (Fig. 7.3e) and twisted (Fig. 7.3f) bridge geometries, respectively. For both of these configurations, the bright features are seen to correspond to the single remaining double bond on the bonded benzene molecule.

7.3 Vibrational study

Infrared spectra of tetracene both calculated, using Gaussian 98 [27], and experimental, in KBr [28], are shown in Fig. 7.4, which are in excellent agreement with the infrared spectrum of free tetracene molecule presented in The Aldrich Library of Infrared Spectra [29] in the frequency range from 650 – 4000 cm^{-1} .

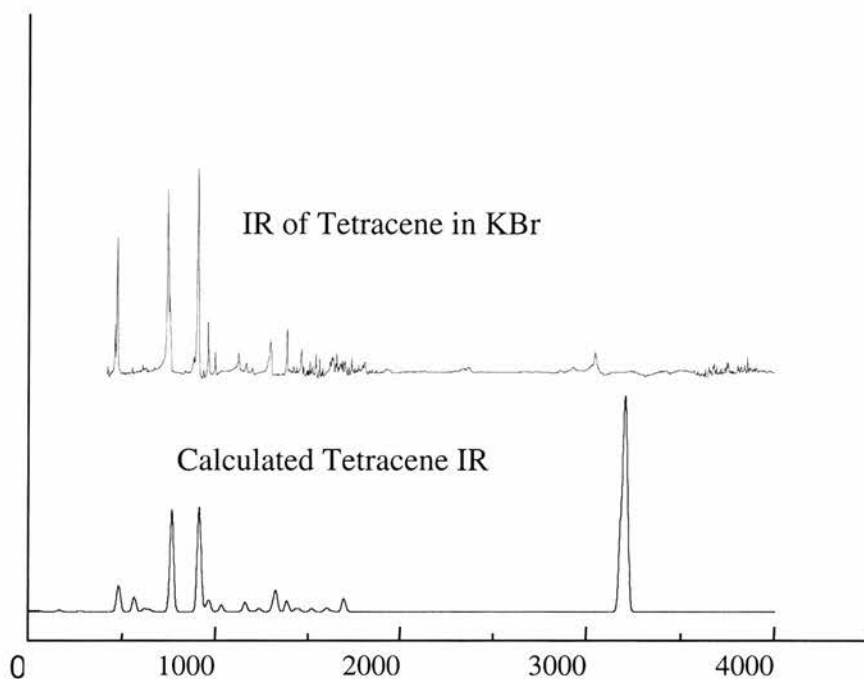


Fig. 7.4 Infrared spectra of tetracene molecule theoretical, using Gaussian 98, (lower spectrum) and experimental, in KBr, (upper) show similar peaks in general.

High resolution electron energy loss spectroscopy was used to follow the growth of the tetracene thin film on passivated Si(111) surface at room temperature. Although many electron-vibration interactions studies have been carried out on some polycyclic aromatic hydrocarbons, including tetracene and pentacene most of them are related to the infrared modes of the radical cation of these molecules [30,31].

Figure 7.5 shows spectra of both the clean H:Si(111) surface and a multilayer thin film of tetracene on this substrate, after dosing for 20 min. The HREEL spectrum (a) shows the characteristic peaks for clean hydrogen terminated Si(111) at 620 and 2080 cm^{-1} corresponding to bending mode $\beta(\text{Si-H})$, and stretching mode $\nu(\text{Si-H})$ respectively [32]. The latter spectrum provides an overview of the molecular geometry of this thin film, where several sharp peaks can be noticed.

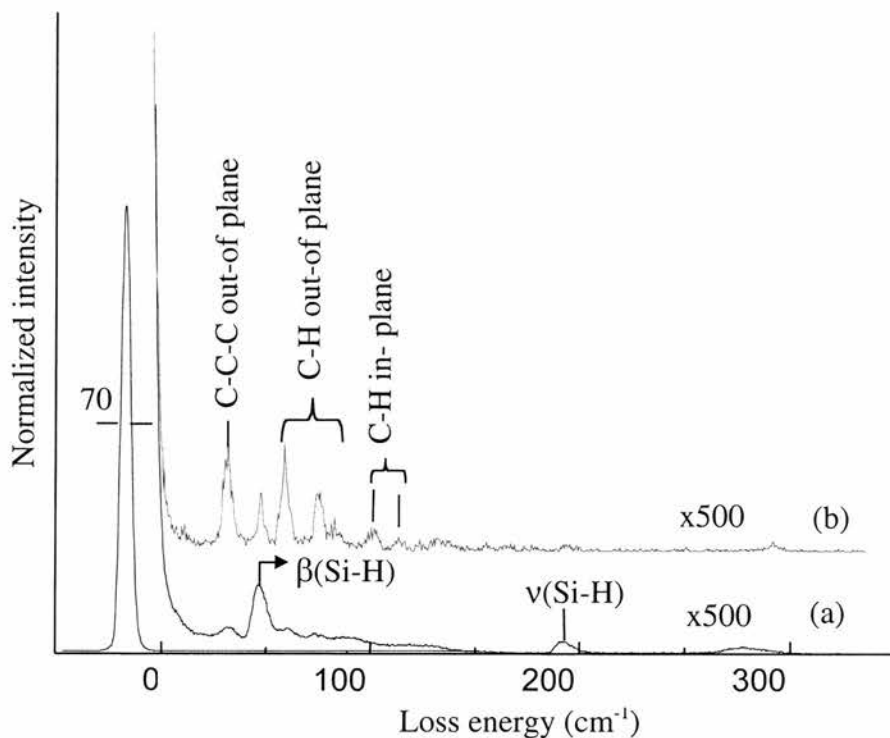


Fig. 7.5 Spectrum of a) clean hydrogen-terminated Si(111) and b) tetracene multilayer deposited on that surface.

Four sharp peaks under 1000 cm^{-1} can be distinguished from spectrum (b); those loss peaks are located at 470 , 620 , 740 and 890 cm^{-1} . The one at 620 cm^{-1} corresponds to Si-H bending mode from the substrate. The intensity of those peaks compared to the Si-H peak suggests multilayer coverage. Peaks at 740 and 890 cm^{-1} correspond to C-H out-of-plane bending modes [33], the peak at 460 cm^{-1} corresponds to (C-C-C) out-of-plane bending mode [21]. Also, others small feature are present in the spectrum (b) at 1160 , 1280 , and 3065 cm^{-1} . Details of those peaks are as follow: small peaks at 1160 , 1280 cm^{-1} correspond to C-H in-plane bending modes [21], the peak located at 3065 cm^{-1} corresponds to the C-H stretching mode. Since the dominant features are out-of-plane modes, the surface selection rule leads to the conclusion that there is flat-lying adsorption of tetracene on the passivated Si(111) surface even as a multilayers film.

7.4 Desorption of tetracene from H:Si(111) at room temperature.

The EEL spectra in Fig. 7.6, taken as a function of time, show that the desorption takes place at room temperature for tetracene from H:Si(111) surface, until after 23 hours obtaining almost a “clean” substrate again, which has the Si-H distinctive peak, at 620 cm^{-1} , as predominant. These results confirm not only the weak Van Der Waals (vdw) bonds between tetracene molecules in this multilayer film, but also the weak interaction between perylene molecules and H:Si(111) substrate. It is noticeable that all tetracene adsorption peaks decrease during the time, but some peaks fall faster than other within the three initial hours, for instance that located at 740 cm^{-1} .

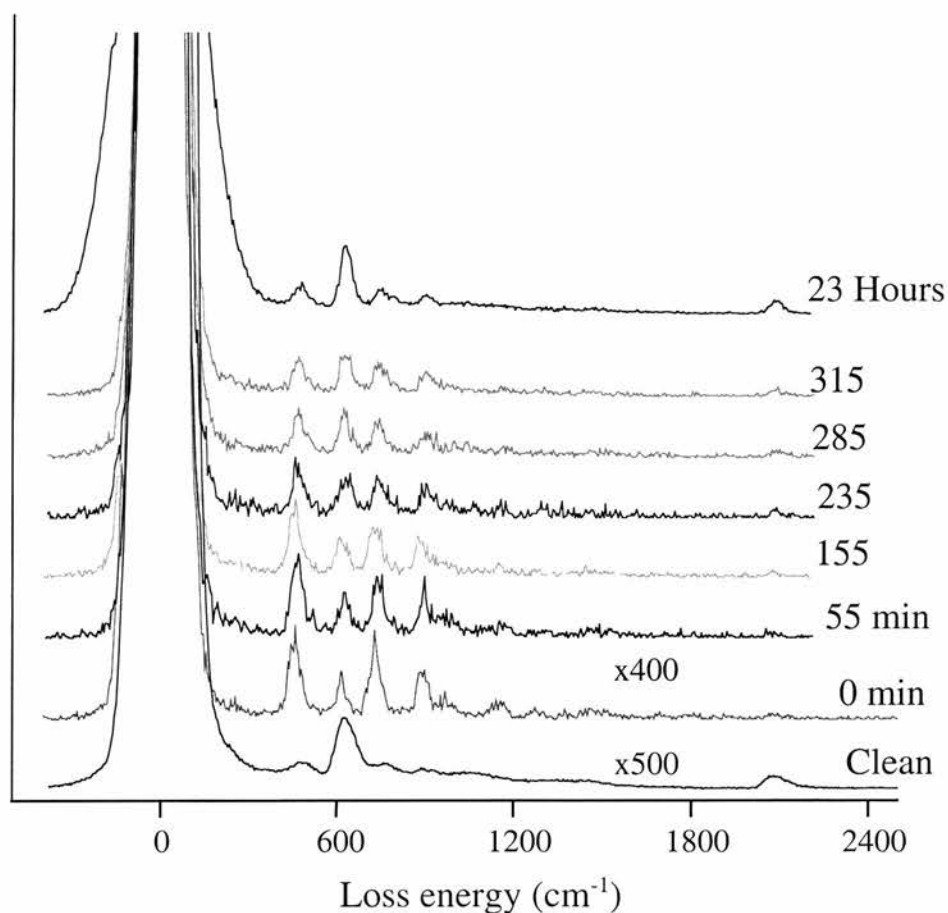


Fig. 7.6 EEL spectra of tetracene on H:Si(111) showing desorption of tetracene at room temperature.

The detailed behaviour of individual peaks, 470 and 740 cm^{-1} , with time can be seen in Fig. 7.7. In the first case, a steadily decrease on the intensity is presented. While the loss intensity for the peak at 740 cm^{-1} has a more complex dependence on the time. Here, the intensity falls sharply in the first hour, while the next two hours show a little decrease on the loss intensity followed by a further decrease in the next three hours.

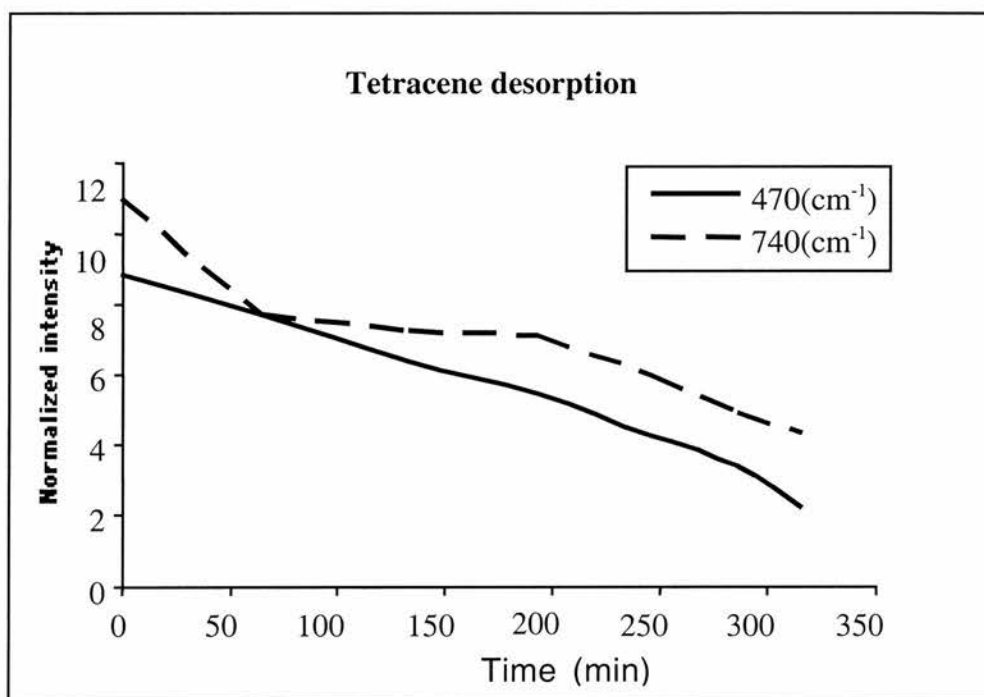


Fig. 7.7 Variation of EELS peak intensity as a function of time for tetracene desorption from H:Si(111) surface after 20 min dosage at room temperature for the peaks at 470 and 740 cm^{-1} .

7.5 HREELS study of tetracene adsorption on clean Si(100)-2x1

A spectrum in the specular direction of clean Si(100)-2x1 is shown in Fig. 7.8a. After dosing for 20 min, the multilayer thin film spectrum of tetracene was obtained (Spectrum b). Three distinctive peaks are present at 475, 750, and 1175 cm^{-1} . The peak locate at 475 cm^{-1} corresponds to C–C–C out-of-plane bending mode, the loss at 750

cm^{-1} is assigned to a C–H out-of-plane bending mode. In contrast, the peak at 1175 cm^{-1} corresponds to C–H in-plane bending mode. Also, there are small features present at 1450 and 1580 cm^{-1} , corresponding to C–C stretching modes, and near 3000 cm^{-1} , which is assigned to a CH stretching mode. It is not possible to conclude, according to this spectrum, a flat-adsorption of tetracene molecules on clean Si(100) surface due to the strong in-plane mode at 1175 cm^{-1} , for this coverage. Instead, the combination of in-plane and out-of-plane modes leads to suggest a random orientation of tetracene molecules at multilayer coverage. In contrast to tetracene on H:Si(111), these features were stable with time suggesting a strong interaction with the Si(100) substrate.

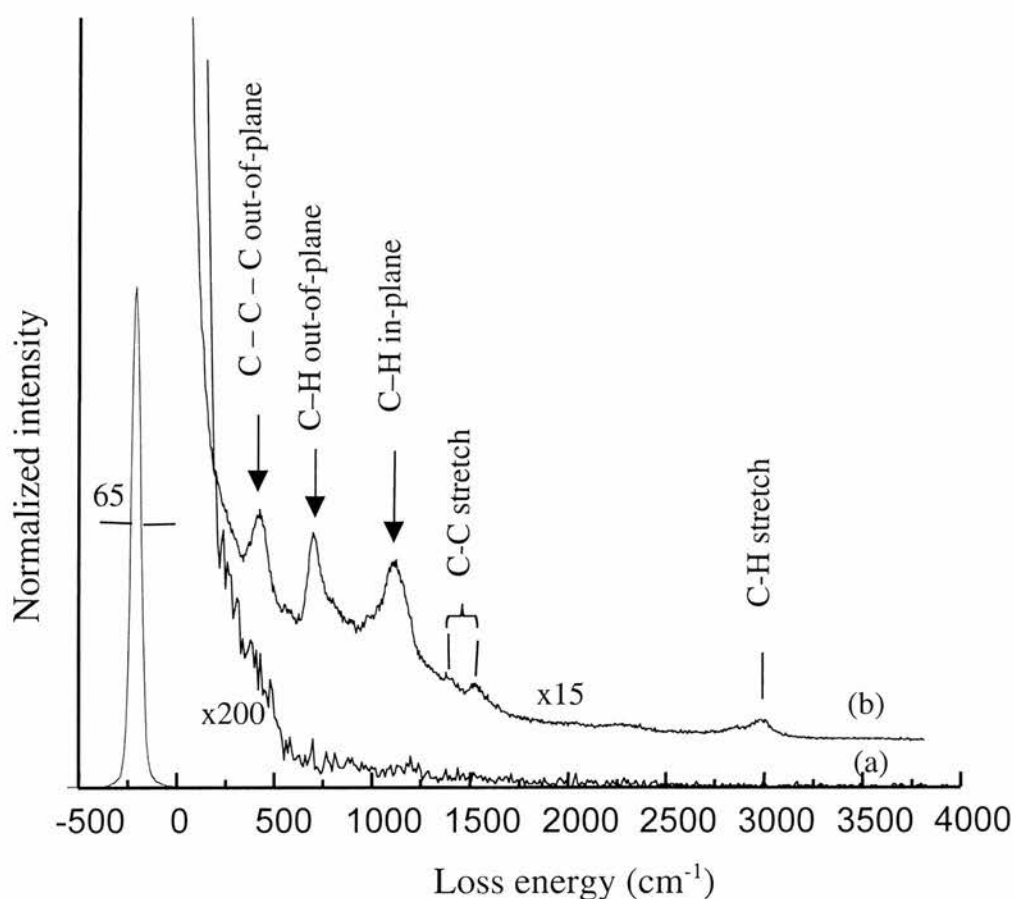


Fig. 7.8 EEL spectra of clean Si(100) 2×1 spectrum (a) and tetracene thin film (b.)

7.6 STM analysis of tetracene on Si(100)-2x1

Early in the development of STM, Tersoff & Hamann created the theoretical framework for understanding the atomic-level resolution images that the technique provides [34]. They showed that the tunnelling current is proportional to the local density of states of the surface at the position of the tip. Lang provided clear explanations for the characteristic signatures of chemically different atomic adsorbates [35]. He showed that sulphur, an electronegative element, can appear as a pronounced protrusion in filled state images but as a weak feature, possibly a depression, in empty state images [36]

7.6.1 Filled state image

Figure 7.9a shows a filled state image of 0.03 ML tetracene chemisorbed on Si(100)-2x1, where a coverage of one monolayer (ML) corresponds to one tetracene molecule for each silicon dimer. This filled state image was taken at a tunnelling current of 0.07 nA and a sample bias voltage of -2.6 V. Two silicon terraces present are separated by a single-height atomic step. On both terraces, the surface structure consists mainly of rows of symmetric dimers. However, at surface defects and at the step edge, zigzag, the rows of asymmetric dimers, can be seen. Chemisorbed tetracene molecules appear as brighter features. These molecules are orientated in two different ways; perpendicular and parallel to silicon dimer rows.

Tetracene molecules located perpendicular to the Si dimer rows (labelled A in Fig. 7.9a) show three protrusions. Note that this feature occurs on both terraces. In this STM image, the molecule seems to extend from the second silicon atoms belonging to the first dimer row, is centred over two dimers in the second row, and continues to the first silicon atoms in the third dimer row. In this case, the length of the tetracene

molecule is 13.4 \AA , as determined from line profiles, such as α shown in Fig. 7.9b. I will return to this part later *vide infra*, after presenting results from *ab initio* calculations.

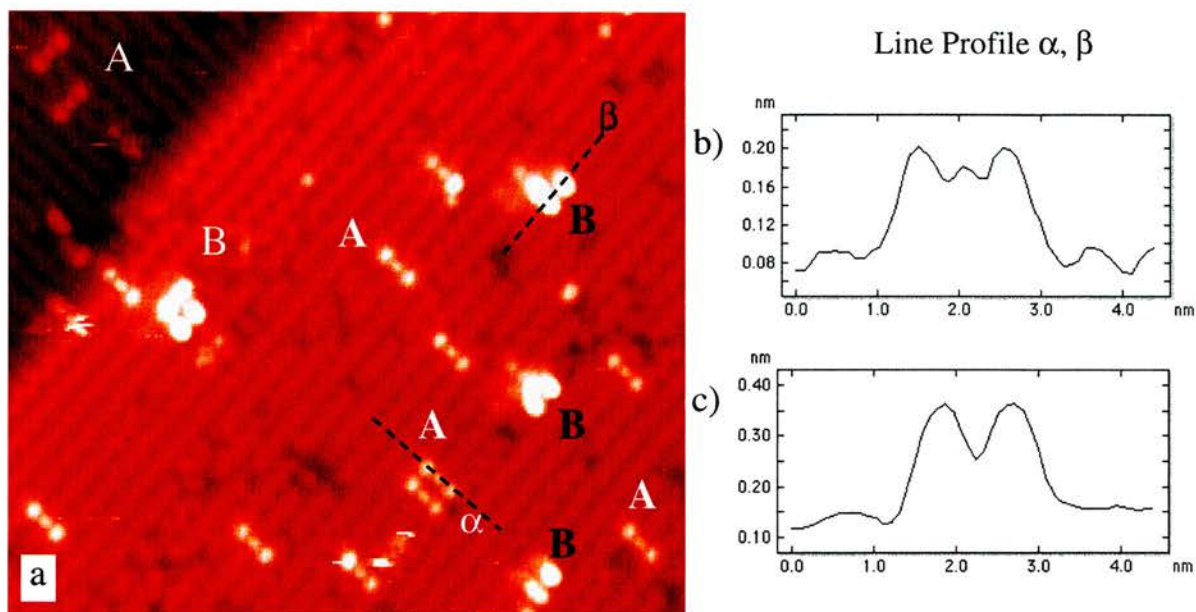


Fig. 7.9 (a) Filled state STM image ($25 \text{ nm} \times 18 \text{ nm}$) of tetracene on Si(100)- 2×1 (70 pA ; -2.6 V). Two types of bright features can be distinguished. Feature A is a tetracene molecule perpendicular to the Si dimer rows. Feature B corresponds to tetracene molecule on top of the Si dimer rows. Line profiles α and β of those adsorption sites, A and B, parallel to the long molecular axis are shown in (b) and (c) respectively.

A second type of adsorption corresponds to tetracene molecules on top of the silicon dimer rows aligned parallel with the dimer rows (labelled B in Fig. 7.9a). Here, two rather than three brighter spots indicate the tetracene molecule. Measurement of the

B type tetracene length is similar to A type adsorption, as shown in the line profile β on Fig. 7.9c. Similar results with a different number of the bright spots for the same organic molecule have been reported for pentacene on Si(100) by Kasaya et al [5]. Finally, it was found that the ratio between features A and B (A/B), taken from a larger image (30.6 nm x 30.6 nm), is 3/2. It means that there are three molecules located perpendicular to the dimer rows per two molecules parallel to the dimer rows.

7.7.2 Empty state image

It is well known that changing the polarity of the bias voltage between the sample and the tip, can markedly alter the STM images particularly for adsorption on semiconductors [9]. Here, is not an exception to such a rule. The empty state image, shown in Fig. 7.10a, was taken at a tunnelling current of 0.215 nA and a sample bias voltage of +2.6 V. In this image, three distinctive features, as depressions, can be distinguished. They are labelled as A* for a rectangular hole perpendicular to the Si dimer rows. The size of this feature is 13.6 Å, as shown in the line profile (see Fig. 7.10b), which is in agreement with the van der Waals' length of the tetracene molecule.

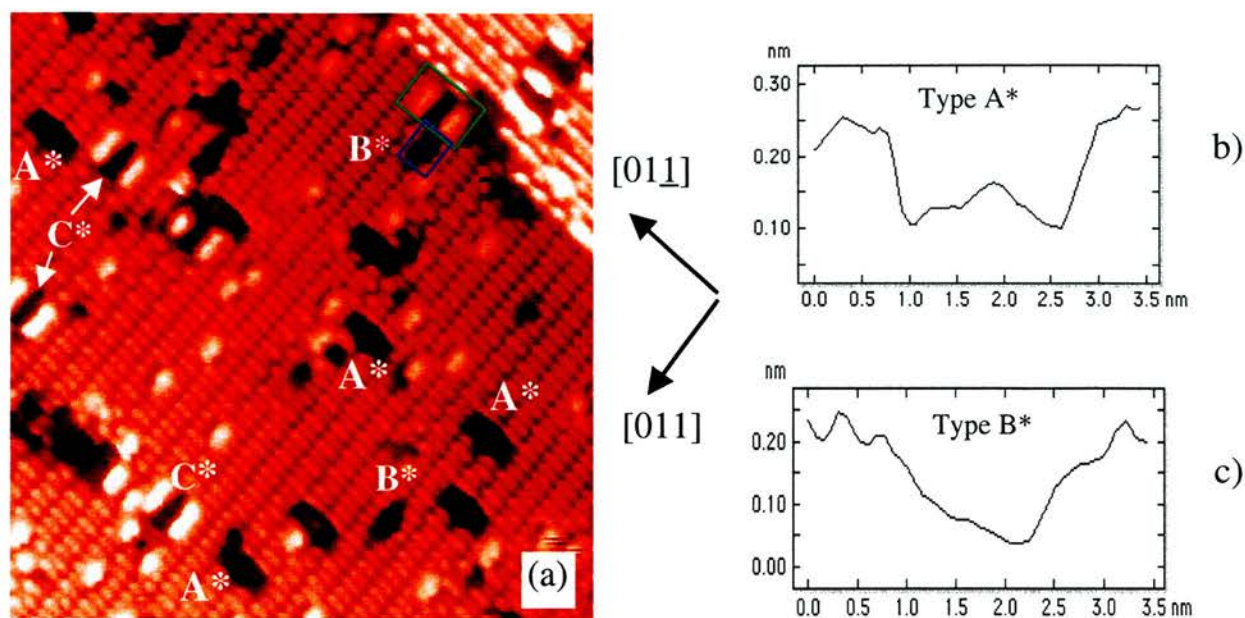


Fig. 7.10 (a) Empty state STM image (22 nm x 22 nm) of tetracene on Si(100)-2x1 (0.26 nA; +2.6 V). Three different adsorption types can be seen. The boxes near the top in the right show the difference between tetracene molecules on top of the dimer row (B*) and inter-dimer rows. (C*). Line profiles are presented for each type of adsorption parallel to the long molecule axis (b), (c).

A second feature labelled as B* is also present, which corresponds to tetracene molecule aligned parallel to the dimer rows but located on top of the silicon dimer row. Here it must be clear that although the empty state image presented has rows of bright features, those rows are not coincident with dimers. Instead those bright rows correspond to inter-dimer sites, i.e. there is nodal plane at the feature of the dimer in the case of empty states. The third type of adsorption site (labelled as C*) is a rectangular hole whose longer side is again parallel to the silicon dimer rows, but now located in between dimer rows, and therefore termed the inter-dimer site. The line profile confirmed that the length is similar in both cases B* and C*, as shown in Fig. 7.10c, d.

Bright borders can be seen parallel and on each side of to molecule of type C*. The line profile across and perpendicular to type C* is shown in Fig. 7.11. The ratio taken from a larger image (30.6 nm x 30.6 nm) of the features A*, B* and C*, (presented as $A^*/[B^*+C^*]$) is approximately 1/1.

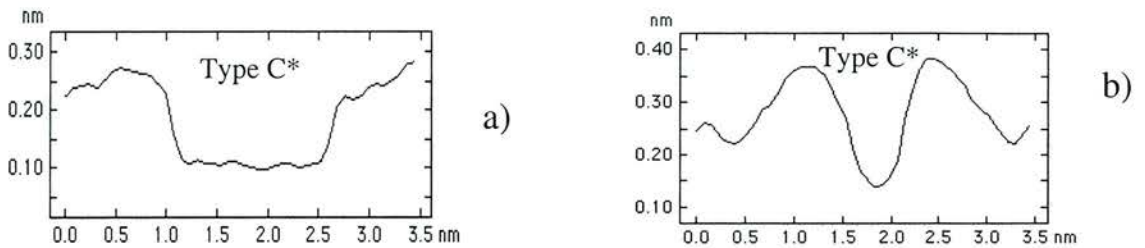


Fig. 7.11 Line profiles across a) and perpendicular b) to type C are presented.*

In Fig 7.12 a comparison between 2 empty state STM images is presented. Those images were taken from the same area with different tunnelling current at sample bias voltage 2.6 V. The image with a low tunnelling current (left) shows better resolution of the individual silicon atoms, also a sharper contour for those depressions. In contrast, within the higher tunnelling current (right), the silicon atoms contour overlap and seem to form Si dimer rows instead of inter-dimer rows. The feature labelled B*, which is located on top of the dimer become larger along its longer axis and covering 4 silicon dimers.

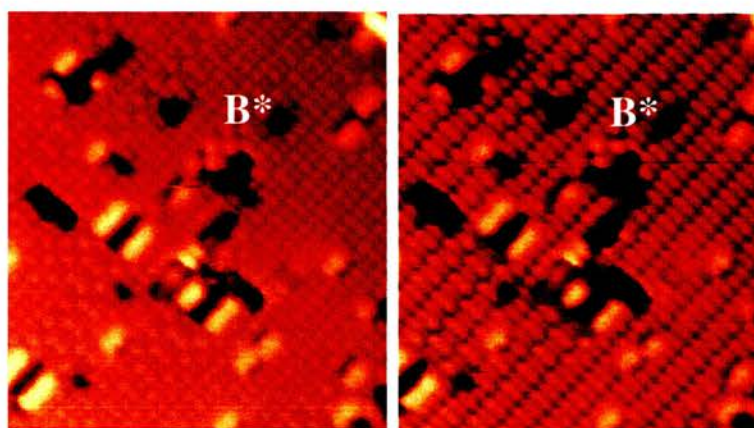


Fig. 7.12 Two empty state STM images (12.5 nm x 14.6 nm) from the same region were recorded at different tunnelling current (+2.6 V). The left hand image was taken at 0.066 nA. The other image was recorded at 0.26 nA (right). Feature B is showed for comparison between these two images.*

7.8 *Ab initio* calculations

Density functional calculations (B3LYP/6-31G*) combined with geometrical optimization, using Gaussian 98, was employed to obtain the population analysis, energy level, orbital symmetry and IR frequency values of an isolated tetracene molecule. The charge density distributions associated with the highest occupied and the lowest unoccupied π -molecular orbitals are shown in Fig. 7.13 [37]. In addition, the energy level distribution between -11 eV and 5 eV is represented. The symmetry of π -orbitals between -11 eV and 5 eV is also denoted.

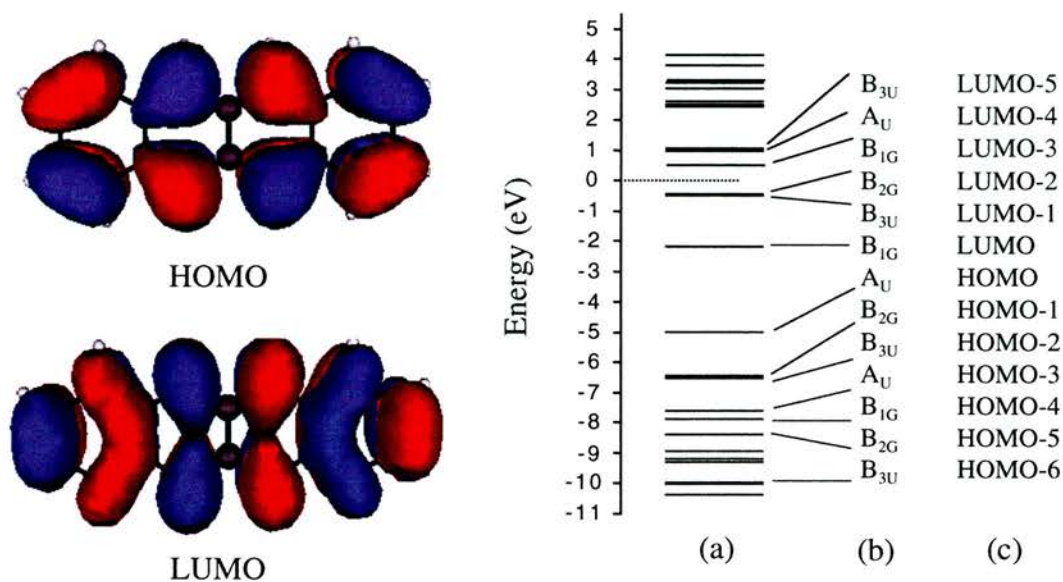


Fig. 7.13 The charge density distributions of the HOMO and the LUMO of tetracene molecule are showed. Also, the energy of molecular orbitals in the range -11 eV to 5 eV (a), the symmetries of π -orbitals (b) and the label of π -orbitals (c).

7.9 Discussion

It is clearly noticeable from the filled state STM images two types of molecular adsorption sites can occur corresponding to orientations perpendicular and parallel to the silicon dimer rows. Type A has three bright spots in contrast to the even brighter two-lobed protrusion of type B, as shown in Fig. 7.9. In favourable cases, we might hope that the STM images would be dominated by tunnelling through a specific molecular orbital located, in energetic terms, by appropriate bias conditions on the tip.

Ideally the image would match the density distribution in the relevant orbital and most obviously the pattern of its nodal planes. Of course, mixing between adsorbate and substrate orbitals in strongly chemisorbed systems may complicate this simple picture considerably. However, the HOMO charge density distribution, shown in Fig. 7.13 does not match the STM images corresponding to either site. A more detailed analysis of the other filled molecular orbital is needed to explore the different nodal patterns, which might be reflected in the STM images. Specifically, it has been found that the B_{3u} molecular orbitals HOMO-2 and HOMO-6 have three regions of high charge density separated by two nodal planes (see Fig. 7.14). These may be major contributors to the filled state imaging of molecule in site A.

Molecule in type B sites, parallel to and top of Si dimer rows, seem to correlate more closely with the charge density of HOMO-3 (A_u) and with the possibility of some contributions from the HOMO-4 (B_{1g}) since each of them has a central nodal plane and regions of high charge density, which might correlate with the two bright regions of the STM image. Any occupancy of the LUMO (B_{1g}), due to charge transfer into this orbital from silicon could also contribute to the image at site B.

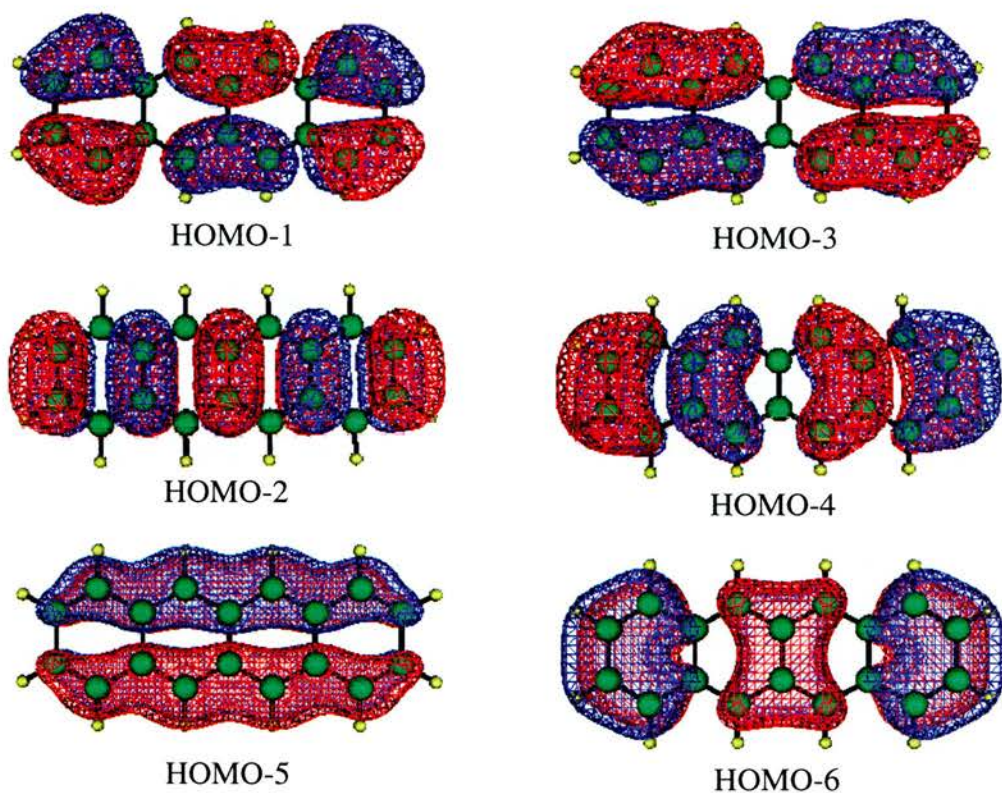


Fig. 7.14 Representations of six occupied molecular orbitals plotted after energy calculations of insulated tetracene. Some of them are related with the filled state STM image presented in Fig. 7.9a. According to those maps we can assign tentatively: to type A the HOMO-1 and/or HOMO-6 levels; and for type B corresponds to the HOMO-3 and/or HOMO-4 levels.

In order to consider the influence of the substrate bonds on such an image in conjunction with the electronic structure calculations, a knowledge of the registry of the molecule and the substrate is important. Careful analysis of the images shows that at tetracene molecule in site A has its central interaction on top of the dimer row, though it

is noted the intensity of this central part seems weak, compared with the two spots at each end, which are located over the valley between silicon dimers, see Fig. 7.15. Registry of the molecules in site A along the dimer row is harder to determine but it is considered centred directly between Si dimers.

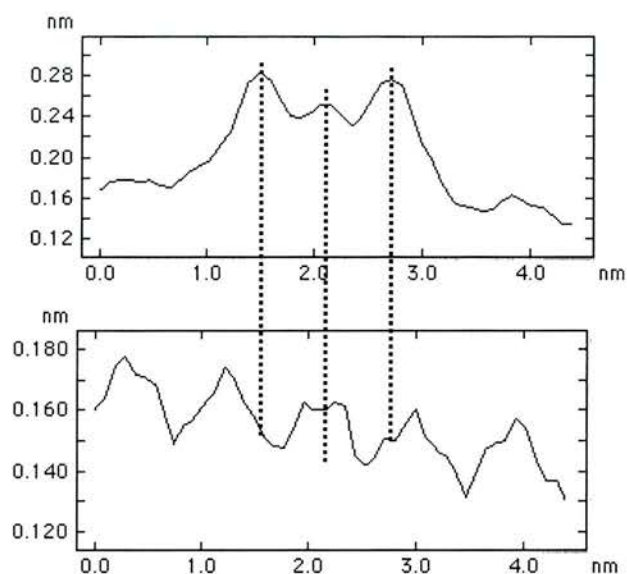


Fig. 7.15 A registry of tetracene on silicon substrate. The middle lobes of tetracene molecule lie (symmetrically) directly on top of the Silicon dimer in contrast with the brighter part that is located on the dimer valley. The separation distance between silicon dimer rows is 7.68\AA ($a_0 \cdot \sqrt{2}$)

Unfortunately, registry of the silicon dimers was not possible to obtain for type B adsorption. Another aspect that is important to point out is the difference in the height of the type A and B, as we can distinguish from line profile (Fig. 7.15) for those features. From those profiles, the adsorption of tetracene parallel to the dimer rows, type B, is favourable for the highest contrast.

Model for the two adsorption sites, A and B, based on the filled state image are depicted in Fig. 7.16. There the possible adsorption sites for both type of tetracene molecule is suggested. For type A, symmetric Si–C bonds seem to be formed in the central part of tetracene, with the two farthest carbon atoms, from the second (labelled 2 and 7) and third benzene (labelled 3 and 6) rings, attached to two dimers. The others carbon atoms do not seem to be bonded in any way to silicon atoms. For tetracene adsorption parallel to the silicon dimer row, type B, it is possible that the carbon atoms 2,3,6 and 7, belonging to the second and third benzene rings are again involved and bridge bond to silicon atoms in the dimer.

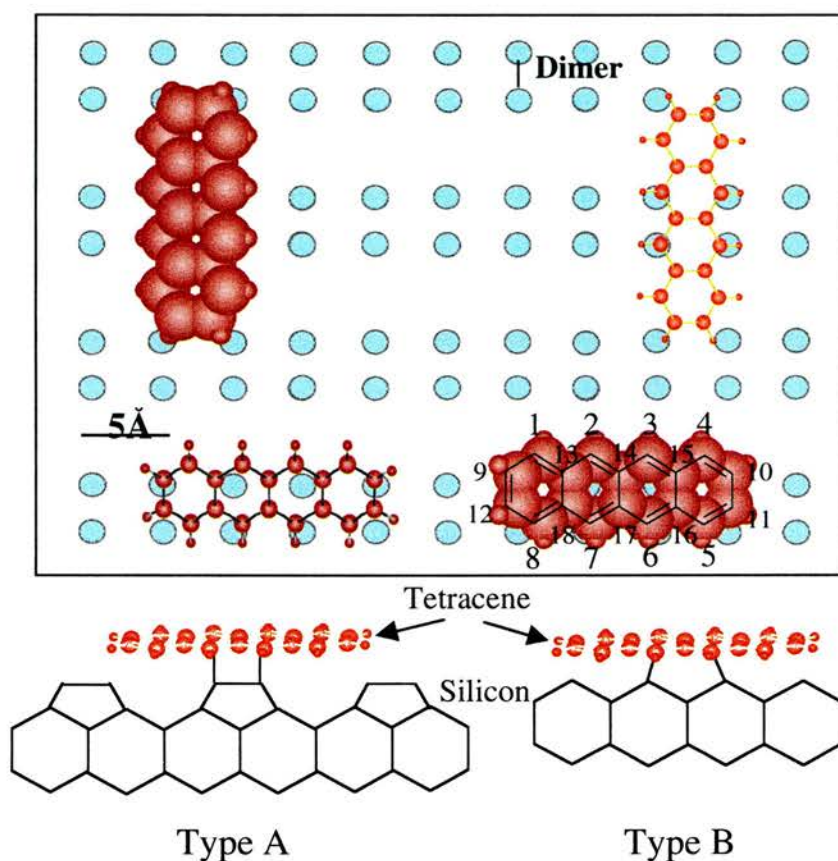


Fig. 7.16 Schematic model of the filled state image shows the tetracene adsorption of type A and B, including a side view and the bonding sites.

Regarding the empty state images, in contrast three adsorption sites have been distinguished, Fig. 7.10. We relate features of type A*, perpendicular to the dimer rows, with those identified as A in the filled state images. Comparison of type A molecules in filled and empty state images allow us to confirm that the Si dimer rows, which are bright features in the filled state image, are centred in the dark regions of the empty state images (Fig. 7.10). In turn this allows us to recognise in the empty state images that, of the molecules parallel to the dimer rows, it is these labelled B*, on-top of the dimer rows, which correlate with type B of the filled state image, while those identified as C* lie parallel but between Si dimer rows and have not been recognised in filled state images. Molecules in this site are accompanied by a bright protrusion on each side of the tetracene. Such holes and protrusions have been seen previously in the case of pentacene adsorption on Si(100)-2x1 within empty state images [38]. As Kasaya et al. [10] suggested, images observed are a combination of both molecular and silicon derived orbital. A possible long range contribution from silicon atoms in the adjacent dimer rows along the [011] direction presumably gives rise to those protrusions on both sides of the tetracene hole.

7.9 Conclusions

Chemisorption of tetracene molecule on clean Si(100)-2x1 at room temperature was obtained. Highly resolved STM images have shown that three adsorption sites are possible corresponding in each case to flat-lying tetracene molecules. Molecules can adopt an azimuthal orientation either perpendicular to Si dimer rows or parallel to the dimer rows. Molecules with the latter orientation can, on the basis of empty state images, occupy sites both on-top of the dimer rows or between the rows, although the latter is not an identifiable site in filled state images. It has been possible to tentatively

identify the principal orbital contributions to filled state images and recognise possible contribution to the Si–molecule bonding. From HREEL spectra of H:Si(111), it is confirmed the weak van der Waals interaction between tetracene molecules and with passivated surface, which leads to the conclusion of physisorption of tetracene on H:Si(111).

References

- 1 J.H.Schon, Ch. Kloc, A. Dodabalapur, B. Batlogg. *Science* **289**, 599 (2000).
- 2 B. Crone, A. Dodabalapur, Y. Y. Lin, R. W. Filas, Z. Bao, A. LaDuca, R. Sarpeshkar, H. E. Katz, and W. Li. *Nature* **403**, 521 (2000).
- 3 J.H.Schon, S. Berg, Ch. Kloc, B. Batlogg. *Science* **287**, 1022 (2000).
- 4 J.H.Schon, Ch. Kloc, B. Batlogg. *Nature* **406**, 702 (2000).
- 5 J.H.Schon, S. Berg, Ch. Kloc, B. Batlogg. *Science* **288**, 2338(2000).
- 6 S. F. Nelson, Y. Y. Lin, D. J. Gundlach, T. N. Jackson. *Appl. Phys. Lett.* **72**, 1854 (1998)
- 7 E. A. Silinsh, V. Capek. *Organic Molecular Crystals*. (AIP, New York, 1994)
- 8 T. Ishiguro, K. Yamaji, G. Saito, *Organic Superconductors* (sSpringer, Berlin, 1998)
- 9 W. Warta, N. Karl, *Phys. Rev. A* **36**, 163 (1985).
- 10 M. Kasaya, H. Tabata, T. Kawai. *Surf. Scie.* **400**, 367 (1998)
- 11 T. Yamaguchi. *J. Phys. Soc. Jpn.* **68**, 1321 (1999).
- 12 T. Bitzer, T. Rada, N. V. Richardson. *J. Phys. Chem.* **105**, 4535 (2001)
- 13 Q. Chen, T. Rada, A. MacDowall, N. V. Richardson. *Chem. Mater.* **14**, 743 (2002).
- 14 Q. Chen. D. J. Frankel, N.V. Richardson. *Langmuir* **17**, 8276 (2001).

-
- 15 W. A. Hofer, A. J. Fisher, R. A. Wolkow, P. Grutter, *Phys. Rev. Lett.* **87**, 236104 (2001)
- 16 W. A. Hofer, A. J. Fisher, T. Bitzer, T. Rada, N. V. Richardson. *Chem. Phys. Lett.* **355**, 347 (2002)
- 17 T. Yamaguchi. *J. Phys. Soc. Jpn.* **68**, 1321 (1999)
- 18 **either**: M. N. Piancastelli, F. Cerrima, G. Margaritondo, A. Franciosi, J. H. Weaver, *Appl. Phys. Lett.* **42**, 990 (1983) or M. N. Piancastelli, G. Margaritondo, J. Anderson, D. J. Frankel, G. J. Lapeyre, *Phys. Rev. B* **30**, 1945 (1984).
- 19 R. Gromer, *Rep. Prog. Phys.* **53**, 917 (1990).
- 20 Y. Taguchi, M. Fujisawa, M. Nishijima, *Chem. Phys. Lett.* **178**, 363 (1991).
- 21 Y. Taguchi, M. Fujisawa, T. Takaota, T. Okada, M. Nishijima, *J. Chem. Phys.* **95**, 6870 (1991).
- 22 B. I. Craig, *Surf. Sci. Lett.* **280**, L270 (1993).
- 23 H. D. Jeong, S. Ryu, Y. S. Lee, S. Kim, *Surf. Sci. Lett.* **344**, 1226 (1995).
- 24 R. A. Wolkow, G. P. Lopinski, D. J. Moffatt, *Surf. Sci.* **416**, L1107 (1998). And references therein
- 25 W. A. Hofer, A. J. Fisher, G. P. Lopinski, R. A. Wolkow, *Phys. Rev. B* **63**, 085314 (2001).
- 26 B. Borosvky, M. Krueger, E. Ganz. *Phys. Rev. B* **57**, R4269 (1998).
- 27 Gaussian 98, Revision A.7, M. J. Frisch, G. W. Trucks, H. B. Schlegel, G. E. Scuseria, M. A. Robb, J. R. Cheeseman, V. G. Zakrzewski, J. A. Montgomery, Jr., R. E. Stratmann, J. C. Burant, S. Dapprich, J. M. Millam, A. D. Daniels, K. N. Kudin, M. C. Strain, O. Farkas, J. Tomasi, V. Barone, M. Cossi, R. Cammi, B. Mennucci, C.

Pomelli, C. Adamo, S. Clifford, J. Ochterski, G. A. Petersson, P. Y. Ayala, Q. Cui, K. Morokuma, D. K. Malick, A. D. Rabuck, K. Raghavachari, J. B. Foresman, J. Cioslowski, J. V. Ortiz, A. G. Baboul, B. B. Stefanov, G. Liu, A. Liashenko, P. Piskorz, I. Komaromi, R. Gomperts, R. L. Martin, D. J. Fox, T. Keith, M. A. Al-Laham, C. Y. Peng, A. Nanayakkara, C. Gonzalez, M. Challacombe, P. M. W. Gill, B. Johnson, W. Chen, M. W. Wong, J. L. Andres, C. Gonzalez, M. Head-Gordon, E. S. Replogle, and J. A. Pople, Gaussian, Inc., Pittsburgh PA, 1998.

28 Alexander. McDowall, private communication.

29 Ch. Poucher, The Aldrich Library Infrared Spectra 2nd Edition (1978).

30 H. Torii, Y. Ueno, A. Sakamoto, M. Tasumi. *J. Phys. Chem. A* **103**, 5557 (1999).

31 P. K. McCarthy, G. J. Blanchard. *J. Phys. Chem.* **99**, 17753 (1995).

32 Ch. Stuhlmann, G. Bogdanyi, H. Ibach, *Phys. Rev. B* **45**, 6786 (1992).

33 J. Szczepanski, M. Vala, *The Astrophysical J.* **414**, 646 (1993).

34 J. Tersoff, D. R. Hamann, *Phys. Rev. B* **31**, 805 (1985).

35 N. D. Lang, *Phys. Rev. Lett.* **55**, 230 (1985).

36 N. D. Lang, *Phys. Rev. Lett.* **58**, 45 (1986).

37 Gamess Version. 25 Mar 2000 From Iowa State University M.W.Schmidt,

K.K.Baldrige, J.A.Boatz, S.T.Elbert, M.S.Gordon, J.H.Jensen, S.Koseki,

N.Matsunaga,K.A.Nguyen, S.J.Su, T.L.Windus,Together With M.Dupuis,

J.A.Montgomery, *J.Comput.Chem.* 14, 1347-1363(1993)

38 A.A. Cafolla, D. Carty, P. Guaino, G. Hughes, P. Moriarty. PRIVATE

COMMUNICATIONS